II. PLASMA DYNAMICS

II-A. PLASMA PHYSICS*

Prof. S. C. Brown
Prof. W. P. Allis
Prof. G. Bekefi
Prof. D. J. Rose
Prof. D. R. Whitehouse
Dr. S. Gruber
V. Arunasalam
D. E. Baldwin
C. D. Buntschuh
J. D. Coccoli
E. W. Fitzgerald, Jr.
S. Frankenthal
P. J. Freyheit
J. C. Ingraham
W. R. Kittredge
J. J. McCarthy
W. J. Mulligan
J. J. Nolan, Jr.
J. C. Terlouw
K. F. Voyenli
R. E. Whitney

1. MICROWAVE MEASUREMENTS OF THE RADIATION TEMPERATURE OF A PLASMA IN A MAGNETIC FIELD

Measurements of the intensity and spectrum of the microwave emission from a plasma can be used to infer the energy and energy distribution of the free electrons. In the present experiments we used a technique (1, 2) that permitted a direct determination of the ratio of the emissivity of the plasma electrons, j_ω, to the self-absorption, α_ω, of this emission in its passage through an elementary volume of the plasma. This ratio $B(\omega, T_r)$ (often called the "Ergiebigkeit" or source function) is a measure of the electron energy. When the electrons have a Maxwellian distribution of energies, $B(\omega, T_r)$ is Planck's formula for the black-body emission, T_r equals the electron temperature T_e, and the function $B(\omega, T_e)$ is independent of the detailed emission and absorption processes taking place inside the plasma. However, when the electrons do not have a Maxwellian distribution, calculations (3) show that $B(\omega, T_r)$ depends on the cross section for emission (and on the related cross section for absorption). In this case T_r (which we shall call the radiation temperature), although related to the electron energy ($\bar{u}$), is not equal to it. In the absence of an external magnetic field, the difference between $T_e \equiv (2/3)(\bar{u}/k)$ and T_r is not very large. In a magnetic field, particularly at a frequency ω equal to the electron orbital frequency $\omega_b = eB/m$ (where B is the magnetic field strength), T_r can depart significantly from T_e.

Let $f(v_{||} v_\perp)$ be the distribution function of electron velocities, where $v_{||}$ is the velocity in the direction of the applied magnetic field, and $v_\perp$ is the velocity perpendicular to the magnetic field. The distribution function is normalized so that $\int_0^\infty f\, 2\pi v_\perp dv_\perp dv_{||} = 1$. When a steady state is established between the emission and the absorption and the plasma is sufficiently tenuous so that $(\omega_p/\omega)^2 \equiv ne^2/m\epsilon_o\omega^2 \ll 1$, calculations show (4) that for cold electrons ($v/c \ll 1$),

*This work was supported in part by the Atomic Energy Commission under Contract AT(30-1)-1842; and in part by the Air Force Command and Control Development Division under Contract AF19(604)-5992; and in part by the National Science Foundation under Grant G-9330.

$$kT_r = -m \frac{\int_{-\infty}^{\infty} \int_{0}^{\infty} vR(v)\, f(v_{||}, v_{\perp})\, v_{\perp}^3\, dv_{\perp}\, dv_{||}}{\int_{-\infty}^{\infty} \int_{0}^{\infty} vR(v) \left[\frac{\partial f(v_{||}, v_{\perp})}{\partial v_{\perp}}\right] v_{\perp}^2\, dv_{\perp}\, dv_{||}} \tag{1}$$

Here, m is the electron mass, and $R\left(v = \left(v_{||}^2 + v_{\perp}^2\right)^{1/2}\right)$ is an absorption cross section for the radiation. When the radiation results from bremsstrahlung and cyclotron emission of cold electrons, R becomes (3)

$$R(v) = \frac{\omega^2 Q_m(v)[(1+\cos^2\theta)/2]}{(\omega-\omega_b)^2 + [NvQ_m(v)]^2} \tag{2}$$

where Q_m is the elastic collision cross section for momentum transfer (5), N is concentration of atoms, and θ is the angle between the direction of observation of the emission and the magnetic field.

Note that when the distribution function is a Maxwellian, $f \propto \exp\left[-m\left[v_{||}^2+v_{\perp}^2\right]\Big/ 2kT_e\right]$, then T_r of Eq. 1 becomes T_e. Likewise $T_r = T_e$ if the distribution is Maxwellian in the perpendicular direction only and arbitrary in the parallel direction; that is, $f \propto \exp\left[-bv_{\perp}^2\right] \Phi(v_{||})$, where b is a constant. Hence, any departures of T_r from T_e require that the distribution function be non-Maxwellian in the perpendicular direction.

For simplicity of calculation, we assume a spherically symmetric distribution function of the form

$$f(v) \propto \exp[-b(v/\bar{v})^{\ell}] \tag{3}$$

where $\bar{v}$ is the mean electron velocity, and b and ℓ are arbitrary positive constants. When $\ell = 2$ the distribution is Maxwellian; when $\ell > 2$ there is an excess of slow electrons, and when $\ell < 2$ the opposite is the case. The parameter b determines the mean electron energy $\bar{u}$.

In Fig. II-1 is shown a plot of $3kT_r/2\bar{u} \equiv T_r/T_e$ as a function of frequency, for $\ell = 6$. In the calculations for this figure the collision cross section Q_m was assumed to have the following dependence on the electron velocity:

$$Q_m = a(v/\bar{v})^{h-1} \tag{4}$$

where a is a positive constant, and h is a constant greater than or equal to -3.

Figure II-1 illustrates the following characteristics of the radiation temperature: (a) when h is zero (that is, the collisions occur at a constant mean-free time), $T_r = T_e$, irrespective of the form of the distribution function; (b) when h is positive, T_r exhibits a pronounced peak at the cyclotron frequency and it exhibits a dip when h is negative

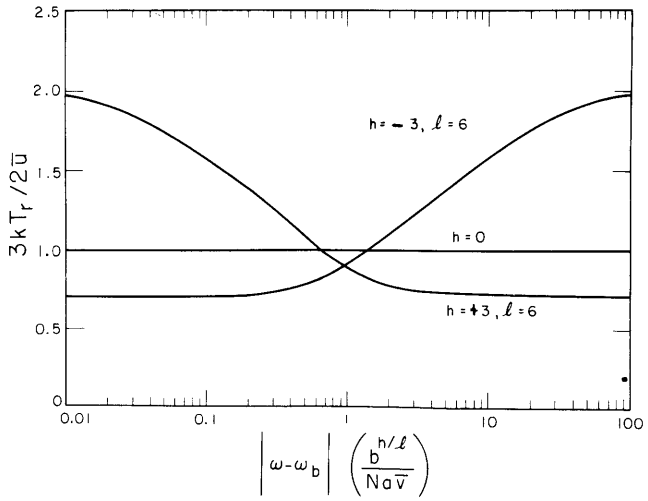

Fig. II-1. Radiation temperature as a function of frequency. The distribution function $f(v) \propto \exp[-b(v/\bar{v})^{\ell}]$; the collision cross section $Q_m = a(v/\bar{v})^{h-1}$.

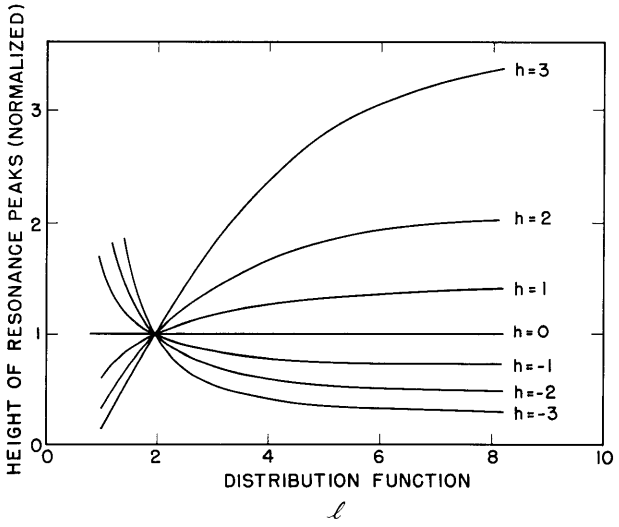

Fig. II-2. Normalized resonance peaks as a function of the distribution function for various cross sections. Ordinate represents the ratio of the magnitude of T_r at $\omega = \omega_b$ to the magnitude of T_r at $(\omega-\omega_b) \to \infty$.

(the opposite would be true had the calculations been made for $\ell < 2$); (c) the width of the resonance peak or dip is directly proportional to the gas pressure; (d) the ratio of T_r/T_e is independent of the charged-particle density; and (e) the height of the peak or dip (T_r/T_e) is independent of pressure.

Figure II-2 shows the ratio of the magnitude of the radiation temperature at the cyclotron frequency, $\omega = \omega_b$, to the magnitude of the radiation temperature at a frequency that is far removed from resonance, $(\omega-\omega_b) \rightarrow \infty$, for various cross sections and distribution functions.

a. Experimental Results

In Fig. II-3 we show the variation of the radiation temperature with magnetic field for argon, neon, and hydrogen as measured in the positive column of a dc glow discharge, subjected to an axial magnetic field. In argon and neon the radiation temperature shows a general decrease with increasing magnetic field, as indicated by the dashed lines.

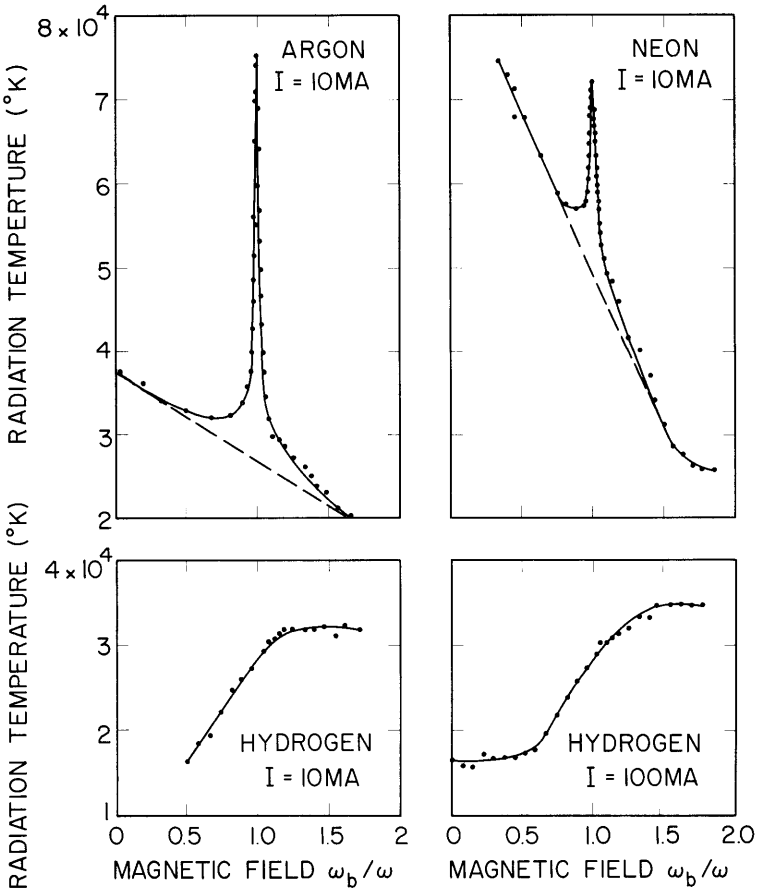

Fig. II-3. Variation of the radiation temperature with magnetic field in argon, neon, and hydrogen. (p_o = 0.28 mm Hg.)

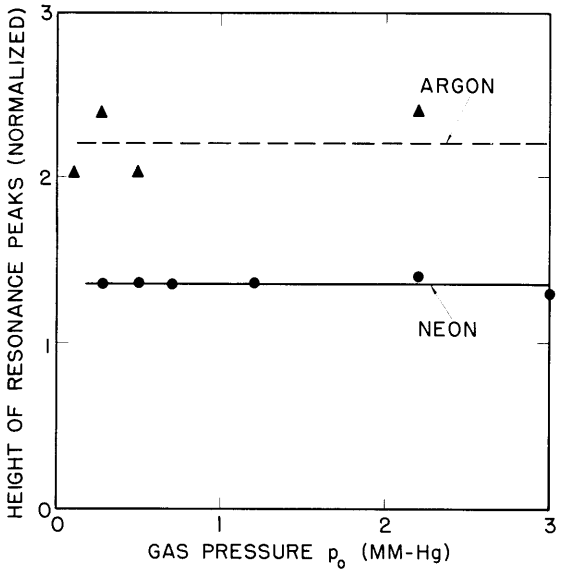

Fig. II-4. Normalized resonance peaks as a function of pressure.

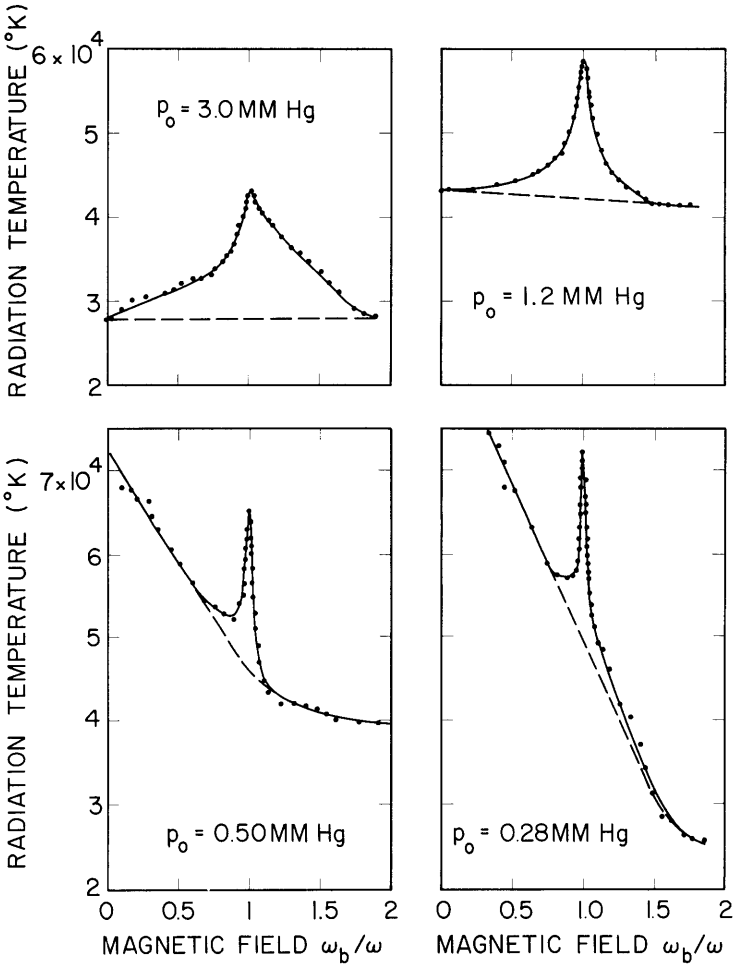

Fig. II-5. Variation of the radiation temperature with magnetic field in neon at various pressures. (I = 10 ma.)

This trend is in agreement with the predicted behavior of the electron temperature in the positive column. The large peaks at the cyclotron frequency are interpreted (see Figs. II-1 and II-2) as resulting from a non-Maxwellian distribution of electron velocities in a gas in which the cross section increases with energy ($h > 0$), in the energy range in which the measurements were made. Similar peaks were observed in xenon. Since in argon h is considerably greater than in neon, a larger peak is expected to occur, and measurements indicate that this is indeed so.

In hydrogen (see Fig. II-3) and in helium (not shown) no peaks were observed. Since in the energy range of measurement hydrogen and helium have a cross section that varies inversely with electron velocity ($h \approx 0$), no peaks are expected on the basis of the previous calculations. Note that the radiation temperature in hydrogen increases, rather than decreases, with increasing magnetic field, a fact that is in disagreement with the simple theory of the electron temperature in the positive column. However, this behavior is in agreement with the onset of an instability as observed by Hoh and Lehnert (6). The onset of this instability is characterized by a sudden increase of the axial voltage across the positive column. We find that this increase in voltage is accompanied by an increase in the radiation temperature.

One may suspect that the absence of peaks in hydrogen is the result of this instability. However, no peaks were observed in helium, although the onset of the instability occurred at frequencies far removed from the cyclotron frequency ($\omega_b/\omega > 1$). Therefore,

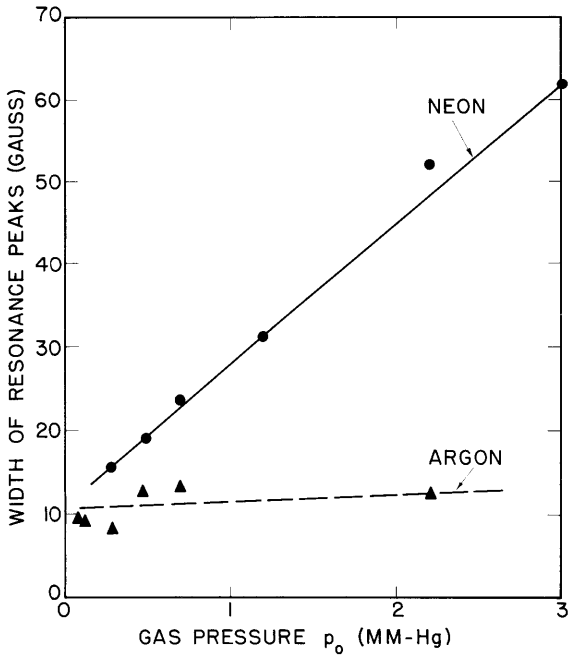

Fig. II-6. The width of the resonance peaks as a function of pressure.

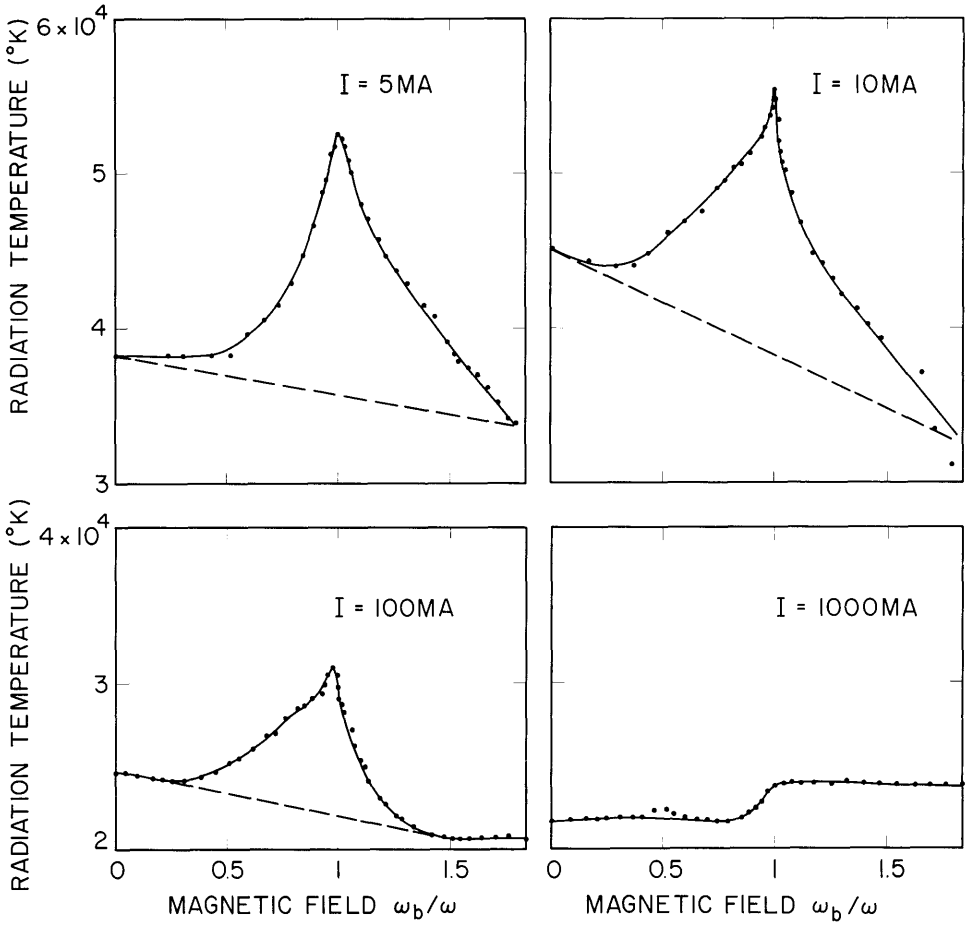

Fig. II-7. Variation of the radiation temperature with magnetic field in neon for various currents. (p_o = 2.2 mm Hg.)

in hydrogen and helium, we cannot attribute the absence of resonances to this instability. In Fig. II-4 we show a plot of the normalized resonance peaks (as defined by the ordinate of Fig. II-2) as a function of the gas pressure. The constancy of the magnitudes of the normalized peaks with pressure is in agreement with calculations.

Figure II-5 illustrates the broadening of the resonance peaks with increasing pressure. Figure II-6 shows that the width of the peaks is directly proportional to the pressure. (By extrapolating the curves to zero gas pressure, we find that the apparent width of the peaks tends to a value equal to 10 gauss. This extrapolated width is related approximately to the inhomogeneity in the magnetic field across 50 cm of the positive column from which the radiation was observed.)

Figure II-7 illustrates qualitatively that the widths and the magnitudes of the peaks are sensibly independent of the discharge current, provided that the current is not too large, so that the radiation is received from a sufficiently tenuous plasma. Only, in

this case, is a comparison between measurements and calculations expected to be meaningful.

These measurements show that the electron energy and energy distribution function can be inferred from the measurements of the radiation temperature, provided that the correct collision cross section for the gas in question is used in the calculations indicated by Eq. 1.

H. Fields, G. Bekefi

(Mr. Harvey Fields is from Microwave Associates, Burlington, Massachusetts.)

References

1. A. L. Gilardini, Technical Note No. 1, Air Force Cambridge Research Center, Bedford, Massachusetts, August 1959. Also D. Formato and A. Gilardini, Proc. Fourth International Conference on Ionization Phenomena in Gases (North Holland Publishing Company, Amsterdam, 1960), Vol. I, pp. IA99-IA104.

2. G. Bekefi and Sanborn C. Brown, J. Appl. Phys. 32, 25 (1961).

3. G. Bekefi, J. L. Hirshfield, and S. C. Brown, Phys. Fluids 4, 173 (1961).

4. S. Gruber, Negative conductivity in a plasma, Quarterly Progress Report No. 61, Research Laboratory of Electronics, M. I. T., April 15, 1961, pp. 5-10.

5. S. C. Brown, Basic Data of Plasma Physics (Technology Press of Massachusetts Institute of Technology, Cambridge, Mass., and John Wiley and Sons, Inc., New York, 1959).

6. F. C. Hoh and B. Lehnert, Phys. Fluids 3, 600 (1960).

2. MEASUREMENTS OF CONTROLLED TURBULENCE

The existence of turbulence in plasmas is generally considered to be a cause of increased diffusion and instabilities. This turbulence arises chiefly in high-temperature, highly ionized gases. In this report we discuss measurements of turbulence in a plasma of low degree of ionization and of low temperature. The turbulence was produced by dry air flowing past an obstacle at high velocity. This turbulent gas was ionized by an rf voltage. The turbulence of the neutral atoms and the ions is also transferred to the electrons by means of the space charge forces. From a knowledge of the obstacle size, gas velocity, and gas pressure, the nature of the turbulent velocity field of the plasma can be inferred.

a. Experimental Arrangement

In these experiments it was necessary to use a supersonic wind tunnel in order to achieve a high gas velocity (for turbulence to set in), and a sufficiently low gas pressure, to permit breakdown. In this manner, we were able to make a gas flow through a channel of 2-inch square cross section, at velocities in the neighborhood of sonic velocity. The static gas pressure was approximately 5 mm Hg. An obstacle was introduced into

the cross section plane of the channel.

The gas was ionized by an rf voltage at a frequency of 40 kc. The power (approximately 5 kw) was fed into the discharge through two capacitor plates embedded in opposite walls of the Plexiglas channel. In this manner, a volume of plasma 7 in. × 2 in. × 2 in. was produced. The rf source did not introduce any low-frequency modulation of the electron density (for example, at 60 c/s), and hence of the light intensity emanating from the discharge.

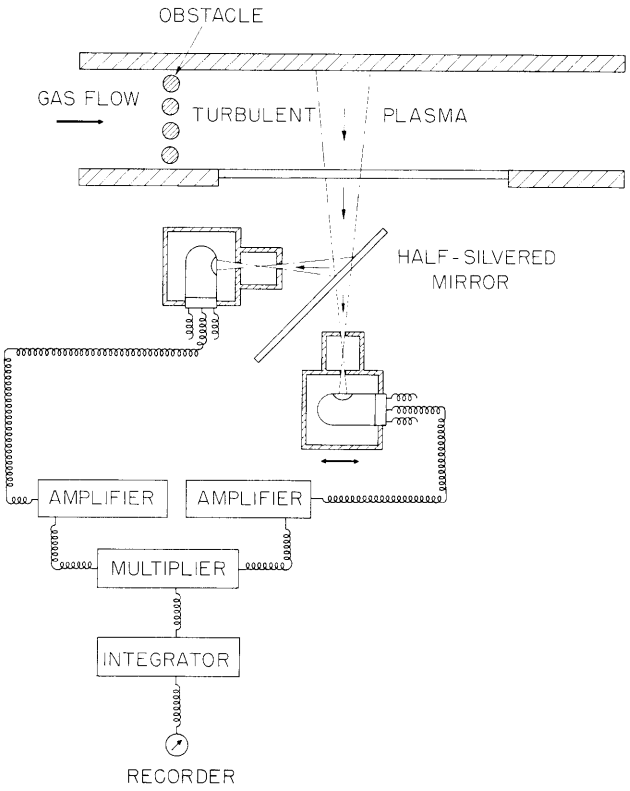

Fig. II-8. Schematic drawing of the optical system.

The optical system was designed to measure the intensity fluctuations of the light from the plasma (see Fig. II-8). Two parallel cones of light, each of 1° cone angle, were received. The width of the cones was determined by holes, 10^{-2} inches in diameter, drilled in brass cylinders that were 1 inch long. These cylinders were fitted over two photomultiplier tubes mounted in a light-tight box. One of these phototubes was mounted on a precision-ground and lapped platform, and was movable over a distance of 4 inches. The half-silvered mirror permitted measurements to be made for small and zero separation between the light cones. The maximum separation was ±2 inches.

The output from each photocell was amplified approximately 100 db, and the product

of the two signals was taken. A 10-second sample of the product was averaged in time and recorded for each separation of the light cones. The frequency response of the electronic system that was used ranged from 3 cps to 20,000 cps.

The optical system was mounted 2 inches away from a glass window through which the turbulent plasma was observed. A physical displacement of the complete system allowed us to study the turbulence at various distances from the obstacle in the range 2 in. -10 in. downstream from it.

b. Results

Figure II-9 shows correlation measurements of the light fluctuations behind an obstacle that consisted of a planar array of 16 Plexiglas cylinders, each 0.3 inch in diameter and 0.25 inch long. An array of this type is known to approximate a homogeneous,

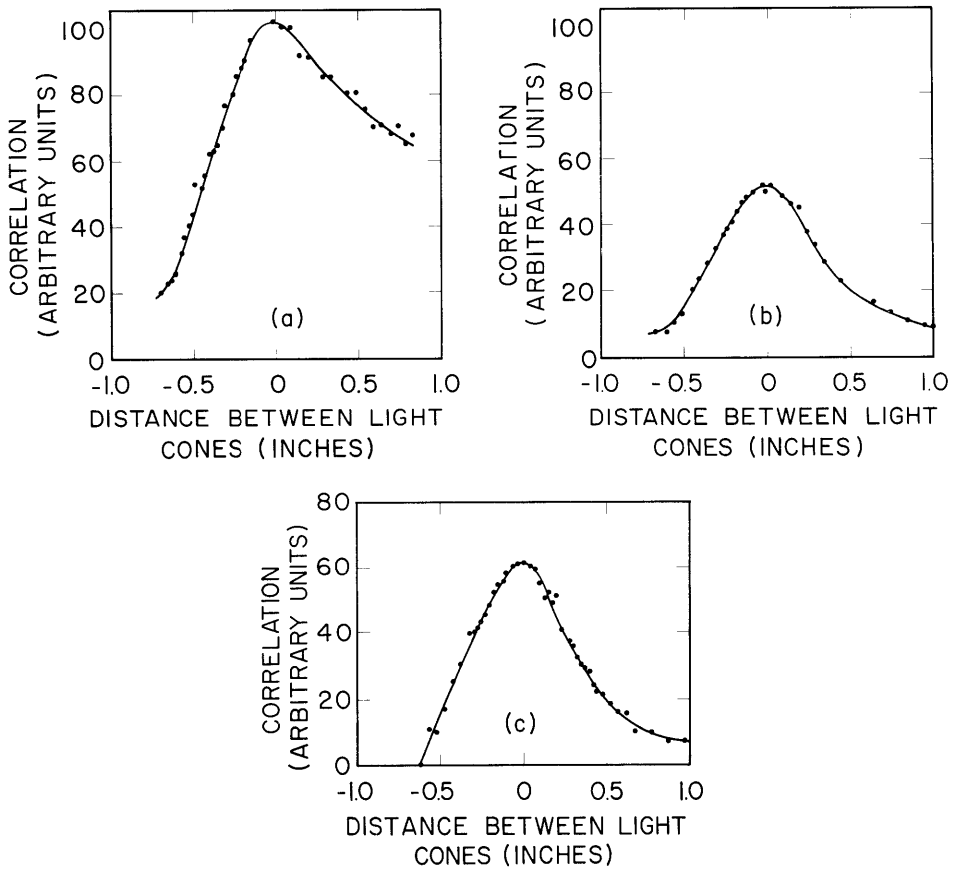

Fig. II-9. Correlation measurements of turbulence behind a planar array of obstacles. Static gas pressure, 4.7 mm Hg; flow velocity, Mach 0.99; Reynolds number, 2800. In (a) the turbulence was measured 6 inches down stream from the obstacle; in (b), 7 inches from the obstacle; and in (c), 8 inches from the obstacle.

turbulent field (1). On the abscissa of Fig. II-9 is plotted the separation between the light cones (as measured in a direction parallel to the flow). On the ordinate is plotted the amplitude of the product of the light fluctuations in the two cones. In Fig. II-9a the measurements were made at a distance of 6 inches downstream from the obstacle (this distance is for a juxtaposition of the light cones). Figure II-9b refers to a distance equal to 7 inches, and Fig. II-9c to a distance of 8 inches. We note that the width of the curves (and hence the characteristic size of the turbulence) decreases with increasing distance from the array of obstacles. Similar observations have been made in the past with hot wire anemometers inserted into the turbulent gas flow (1).

Figure II-10 illustrates correlation measurements of turbulence that was generated behind a free jet. The jet was produced by a nozzle of circular cross section with an exit diameter equal to 1 inch. The nozzle emptied air at supersonic velocity into the test section. Figure II-10a represents correlation measurements made at a distance of 7 inches from the output end of the nozzle, and Fig. II-10b shows measurements that were made at a distance of 8 inches.

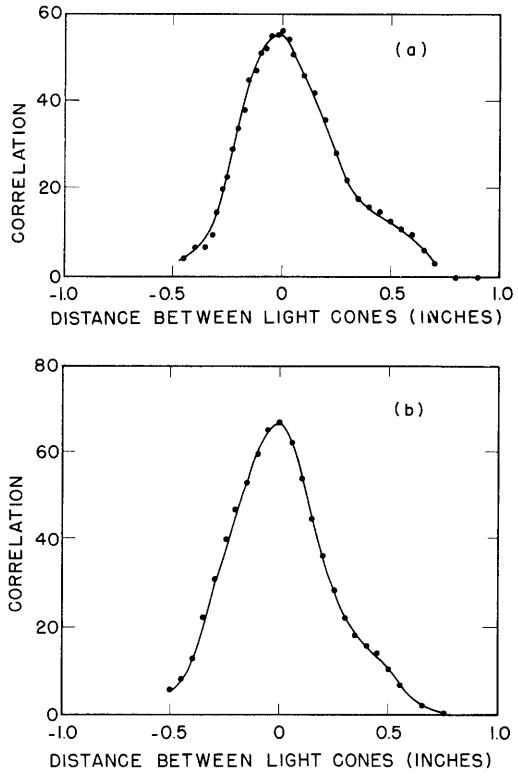

Fig. II-10. Correlation measurements of turbulence behind a free jet. Static gas pressure, 4.9 mm Hg; flow velocity, Mach 1.9; Reynolds number, 40,000. In (a) the measurements were made 7 inches away from the jet; in (b), 8 inches away.

The photograph of Fig. II-11 shows the average light emitted by the turbulent plasma downstream from the jet. The presence of the plasma illustrates nicely the various

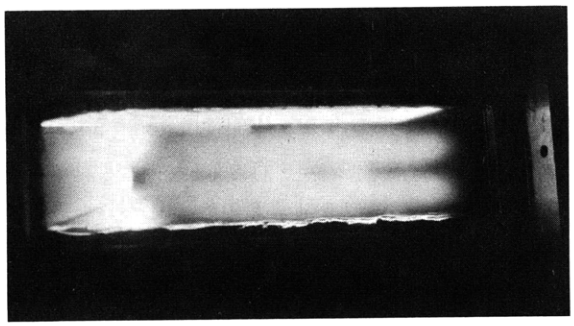

Fig. II-11. Photograph of the light emitted by the turbulent plasma behind the free jet.

pressure regions in the shock behind the free jet. Since the mean light intensity varies with position, an error is introduced into the correlation data shown in Fig. II-10. Measurements that were intended to correct for this error showed that the modifications of the correlation profile were small.

S. Gruber, G. Bekefi

References

1. G. K. Batchelor, The Theory of Homogeneous Turbulence (Cambridge University Press, London, 1956).

3. THE FOKKER-PLANCK EQUATION WITH SHORT-RANGE INTERACTIONS

Many authors (1,4,5) have written the Liouville equation in the form of a set of linked equations

$$\frac{\partial F_{1\ldots s}}{\partial t} = \left[\sum_{i=1}^{s} T_i \; ; \; F_{1\ldots s}\right] + \left[\sum_{i<j}^{s} \sum_{j=2}^{s} \psi_{ij} \; ; \; F_{1\ldots s}\right]$$

$$+ \frac{N-s}{V} \int \left[\sum_{i=1}^{s} \psi_{is+1} \; ; \; F_{1\ldots s+1}\right] dX_{s+1} \qquad (1)$$

in which the brackets are Poisson brackets, T_i and ψ_{ij} are the kinetic energies and the interparticle potentials, X_i is a six-dimensional phase-sapce vector $\{\vec{r}_i, \vec{p}_i\}$, and the s-particle function is defined as

$$F_{1\ldots s} = \frac{1}{V^{N-s}} \int D(X_1 \ldots X_N;t)\, dX_{s+1} \ldots dX_N$$

$$= F_{1\ldots s}(X_1 \ldots X_s;t) \tag{2}$$

where D satisfies Liouville's equation in 6-N dimensions.

Bogoliubov (1) has shown that, under the assumption of short-range forces, these equations lead to the Boltzmann equation for the one-particle function F_1. The short-range assumption has made the integral term in Eq. 1 negligible for $s > 1$. Sptizer (2) and Allis (3) have used the Boltzmann collision integral to discuss plasmas. The resulting integrals diverge at long distances because the integral terms are not negligible for long-range Coulomb interactions. They were forced to employ the artificial device of cutting off the interactions at the Debye distance in order to remove this divergence.

The opposite approach has been to recognize that for Coulomb interactions the integral terms are large, while the single-particle interactions, the double summation in Eq. 1, are small. Treating these terms as perturbations on the two-body distribution F_{12} leads to a Fokker-Planck type of term in the equation for the one-particle function F_1. This procedure has been followed by Rosenbluth (4), and by others. In this case integrals diverge at short distances because of the breakdown of the perturbation procedure.

An examination of this divergence may suggest a means of avoiding it. In all of the following discussion, assume a gas composed of particles that are all of one sign, with the usual neutralizing background. One can show that under this perturbation scheme, all of the distributions $F_{1\ldots s}$ are expressible in terms of one-particle distributions $f_1(x_1)$ and two-particle correlations $f_{12}(x_1,x_2)$, if the three-particle correlations $f_{123}(x_1, x_2, x_3)$ is neglected. This assumption has been discussed in detail by Rosenbluth (4) and Tchen (5).

If we define a parameter

$$\lambda = \left\langle \frac{f_{12}}{f_1 f_2} \right\rangle_{\text{average}} \tag{3}$$

it can be shown that λ is of the same order of magnitude as the individual interaction terms $[\psi_{ij};F_{1\ldots s}]$ in Eq. 1, and that neglecting f_{123} is equivalent to neglecting terms in λ^2. After some cancellation, we obtain to first order in λ:

$$\frac{\partial f_1}{\partial t} = [T_1;f_1] + \frac{N}{V} \int [\psi_{12};f_1 f_2 + f_{12}]\, dX_2$$

$$\frac{\partial f_{12}}{\partial t} = [T_1+T_2;f_{12}] + [\psi_{12};f_1f_2] + \frac{N}{V}\int [\psi_{13};f_{23}f_1]\, dX_3$$

$$+ \frac{N}{V}\int [\psi_{23};f_{13}f_2]\, dX_3 + \frac{N}{V}\int [\psi_{13}+\psi_{23};f_{12}f_3]\, dX_3 \qquad (4)$$

The correlation equation yields a correlation function, f_{12}, that has a pole at $\vec{r}_{12} = 0$, and hence the integral $\int[\psi_{12};f_{12}]\, dX_2$ diverges. The other integrals such as $\int[\psi_{12};f_{23}f_1]\, dX_2$ do not diverge because the singularities of ψ_{12} and f_{23} are not superposed.

This comes about because in our approach to the set of Eqs. 1 we did not correctly allow for the circumstance $|r_{12}| \to 0$. We may correct this situation in the set of Eqs. 1 by not assuming the interaction ψ_{12} to be small, and by keeping the other pairs ψ_{ij} of order λ. We then allow particles 1 and 2 to approach one another, but allow for only distant encounters for the other pairs. Whereas before we had essentially considered free particles perturbed by distant encounters, we now consider a two-body collision perturbed by distant encounters with other particles.

In general terms, we can see what is happening. In Eq. 1 the bracket of ψ_{12} with $F_{1\ldots s}$ may be viewed as an operator that is generating correlations. Usually this is small – of order λ – so we may obtain correlations to first order in λ by substituting $F_{1\ldots s}$ to zero order in λ in this term, $F_{1\ldots s} = \prod_{i=1}^{s} f_i$. If this term is not really small, this procedure is invalid and we must not linearize in λ.

In the present problem, we assume that all correlation operators except ψ_{12} are of order λ. This ensures that the integral $\int[\psi_{12};f_{12}]\, dX_2$ will not diverge, since f_{12} will go rapidly to zero as $|\vec{r}_{12}| \to 0$. (Remember that all charges are of the same sign.)

Introduction of the above-mentioned modification leads to the result that the basic relation is not

$$F_{1\ldots s} = \prod_{i=1}^{s} f_i + \sum_{i<j}^{s} \prod_{k\neq i,j}^{s} f_h f_{ij} \qquad (5)$$

but rather that a three-particle function is necessary.

$$F_{1\ldots s} = F_{12}\left[\prod_{i>3}^{s} f_i + \sum_{\substack{i<j \\ \neq 1,2}}^{s} \prod_{\substack{k\neq i,j \\ \neq 1,2}}^{s} f_h f_{ij}\right]$$

$$+ \sum_{i=3}^{s} \prod_{\substack{j\neq i \\ \neq 1,2}}^{s} f_j F^1_{123}$$

where F^1_{123} satisfies

$$\frac{\partial F^1_{123}}{\partial t} = \left[T_1+T_2+T_3+\psi_{12};F^1_{123}\right] + \int \left[\psi_{34};F^1_{124}f_3\right] dX_4$$

$$+ \int \left[\psi_{14}+\psi_{24}+\psi_{34};F^1_{123}f_4\right] dX_4$$

$$+ \left[\psi_{23}+\psi_{13};F_{12}f_3\right] + \int \left[\psi_{14}+\psi_{24};F_{12}f_{34}\right] dX_4 \qquad (6)$$

Note the occurrence of the weak coupling between particles 1 and 2 and the others. When F^1_{123} is substituted in the equation for F_{12}, the term

$$\int \left[\psi_{13}+\psi_{23};F^1_{123}\right] dX_3$$

will diverge because of the weak-coupling assumption between particles 1 and 3, and particles 2 and 3. This is directly analogous to the earlier divergence and occurs for the same reason. It is believed that the introduction of cutoffs in this term in the equation for F_{12} will have a much smaller effect than would the corresponding cutoff in the equation for F_1, that is, the dependence on the cutoff distance will be much weaker than logarithmic in the final equation for F_1.

The equation for F^1_{123} has been solved for a homogeneous plasma. When F_{123} is substituted in Eq. 1 for F_{12}, the resulting equation has many terms; some progress has been made in interpreting them. From one such term, it is found that the interaction ψ_{12}, whose Fourier transform is

$$4\pi i e^2 \int \frac{\vec{k}}{k^2} e^{i\vec{k}\cdot\vec{r}_{12}} d^3\vec{k}$$

is replaced by a potential whose transform when acting on particle 1 is

$$4\pi i e^2 \int \frac{\vec{k}\, e^{i\vec{k}\cdot\vec{r}_{12}}\, d^3\vec{k}}{k^2\left[1 + \frac{\omega_p^2}{k^2}\int d^3\vec{V}_3 \vec{k}\cdot\frac{\partial f_3}{\partial \vec{V}_3}\,\delta_-(\vec{k}_3\cdot(\vec{V}_3-\vec{V}_1))\right]} \qquad (7)$$

where

$$\delta_-(X) = \pi\delta(X) - iP\left(\frac{1}{X}\right)$$

In the limit $\vec{v}_1 \to 0$ the denominator in expression 7 represents the Debye cloud; for $\vec{v}_1 \neq 0$, the cloud is elongated. Thus we have a pseudo potential, caused by the

long-range terms, which goes to zero outside the Debye length. Use of this potential would have obviated the artificial cutoff used in the Boltzmann collision integral.

D. E. Baldwin

References

1. N. N. Bogoliubov, Problems of Dynamic Theory in Statistical Physics, Translation AEC-tr-3852, U.S. Atomic Energy Commission, Technical Information Service, 1960.

2. L. Spitzer, Jr., Physics of Fully Ionized Gases (Interscience Publishers, Inc., New York, 1956).

3. W. P. Allis, Motions of ions and electrons, Handbuch der Physik, edited by S. Flügge, Vol. 21, pp. 383-444 (Springer Verlag, Berlin, 1956); Technical Report 299, Research Laboratory of Electronics, M.I.T., June 13, 1956.

4. N. Rostocker and M. Rosenbluth, Phys. Fluids 3, 1 (1960).

5. C. M. Tchen, Phys. Rev. 114, 394 (1959).

4. NEGATIVE ABSORPTION OF SYNCHROTRON RADIATION FROM A NONTHERMAL ELECTRON GAS WITH A NONISOTROPIC VELOCITY DISTRIBUTION

In this report we present a simple method for relating the frequency of the radiation, angle of propagation with respect to the magnetic field, and certain characteristics of the electron velocity distribution to determine whether negative or positive absorption will take place. Also, we derive an expression for the absorption coefficient of the extraordinary electromagnetic wave, propagating through a nonthermal, low-density, uniform, relativistic electron gas in the presence of an external magnetic field. Collisions are neglected. Finally, we discuss an approximate equation for the absorption coefficient that is valid at low energies, and apply it to the simple case of a triangular velocity distribution.

The absorption coefficient is determined from an expression of the form

$$a_{\omega}^{\perp}(\theta) = \int a_1^{\perp}(\theta)\, f\, d\vec{p} \tag{1}$$

where $a_1^{\perp}(\theta)$ is the absorption per electron of momentum $\vec{p}$, for the extraordinary wave ($\perp$), per unit frequency per unit solid angle in the direction θ to the magnetic field, and f is the distribution function. Trubnikov (1) shows that $a_1^{\perp}(\theta)$ is related to the spontaneous emission coefficient, $\eta_1^{\perp}(\theta)$. The relation is

$$a_1^{\perp}(\theta) = \frac{8\pi^3 c^2}{\omega^2 \mathscr{E}} \left[\eta_1^{\perp} + \mathscr{E}\, \frac{\cos\theta}{c} \frac{\partial \eta_1^{\perp}}{\partial p_{\parallel}} + \mathscr{E}\, \frac{\mathscr{E}/c - p_{\parallel} \cos\theta}{c p_{\perp}} \frac{\partial \eta_1^{\perp}}{\partial p_{\perp}} \right] \tag{2}$$

where $\mathscr{E}$ is the total energy, and $\perp$ and $\|$ refer to directions perpendicular and parallel to the magnetic field.

The spontaneous emission by a single electron in a magnetic field (1, 2) is

$$\eta_1^{\perp}(\theta) = \frac{q^2\omega^2}{2\pi c} \sum_{n=1}^{\infty} \beta_{\perp}^2 J_n'^2 \left(\frac{\omega\beta_{\perp} \sin\theta}{\omega_H(1-\beta^2)^{1/2}} \right) \delta\left[n\omega_H(1-\beta^2)^{1/2} - \omega(1-\beta_{\|}\cos\theta) \right] \tag{3}$$

Here, $J_n'(\ )$ is the derivative with respect to its entire argument of the Bessel function of order n; $\delta[\ ]$ is the Dirac delta function; β is the velocity ratio v/c; H is the magnetic field intensity; n is a positive integer referring to the n^{th} harmonic of the cyclotron radiation; and $\omega_H = qH/mc$, where m is the electron rest mass.

Equations 1, 2, and 3 are combined and integrated over the variable $p_{\perp}$ to obtain (for the n^{th} term)

$$\alpha_{\omega_n}^{\perp}(\theta) = -\frac{8\pi^3(qmc)^2}{\omega} \int_{-\infty}^{\infty} J_n'^2\left(\sqrt{\chi}\,\frac{\omega}{\omega_H}\sin\theta \right) \left\{ \chi\cos\theta \left[\frac{\partial f}{\partial p_{\|}} \right]_* + \sqrt{\chi}\,\frac{n\omega_H}{\omega} \left[\frac{\partial f}{\partial p_{\perp}} \right]_* \right\} dp_{\|} \tag{4}$$

where

$$\chi = \left(\frac{n\omega_H}{\omega} + \frac{p_{\|}}{mc}\cos\theta \right)^2 - \left(1 + \frac{p_{\|}^2}{m^2c^2} \right) \tag{5}$$

Here, the asterisk indicates the substitution of $\sqrt{\chi}$ for $p_{\perp}/mc$. This substitution occurs because integration of Eq. 1 with respect to $p_{\perp}$ relates $p_{\perp}$ and $p_{\|}$ through the delta function in Eq. 3.

Certain qualitative features (and even orders of magnitude) of the behavior of $\alpha_{\omega_n}^{\perp}(\theta)$ can be determined if we assume that $f = f_{\|}f_{\perp}$ and approximate $f_{\|,\perp}$ by simple triangular

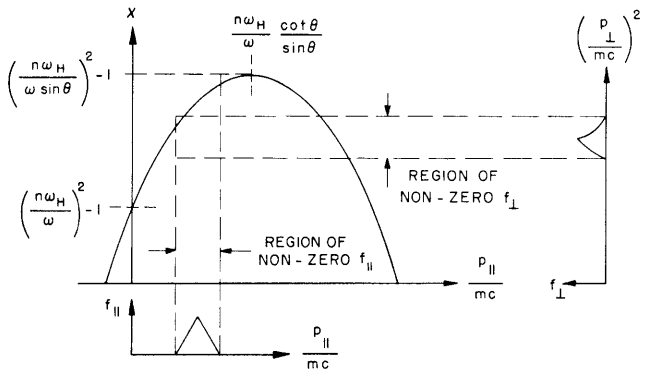

Fig. II-12. χ versus $p_{\|}/mc$ at constant ω and θ.

distributions in momentum space. The half-widths, in units of momentum, are $d_{||,\perp}$; the peaks occur at $p_{||_M,\perp_M}$.

Equation 5, with $p_\perp = mc\sqrt{\chi}$, represents a parabola in the χ, $p_{||}/mc$ plane when ω and θ are held constant. The ordinary Doppler shift and the relativistic Doppler shift permit absorption and emission of radiation in the θ direction at a frequency ω only by those electrons whose momentum components are related by Eq. 5. Figure II-12 shows this parabola with the distribution function superimposed.

Figure II-13 illustrates the region of the χ, $p_{||}/mc$ plane, where f is found to be nonzero. The lines 1, 2, 3, 4, and 5 are sections of different parabolas, labelled with respect to increasing ω, with θ held constant. The large rectangle is the region of nonzero f. Inspection of Eq. 4 reveals the following features. In region A, shown in Fig. II-13, the first term in the integrand of Eq. 4 contributes to negative absorption; the second term to positive absorption. In region B, the first and second terms both contribute to positive absorption. In region C, the first contributes to positive and the second to negative absorption. In region D, both contribute to negative absorption. The essential feature of the distribution function that defines the regions A, B, C, and D at their various mutual boundaries are the values of $p_{\perp_M}$ and $p_{||_M}$ at the maxima of $f_\perp$ and $f_{||}$. We merely choose triangular distributions for purposes of illustration and simplicity in calculation. (Note that we have chosen to illustrate the ascending arm of the parabola. In general, the region of nonzero f may occur anywhere on the parabola. The characteristics of regions A, B, C, and D obviously remain unchanged.)

When the electrons can be classed as weakly relativistic, and when $d_{||}/d_\perp \gg v/c$, the first term in the integrand of Eq. 4 is small compared with the second. If we properly choose the parabolas 1, 2, 3, 4, and 5 of Fig. II-13, the behavior of $\alpha^\perp_{\omega_n}(\theta)$ versus ω has the features shown in Fig. II-14a.

When the electrons are ultrarelativistic, and when $d_{||}/d_\perp \sim 1$, the parameter $\frac{n\omega_H}{\omega}$ is of the order of $\sqrt{\chi}$, and the two terms in the integrand of Eq. 4 are comparable (except, of course, when $\theta \to \pi/2$). Figure II-14b illustrates the case in which the first term in the integrand is larger than the second term.

The dashed lines in Fig. II-14 indicate the manner in which the behavior of $\alpha^\perp_{\omega_n}(\theta)$ versus ω would be modified when the true distribution function replaces its triangular approximation.

Equation 6 is a useful approximation to Eq. 4 for weakly relativistic electrons.

$$\alpha^\perp_{\omega_n}(\theta) \approx -\frac{8\pi^3(qmc)^2}{\omega}\,\frac{\left(\frac{\omega}{\omega_H}\sin\theta\right)^{2(n-1)}}{2^{2n}[(n-1)!]^2}\int_{-\infty}^{\infty}\left\{\chi^n\cos\theta\left[\frac{\partial f}{\partial p_{||}}\right]_* + \chi^{n-1/2}\,\frac{n\omega_H}{\omega}\left[\frac{\partial f}{\partial p_\perp}\right]_*\right\}dp_{||} \tag{6}$$

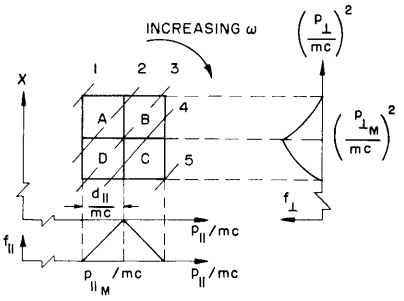

Fig. II-13. χ, $p_{||}/mc$ plane in the region of nonzero f.

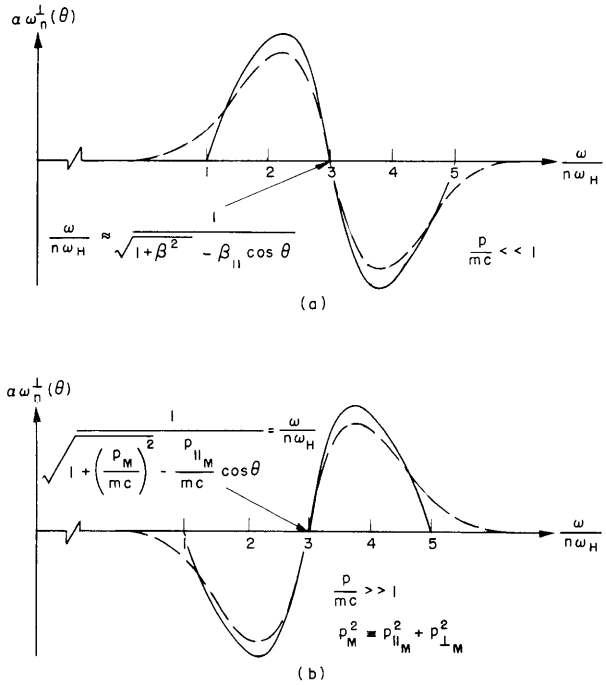

Fig. II-14. Plot of $a_{\omega_n}^{\perp}(\theta)$ versus $\omega/n\omega_H$: (a) weakly relativistic; (b) ultrarelativistic.

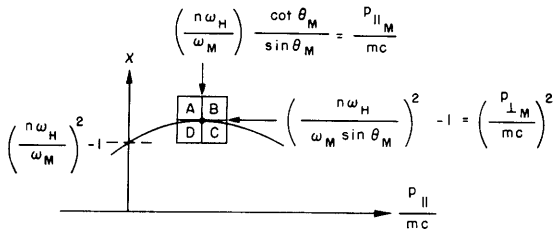

Fig. II-15. Determination of θ_M and ω_M.

The frequency range for negative absorption is contained between the points 3 and 5 in Fig. II-14a corresponding to the parabolas 3 and 5 in Fig. II-13. When the segments of the parabolas crossing the region of nonzero f in Fig. II-13 are approximated by straight line segments, this range is

$$\Delta\omega = \frac{\left| \frac{p_{\perp_M} d_\perp}{m^2c^2} - \frac{1}{2}\frac{d_\perp^2}{m^2c^2} - \left(\frac{p_{\parallel_M} d_\parallel}{m^2c^2} + \frac{1}{2}\frac{d_\parallel^2}{m^2c^2} \right) \sin^2\theta + \frac{d_\parallel}{mc}\cos\theta \right|}{1 + \frac{p_{\parallel_M}}{mc}\cos\theta} n\omega_H \tag{7}$$

This approximation is best as $\theta \to 0$. However, as $\theta \to \pi/2$, a better approximation is

$$\Delta\omega = \left| \frac{p_{\perp_M} d_\perp}{m^2c^2} - \frac{1}{2}\frac{d_\perp^2}{m^2c^2} \right| n\omega_H \tag{8}$$

Figure II-15 illustrates the situation of maximum amplification when the first term in the integrand of Eq. 6 is neglected.

The angle, θ_M, and frequency, ω_M, at which maximum amplification occur are given by

$$\theta_M = \cot^{-1}\left[\left(p_{\parallel_M}/mc \right)^2 \Big/ \left(1 + \frac{p_{\perp_M}^2}{m^2c^2} \right) \right]^{1/2} \tag{9}$$

$$\left(\frac{\omega}{n\omega_H} \right)_M = \frac{\left[\left(p_{\parallel_M}/mc \right)^2 \Big/ \left(1 + \frac{p_{\perp_M}^2}{m^2c^2} \right) \right]^{1/2}}{\frac{p_{\parallel_M}}{mc}\sin\theta_M} \tag{10}$$

When $\left(p_{\parallel_M}/mc \right)^2$ approaches zero, the limits for Eqs. 9 and 10 are

$$\theta_M \to \pi/2$$

$$\left(\frac{\omega}{n\omega_H} \right)_M \to \left[1 + \left(\frac{p_{\perp_M}}{mc} \right)^2 \right]^{-1/2}$$

Whenever Eq. 6 is a good approximation, $\left(p_{\parallel_M}/mc \right)^2$ is much smaller than 1. Thus, for the weakly relativistic case, maximum amplification will always occur in a direction very nearly $\theta \approx \pi/2$, and close to the frequency $\omega = n\omega_H \left[1 + \left(p_{\parallel_M}/mc \right)^2 \right]^{-1/2}$. Inclusion

of the first term in Eq. 6 reinforces this conclusion, since this term tends to decrease the amplification at smaller angles.

An approximate expression for the maximum amplification in the weakly relativistic case, with $d_{||}/d_{\perp} \gg v/c$, and $d \ll p_M$, is

$$\alpha^{\perp}_{\omega M_n}(\theta \approx \pi/2) \approx -\frac{8\pi^3 (qmc)^2}{2^{2n}[(n-1)!]^2}\left(\frac{p_{\perp M}}{mc}\right)^{2n-1}\int_{-\infty}^{\infty}\left[\frac{\partial f}{\partial p_{\perp}}\right]_* dp_{||} \tag{11}$$

For the triangular distribution function, we have

$$\left[\frac{\partial f}{\partial p_{\perp}}\right]_* = \frac{N}{\frac{p_{\perp M}}{mc}\left(\frac{d_{\perp}d_{||}}{m^2c^2}\right)^2 (mc)^5}\begin{cases} 0 & , \quad p_{||} < p_{||_M} - d_{||} \\ p_{||} - p_{||_M} + d_{||} & , \quad p_{||} < p_{||_M} \\ p_{||_M} + d_{||} - p_{||} & , \quad p_{||} > p_{||_M} \\ 0 & , \quad p_{||} > p_{||_M} + d_{||} \end{cases} \tag{12}$$

where N is the electron density.

Substituting Eq. 12 in Eq. 11, we obtain

$$\alpha^{\perp}_{\omega M_n}(\theta \approx \pi/2) \approx -\frac{8\pi^3 (q^2/mc)}{2^{2n}[(n-1)!]^2}\frac{N}{\omega_M}\frac{\left(\frac{p_{\perp M}}{mc}\right)^{2n-2}}{(d_{\perp}/mc)^2} \tag{13}$$

For the first harmonic, that is, n = 1, the maximum amplification is

$$\alpha^{\perp}_{\omega H_1}(\theta \approx \pi/2) \approx -0.54\,\frac{N}{\omega_H}\left(\frac{mc}{d_{\perp}}\right)^2 \text{ cm}^{-1} \tag{14}$$

For a mean electron energy of 10^3 ev, and magnetic field strength of 3×10^3 gauss, we have $p_{\perp M}/mc \approx 0.06$, and $\omega_H \approx 5.3 \times 10^{10}$ rad/sec. If $d_{\perp}/mc = 0.006$, and $N = 10^8$ cm, then $\alpha^{\perp}_{\omega M_1} \approx -30 \text{ cm}^{-1}$, and $\Delta\omega \approx 19 \times 10^6$ (approximately 3 mc).

More quantitative analyses of the dependence of $\alpha^{\perp}_{\omega_n}(\theta)$ on $\omega/n\omega_H$, θ, $d_{||,\perp}$, and $p_{||_{M'}\perp_M}$ are being carried out.

J. D. Coccoli

References

1. B. A. Trubnikov, Magnetic Emission of High Temperature Plasma, Translation AEC-tr-4073, U.S. Atomic Energy Commission, Technical Information Service, 1960.

2. G. A. Schott, Electromagnetic Radiation (Cambridge University Press, New York, 1912).

II-B. PLASMA ELECTRONICS*

Prof. L. D. Smullin
Prof. H. A. Haus
Prof. A. Bers
Prof. D. J. Rose
P. Chorney
J. R. Cogdell
L. J. Donadieu
T. H. Dupree
T. J. Fessenden
W. D. Getty
W. G. Homeyer
H. Y. Hsieh
A. J. Impink, Jr.
P. W. Jameson
W. Larrabee IV
L. M. Lidsky
D. L. Morse
S. D. Rothleder
C. L. Salter, Jr.
A. J. Schneider
P. E. Serafim
P. S. Spangler
A. W. Starr
M. C. Vanwormhoudt
R. C. Wingerson
S. Yoshikawa

1. THERMAL NOISE FROM PLASMAS

In a previous report (1) it was indicated that the noise generation of linear, lossy, electromagnetic media could be accounted for by postulating the existence of random driving-current sources. The correlation matrix $\phi(\bar{r}\,|\,\bar{s}, \tau)$ of these noise sources was found to bear a simple relation to the Green's current dyadic $g(\bar{r}\,|\,\bar{s}, \tau)$.

Because $\phi(\bar{r}\,|\,\bar{s}, \tau)$ satisfies the microscopic reversibility condition and because the matrix $g(\bar{r}\,|\,\bar{s}, \tau)$ is zero for all $\tau < 0$ (causality), we are able to find the Onsager relation satisfied by the current dyadic $g(\bar{r}\,|\,\bar{s}, \tau)$. This relation is

$$g(\bar{r}\,|\,\bar{s}, T) = \tilde{g}_{(-)}(\bar{s}\,|\,\bar{r}, T)$$

Here, the tilde indicates transposition of the matrix, and $g_{(-)}(\bar{r}\,|\,\bar{s}, T)$ represents the Green's current dyadic for a medium that is identical to that under study but for which any impressed dc magnetic field is reversed. If there is no dc magnetic field, $g_{(-)}(\bar{r}\,|\,\bar{s}, T)$ is identical to $g(\bar{r}\,|\,\bar{s}, T)$. This relation generalizes the known Onsager relation for the conductivity of a medium, and applies to non-Markovian media. It is valid not only for media for which the relation between the current density and the electric field is a local relation, but also for more complicated "operator" media.

Previously, we only applied our formalism to one-dimensional plasmas, but now we have extended the treatment to include three-dimensional plasmas. Most of the characteristics of the correlation matrix $\phi(\bar{r}\,|\,\bar{s}, T)$ which were obtained in the one-dimensional case remain unaltered.

If a plasma is treated by starting from the linearized Boltzmann equation, we find that it is an "operator" medium, namely, one in which the induced current density at some point is dependent upon the electric field over the whole medium. Correspondingly, we find that there is a nonvanishing correlation between the noise sources at different points and the spectra of the fluctuations are not white. We thus find a situation very different from that encountered in ordinary networks. This leads us to inquire into the question of whether or not the current fluctuations could be traced back to a more

*This work was supported in part by National Science Foundation under Grant G-9330.

fundamental cause. This is found to be the case. Instead of introducing a Langevin term in Maxwell's equations, we introduce a random driving term in the linearized Boltzmann equation. This driving term gives rise to fluctuations in the distribution function of the electrons, and hence to current fluctuations. We find that this results in the correct noise behavior of a plasma in thermodynamic equilibrium if we make the following hypotheses:

(a) The correlation of the driving term is zero for all delays different from zero.

(b) At some instant of time, the electrons belonging to any velocity group $d\tau_u$ are randomly (Poisson) distributed over configurational ($\vec{r}$) and velocity ($\bar{u}$) space with a density $f^o(\bar{r}, \bar{u})$, and the distributions belonging to different velocity groups are independent. We denote by $d\tau_u$ a volume element of velocity space centered around some velocity $\bar{u}$, and the function $f^o(\bar{r}, \bar{u})$ represents the equilibrium distribution of the electrons.

M. C. Vanwormhoudt

References

1. M. C. Vanwormhoudt, Thermal noise from plasmas, Quarterly Progress Report No. 60, Research Laboratory of Electronics, M.I.T., Jan. 15, 1961, pp. 30-32.

2. COMPLEX PROPAGATION CONSTANTS IN BIDIRECTIONAL WAVEGUIDES

In Quarterly Progress Report No. 61 (pages 23-29), it was predicted that a waveguide completely filled with a uniform, cold, collisionless, longitudinally magnetized plasma could exhibit complex propagation constants on a limited frequency band for certain combinations of the characteristic parameters. Computations are being performed to test this prediction and will be reported when results are obtained.

In an early report, Barzilai (1) investigated the guided wave propagation between two perfectly conducting, infinite, parallel planes which bound a uniform, lossless, longitudinally magnetized ferrite. Because of the configuration, this system is bidirectional. Barzilai found from a direct solution of the boundary-value problem that it was possible, under certain conditions, to support waves with complex propagation constants in this waveguide. This fact is mentioned to support the suspicion that complex propagation can also exist for the plasma waveguide.

In a more recent article, propagation in longitudinally magnetized, uniform, lossless, ferrite waveguides has been examined (2). It was found from a quasi-static approximation that these waveguides exhibit backward waves for frequencies in the vicinity of the gyromagnetic resonance. The quasi-static theory is valid as long as this resonance is far below the cutoff frequency of the empty waveguide. With these results in mind, an argument similar to the one used to justify the complex waves in plasma waveguides (3,4) may be applied to the ferrite-filled waveguide.

As the cutoff frequency of the empty waveguide is allowed to become comparable to the gyromagnetic frequency, we expect, on a heuristic basis, that there would be an interaction between the quasi-static ferrite mode and the empty-waveguide mode. Since the quasi-static ferrite mode is backward wave, there is a frequency band in the vicinity of synchronism in which the propagation constant is complex. This argument, we recall, is based on the theory of coupling of modes (5). It should be emphasized that the coupling-of-modes theory applies only to weak coupling and is therefore a first-order theory. The systems that we are treating cannot really be partitioned into weakly coupled subsystems, and the coupling of modes theory is used heuristically in order to present a plausibility argument for complex propagation constants in lossless, passive waveguides.

One point worth mentioning in connection with complex propagation constants in general is that even though complex waves in lossless, passive systems carry no net power when they are excited individually (3, 4), they can carry power when they are excited in pairs. This comes about because modes having propagation constants that are complex conjugates of one another are not orthogonal (1, 5, 6). Thus power flow arises from the cross terms in the Poynting vector associated with a system that is simultaneously supporting two waves having complex conjugate propagation constants.

P. Chorney

References

1. G. Barzilai, Propagation of electromagnetic waves in gyromagnetic media, Research Report R-578-57, PIB-506, Microwave Research Institute, Polytechnic Institute of Brooklyn, May 7, 1957.

2. A. W. Trivelpiece, A. Ignatius, and P. C. Holscher, Backward waves in longitudinally magnetized ferrite rods, J. Appl. Phys. 32, 259 (1961).

3. P. Chorney, Power, energy, group velocity, and phase velocity in bidirectional waveguides, Quarterly Progress Report No. 60, Research Laboratory of Electronics, M. I. T., Jan. 15, 1961, pp. 37-46.

4. P. Chorney, Power and energy relations in bidirectional waveguides, Proc. Symposium on Electromagnetics and Fluid Dynamics of Gaseous Plasmas, New York, April 1961 (to be published by the Polytechnic Press, New York).

5. J. R. Pierce, Coupling of modes of propagation, J. Appl. Phys. 25, 179 (1954).

6. D. L. Bobroff and H. A. Haus, Orthogonality of modes of propagation in electronic waveguides, Proc. Symposium on Electronic Waveguides (Polytechnic Press, New York, April 1958), pp. 407-414.

3. MAGNETOHYDRODYNAMIC AC GENERATORS

a. SIMPLE MODEL OF A CIRCUIT

It has been shown that electromagnetic power gain may be achieved by coupling of a plasma stream in a dc magnetic field to a traveling-wave circuit (1). It has also been

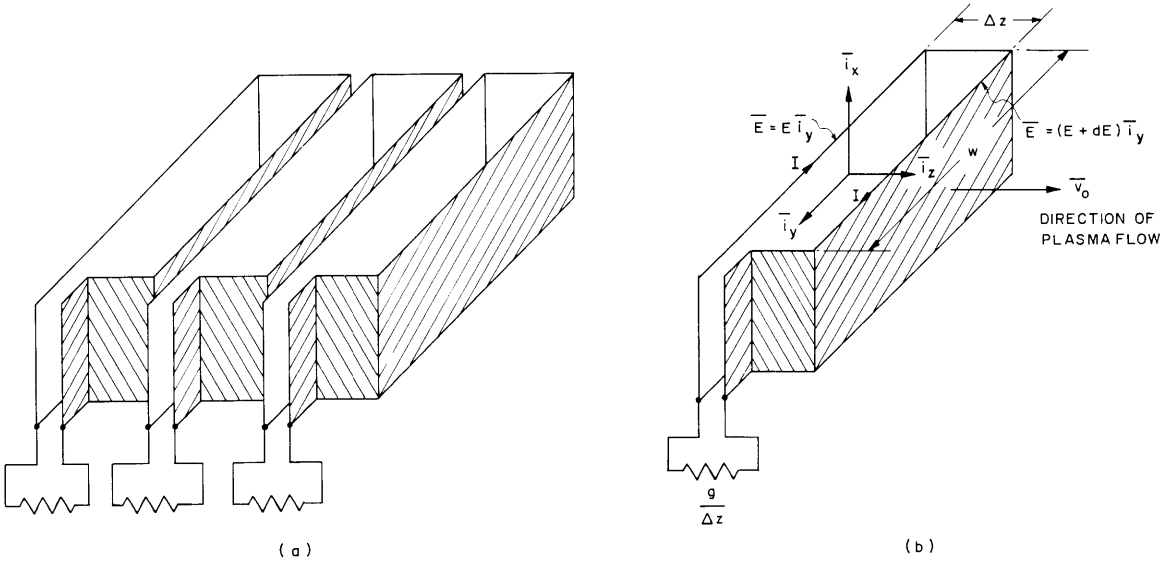

Fig. II-16. (a) The distributed circuit. (b) The choice of coordinates.

shown that self-sustained oscillations can exist in a single coil traversed by a plasma stream without the use of any additional (capacitive) energy-storage elements (2). From the practical point of view, a traveling-wave circuit is undesirable for magnetohydrodynamic power generation because it requires external capacitive energy-storage elements. A single lumped coil does not lead to growing waves, a mechanism that is likely to be used for power generation; a system consisting of a combination of lumped coils cannot be characterized by a simple differential equation.

A model of a circuit has been devised that combines the analytic simplicity of a distributed circuit and the constructional simplicity of a circuit without capacitive energy-storage elements. The one-dimensional circuit model is shown in Fig. II-16. Each winding is assumed to be permeable to a plasma flow in the z-direction. The loading on each winding is a conductance $(g/\Delta z)$ mho. The current per unit height is

$$I = \left(\frac{g}{\Delta z}\right) V = w\left(\frac{g}{\Delta z}\right) \Delta E \tag{1}$$

The "driving" current per length Δz, J_d, of the circuit is

$$J_d = -\frac{\Delta J}{\Delta z} \tag{2}$$

We thus have in the limit of a very short winding span

$$J_d = -\lim_{\Delta z \to 0} wg \frac{\Delta E/\Delta z}{\Delta z} = -wg \frac{d^2E}{dz^2} \tag{3}$$

If one uses Eq. 1 in the one-dimensional compressional wave amplifier (1), or the Alfvèn wave amplifier (2), one obtains for the propagation constant of the perturbed fast and slow waves, $\beta_{\pm}$,

$$\beta_{\pm} = \frac{\omega}{v_o \pm c} + \delta \tag{4}$$

with

$$\delta = \mp j \frac{\omega^2 \mu_o g w}{(v_o \pm c)^2} \frac{c_b^2}{c} \tag{5}$$

where v_o is the dc velocity of the plasma, c_b is the Alfvèn velocity, and

$$c = \left(c_s^2 + c_b^2\right)^{1/2}$$

for a compressional wave amplifier, with c_s, the sound velocity, and

$$c = c_b$$

for the Alfvèn wave amplifier. The slow wave is found to grow exponentially.

A more realistic three-dimensional version of the circuit is shown in Fig. II-17. With this model, a three-dimensional analysis of a compressional wave amplifier of the

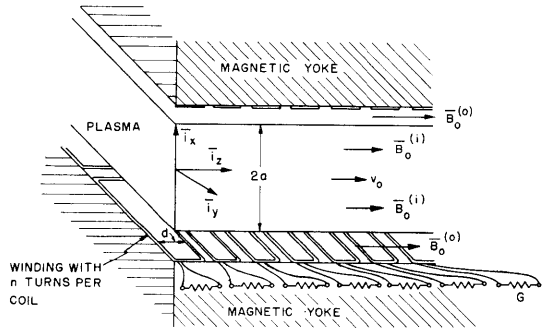

Fig. II-17. Alfvèn-wave amplifier with three-dimensional version of winding.

geometry shown in a previous report (3) has been carried out. The three-phase windings of that analysis were replaced by the windings of Fig. II-17. The resulting propagation constant for weak coupling reduces to a form very similar to that of Eq. 5

$$\delta = \mp j \frac{\omega^2 \mu_o n G d w}{2a(v_o \pm c)^2} \frac{c_b^2}{c}$$

A practical coil represented by this equation would have to possess a span that is short compared with the wavelengths of the pertinent waves in the plasma.

b. TWO-DIMENSIONAL ANALYSIS OF ALFVÈN-WAVE AMPLIFIER

The one-dimensional analysis of a plasma drifting with a uniform velocity v_o parallel to a dc applied magnetic field has shown the possibility of achieving gain through coupling of the (incompressional) waves to a circuit (4). An essential requirement for the gain mechanism to exist is that the plasma be free to move in a direction transverse to v_o. A physical device operating on this principle must employ a plasma of finite transverse extent unimpeded in its transverse motion. A plasma flow along a dc magnetic field, with its pressure balanced by currents in the plasma surface, is appropriate for this purpose.

An analysis has been carried out for the two-dimensional geometry shown in Fig. II-17 under the following assumed conditions:

(a) The (time-average) pressure p_o and velocity v_o are uniform inside the plasma.

(b) The plasma is perfectly conducting.

(c) The dc surface current balances pressure.

(d) A distributed coil winding as described in Section II-B. 3a is used, backed by highly permeable magnetic material.

(e) All equations are linearized.

With an assumed dependence $\exp(j\omega t - j\beta_z z - j\beta_x x)$, for β_x inside the plasma, we have

$$\beta_x = \pm \left[\frac{\left(\omega_r^2 - \beta_z^2 c_b^2\right)\left(\omega_r^2 - \beta_z^2 c_s^2\right)}{c^2\left(\omega_r^2 - \frac{c_b^2 c_s^2}{c^2}\beta_z^2\right)} \right]^{1/2}$$

where $\omega_r = \omega - v_o\beta_z$, and the other symbols have been explained in Section II-B. 3a.

The boundary conditions at x = a, may be expressed as follows: The normal component of the ac magnetic field must satisfy the equation

$$B_x^{(o)} - B_x^{(i)} = \mu_o K_o \frac{\partial \xi}{\partial z}$$

where K_o is the surface current ($K_o > 0$), and ξ is the displacement of the surface. The ac pressure and ac tangential component of B must satisfy the relation

$$p + \frac{B_o^{(i)} B_z^{(i)}}{\mu_o} = \frac{B_o^{(o)} B_z^{(o)}}{\mu_o}$$

With these boundary conditions, we find for the case in which there is a very small distance between the plasma surface and the windings, and for relatively small G,

$$\beta_z = \frac{\omega}{v_o \pm c_b} + \delta$$

with

$$\delta = \mp j \left(\frac{B_o^{(o)}}{B_o^{(i)}} \right)^2 \frac{\omega^2 \mu_o G d w}{2a(v_o \pm c_b)^2} c_b$$

The expression is very similar to that of the compressional wave amplifier for negligible $c_s (\ll c_b)$. The gain of the Alfvèn-wave amplifier is increased by the square of the ratio of the outside to inside magnetic field.

H. A. Haus

References

1. H. A. Haus, Magnetohydrodynamic ac generators, Quarterly Progress Report No. 60, Research Laboratory of Electronics, M. I. T., Jan. 15, 1961, pp. 46-50.

2. H. A. Haus, The compression-wave magnetohydrodynamic generator, Quarterly Progress Report No. 61, Research Laboratory of Electronics, M. I. T., April 15, 1961, pp. 31-33.

3. Ibid., see Fig. II-11, p. 32.

4. H. A. Haus, Alfvèn-Wave Amplifier, Quarterly Progress Report No. 61, op. cit., pp. 29-31.

4. LARGE-SIGNAL ELECTRON-STIMULATED PLASMA OSCILLATIONS

The linear time-harmonic analysis of the interaction between an electron beam and a plasma predicts that longitudinal traveling waves that grow exponentially with distance in the direction of the electron-beam flow may exist. Numerical calculations based on this analysis indicate that growth rates, which are sufficiently large to cause nonlinear, large-amplitude oscillations of the beam and plasma electrons, can be obtained in a system consisting of a moderate-perveance electron-beam gun ($k \approx 10^{-6}$) and a low-temperature plasma (1, 2). In the experiment to be discussed here, a large-signal oscillation is observed in a system consisting of an electron gun that produces a pulsed beam of approximately 1 amp at 10 kv and a plasma generated by the electron beam during each pulse. A general description of this experiment and further details about the apparatus have been given in a previous report (3). In this report, the point of view has been taken that the observed large-amplitude oscillations are the result of an electron beam-plasma interaction. This assumption has been justified by measurements and observations made during the experiment. Studies are underway to determine whether the beam-plasma interaction that produces the large-amplitude oscillations is

the spatially growing traveling-wave type previously referred to, or another type such as a standing wave in the interaction region, which grows exponentially with time.

An electron gun with a perveance of 1×10^{-6} $I/V^{3/2}$ and maximum current of 2.2 amps generates a pulsed beam current. The cathode is magnetically shielded. At the beginning of each 3-μsec pulse of beam current, a plasma is generated by ionizing collisions between the beam electrons and argon atoms. We operate at gas pressures of 10^{-4}-10^{-3} mm Hg in the path of the beam. In this pressure range, the mean-free path of an electron is several times the length of the apparatus. During the initial period, the loss of the electrons and ions produced by the beam is mainly axial, since the applied magnetic induction of several hundred gauss is sufficient to prevent transverse loss of electrons. The actual loss of particles is negligible during the pulse duration; therefore, the plasma density resulting from ionization is given approximately by

$$n_p = 7.1\, n_b\, p\tau \tag{1}$$

where n_p and n_b are the plasma and beam electron densities, respectively; p is the gas pressure in μ Hg; and τ is the time measured from the beginning of the pulse in μsec. At the time t, when the oscillations begin, the plasma resonant frequency ω_{pp} that is calculated by using the density n_p given by Eq. 1 is found to be of the same order of magnitude as the electron cyclotron frequency, ω_c. Therefore, in the analysis of the beam-plasma interaction, the effect of a finite magnetic field must be considered. Also, the analysis must include the effect of the finite diameter of the beam and plasma. As a first approximation, the dispersion equation for a beam and plasma in a filled drift tube of radius b is used. The longitudinal propagation constant β_z for this system is approximately

$$\beta_z = \beta_e\left[\frac{1}{1 + B^2} \pm j\,\frac{B}{1 + B^2}\right] \tag{2}$$

where

$$B^2 = \frac{\beta_{pb}^2}{\beta_T^2\left(1 + \dfrac{\omega_{pb}^2}{\omega_c^2}\right)}\,\frac{\omega^2 - \omega_c^2}{\omega_c^2 + \dfrac{\omega_{pp}^2}{1 + \dfrac{\omega_{pb}^2}{\omega_c^2}} - \omega^2} \tag{3}$$

Equation 2 is subject to the restriction (4) that $\beta_e \ll \beta_c$. The quantities ω_{pp} and ω_{pb} are the plasma resonant frequency of the plasma and beam, respectively; $\beta_{pb} = \omega_{pb}/v_o$, $\beta_c = \omega_c/v_o$, $\beta_e = \omega/v_o$; and v_o is the dc beam velocity. The radial wave number β_T is given by

$$\beta_T b = 2.504 \tag{4}$$

for the lowest order mode, which is the only mode considered. We find complex β_z for B^2 positive, or

$$\omega_c < \omega < \left(\omega_c^2 + \frac{\omega_{pp}^2}{1 + \frac{\omega_{pb}^2}{\omega_c^2}} \right)^{1/2} \tag{5}$$

An equation for $\alpha/\beta_e = \text{Im}\,(\beta_z/\beta_e)$ is obtained from Eqs. 2 and 3. If $\omega_{pb} \ll \omega_c$, the normalized growth constant α/β_e is sharply peaked near $\left(\omega_{pp}^2+\omega_c^2\right)^{1/2}$.

The electron beam is assumed to be velocity-modulated and current-modulated by random processes before it enters the high gas-pressure region where the plasma is generated. As the beam flows through and interacts with the plasma, the random fluctuations at frequencies near $\left(\omega_{pp}^2+\omega_c^2\right)^{1/2}$ are selectively amplified by the interaction. The random fluctuation downstream will no longer have a frequency-independent power spectrum, but will have one that is sharply peaked near $\left(\omega_{pp}^2+\omega_c^2\right)^{1/2}$. The mean square of a fluctuating quantity, such as electron velocity or current, will be proportional to the quantity

$$G_o = \int_{-\infty}^{\infty} \exp 2\alpha(\omega)\, L\, d\omega \tag{6}$$

where L is an arbitrary distance downstream from the point of entry of the electron beam. The constant of proportionality will be the input mean square of the quantity per unit frequency. Using the fact that α/β_e is sharply peaked, we can obtain an approximate integration of Eq. 6 by expanding α/β_e in a Taylor's series about the frequency ω_M at which the maximum value of α/β_e occurs. Obviously, this frequency is determined by B = 1. The resulting expression for α/β_e is

$$\frac{\alpha}{\beta_e} = \frac{1}{2} - \frac{1}{4}\,\frac{\omega_M^2}{\omega_{pp}^4}\,\frac{\beta_T^4}{\beta_{pb}^4}\,(\omega-\omega_M)^2 \tag{7}$$

where $\omega_M^2 = \omega_c + \omega_{pp}^2\left(1+\beta_{pb}^2/\beta_T^2+\beta_{pb}^2/\beta_c^2\right)$. It is assumed that β_{pb}^2/β_c^2 and β_{pb}^2/β_T^2 are small compared with unity. Equation 6 is evaluated by assuming that $\beta_e = \omega_M/v_o \equiv \beta_M$. The result is

$$G_o = \sqrt{\frac{\pi}{2}}\,\frac{e^{\beta_M L}}{(\beta_M L)^{1/2}} \cdot \frac{\omega_{pp}^2}{\omega_M} \cdot \frac{\beta_{pb}^2}{\beta_T^2} \tag{8}$$

Dissipative mechanisms, such as plasma electron thermal energies and elastic electron-atom collisions, are omitted in this analysis, and therefore the maximum amplification rate of $\beta_M/2$ is probably too large. On the other hand, the assumption of a filled drift tube imposes the boundary condition of zero tangential electric field at the boundary of the beam and plasma. This restriction will reduce the ac electric field in the plasma and, therefore, this model may underestimate the growth rate. Only a solution of a more general dispersion relation will answer this and other questions regarding the approximate dispersion equation. Such a numerical solution is now in progress.

A reduced amplification rate would primarily affect the over-all gain, G_o, through the exponential factor in Eq. 8. The main purpose of studying Eq. 8 is to determine how the beam radius b, the plasma frequency ω_{pp}, and the cyclotron frequency ω_c affect the gain. It is subject to the restriction that $\omega_{pp} < \omega_c$ and, therefore, it can be used only during the period of time from the beginning of the plasma generation to the time when $\omega_{pp} \approx \omega_c$. In these experiments, this time may be greater or less than t. Before examining Eq. 8, some results of the experiment will be discussed.

The important quantities that are observed in the experiment are the beam collector current I_c, the pulsed light output from the plasma, the rf oscillation produced by the discharge, and the current pulses picked up by various movable probes in the vacuum chamber. These quantities were previously defined explicitly (3). Other information is obtained from visual observations of the plasma, photographs, and measurements of gas pressure in the interaction region.

A set of oscillographs showing the collector current and photomultiplier output voltage for four different settings of the pressure are shown in Fig. II-18. Values of the time delay t from the beginning of the pulse to the onset of oscillations (indicated by the sudden break in the collector current) were obtained from similar oscillographs. The dependence of t on pressure is shown in Fig. II-19. For each setting of beam voltage

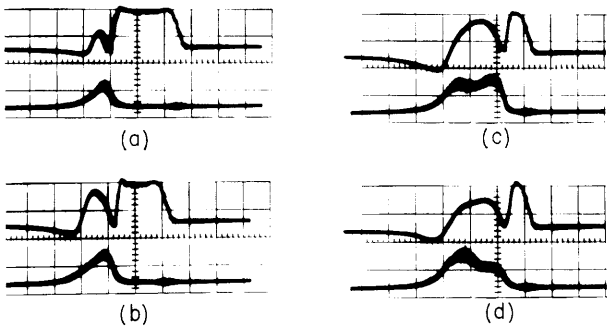

Fig. II-18. Collector current and light oscillograph traces showing variation of time delay with pressure. The pressure increases from (a) to (d). In the photographs, time runs from right to left.

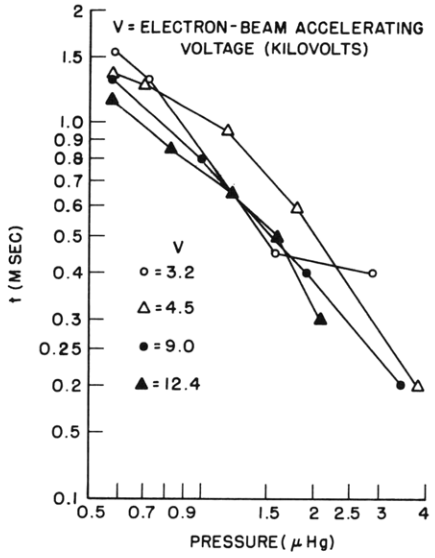

Fig. II-19. Variation of the time delay between the leading edge of the electron-beam pulse and the onset of oscillations with pressure.

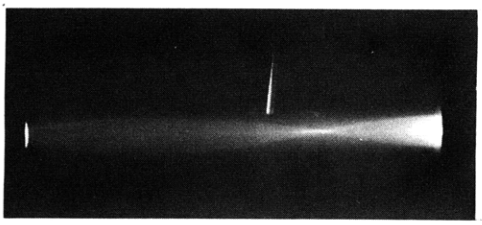

Fig. II-20. Five-second time exposure of plasma under conditions in which a sharp beam cross-over is obtained.

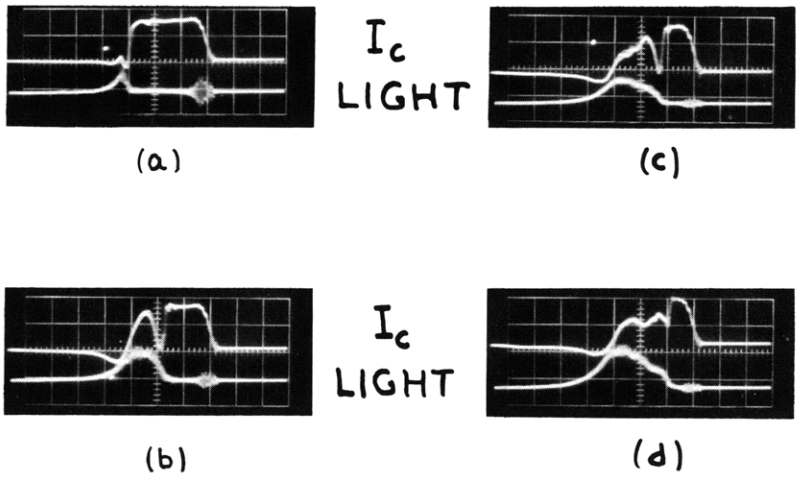

Fig. II-21. Collector current and light oscillograph traces showing variation of time delay with magnetic-field intensity. The magnetic field increases from (a) to (d). In the photographs, time runs from right to left.

and magnetic induction, the beam flows through the time-variant plasma for a length of time that is inversely proportional to the pressure. This is consistent with the hypothesis that the plasma density reaches a critical value before the oscillations begin. Equation 1 shows that the beam is neutralized many times over at the time of the onset of oscillations. The time delay plotted in Fig. II-19 was corrected for the finite rise time of the pulse.

In general, it was found that for a given beam voltage and current, a minimum distance from gun anode to collector existed below which no beam break-up could be obtained for any magnetic induction or pressure in the available ranges of these two variables.

The wide range of effects obtained by varying the magnetic induction have not been fully explored. Two Helmholtz coils, separately excited, supply a magnetic induction of magnitude 100 to 1000 gauss. The shape of the field can be varied by changing one or both coil currents and by inserting iron face plates and cylinders into the system. In general, the plasma resonance frequency ω_{pp} at the onset of oscillation can be greater or less than ω_c. Under certain conditions, the beam, which originates in a magnetic field-free region, is focused at sharp crossovers that are spaced $2\pi/\beta_c$ apart. Figure II-20 is a time exposure (300 beam pulses) taken of the plasma and beam at a field low enough to produce only one crossover in the interaction region. The collector, on the right, is a tantalum tube, 0.5 in. in diameter and 12 inches long. The beam is collected inside the tube; thereby the escape of secondary electrons into the plasma region is prevented. A series of oscillographs shown in Fig. II-21 indicate the variation of t with magnetic induction. As the magnetic induction is increased in approximately 10 per cent steps, the time delay decreases.

An oscillograph of the video output pulse of an APR/4 receiver is shown in Fig. II-22. The receiver, which has a bandwidth of 2 mc, is tuned to 2500 mc. The delay between

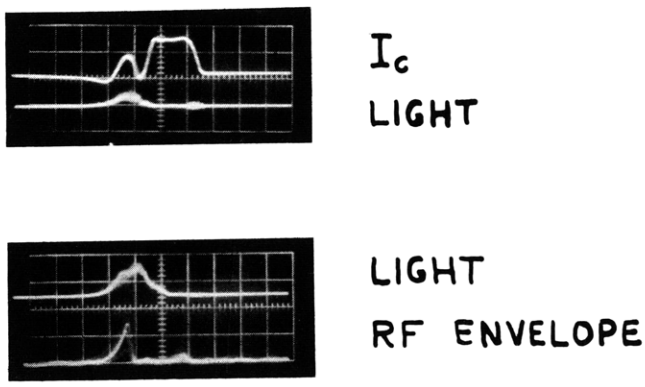

Fig. II-22. Typical oscillograph traces of I_c, light output, and rf envelope.

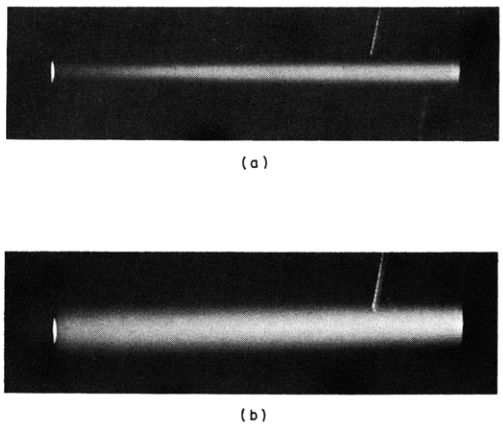

Fig. II-23. Five-second time exposures of the plasma showing two typical light distributions: (a) at higher magnetic fields, the light intensity increases toward the collector; (b) the light intensity is relatively uniform over the entire length of the plasma.

the collector current break-up and the rf burst is due to the receiver. The rf spectrum has not been explored completely. The microwave radiation spectrum is wideband, and includes both the plasma frequency ω_{pp} and the cyclotron frequency ω_c. The power available is sufficient to saturate the receiver. Further studies of the rf and visible spectra are planned.

These experimental observations have been interpreted in terms of the dispersion equation presented in Eq. 2, and particularly in terms of the integrated amplification constant G_o given by Eq. 8. When the electron gun is space-charge-limited, the ratio β_{pb}^2/β_T^2 depends only on the perveance and is independent of the beam diameter. Therefore, the scalloping of the beam edge because of the magnetic induction should not have a first-order effect on G_o, which depends only on β_{pb}^2/β_T^2. Equation 8 is still valid even though the dc characteristics of the beam and plasma vary as a function of z, the axial coordinate. The time delay before the onset of oscillations is interpreted as the time required to reach a critical value of G_o. Inspection of Eq. 8 shows that G_o starts at zero and increases as ω_{pp}^2 increases. The onset of oscillations marks the time required for G_o to reach a value great enough to produce large amplitude ac oscillations at the downstream end of the interaction region. If L is decreased, Eq. 8 indicates that a longer time delay is required. If this time becomes longer than the pulse length, no oscillations occur. The effect of varying ω_c can also be obtained from Eq. 8. For simplicity, assume that the oscillation commences at a time when $\omega_{pp}^2 \ll \omega_c^2$. Then G_o is approximately given by

$$G_o = \sqrt{\frac{\pi}{2}} \frac{e^{\beta_c L}}{(\beta_c L)^{1/2}} \frac{\beta_{pb}^2}{\beta_T^2} \frac{\omega_{pp}^2}{\omega_c} \tag{9}$$

The time delay is proportional to ω_{pp}^2, which is given by

$$\omega_{pp}^2 = \sqrt{\frac{2}{\pi}} G_o \frac{\beta_T^2}{\beta_{pb}^2} \frac{v_o}{L} (\beta_c L)^{3/2} e^{-\beta_c L} \tag{10}$$

The time delay is, therefore, proportional to $\exp(-\beta_c L)$. This variation is approximately true for the series of oscillograms from which those shown in Fig. II-21 were taken.

The photographs of the beam and plasma shown in Fig. II-23 are time exposures of several hundred pulses. These two distributions of light intensity, as well as that shown in Fig. II-20, were taken for three sets of operating conditions, all of which produce a large amplitude oscillation. Considering the fact that a thermal argon atom has a velocity of approximately 1 mm/μsec, we conclude that the light distribution is a direct indication of the density distribution of energetic electrons. The two light intensity distributions of Fig. II-23 were obtained with slightly different values of magnetic induction, and are typical of all photographs taken, with the exception of the type shown in Fig. II-20.

W. D. Getty

References

1. L. D. Smullin and W. D. Getty, Electron-beam stimulated plasma oscillation, Quarterly Progress Report No. 56, Research Laboratory of Electronics, M.I.T., Jan. 15, 1960, pp. 27-34.

2. E. V. Bogdanov, V. J. Kislov, and Z. S. Tchernov, Interaction between an electron stream and plasma, Microwave Research Institute Symposium Series, Vol. IX (Polytechnic Institute of Brooklyn, New York, 1959), pp. 57-72.

3. L. D. Smullin and W. D. Getty, Large-signal electron-stimulated plasma oscillations, Quarterly Progress Report No. 61, Research Laboratory of Electronics, M.I.T., April 15, 1961, pp. 33-36.

4. L. D. Smullin and P. Chorney, Propagation in ion-loaded waveguides, Microwave Research Institute Symposium Series, Vol. VIII (Polytechnic Institute of Brooklyn, New York, 1958), p. 242.

5. PLASMA HEATING BY ELECTRON BEAM-PLASMA INTERACTION

a. Dispersion Relation and Growth Constant

A study has been made of the small-signal energy transfer from an electron beam to a stationary plasma. A one-dimensional model is used for the analysis which may be described as follows. A cold, collisionless electron beam with a dc drift velocity passes through a stationary plasma with a temperature V_T and an electron-ion collision frequency ν_{ca}. Only the interaction between the beam electrons

and the plasma electrons is considered.

Boyd (1) shows that the following dispersion relation may be used to describe the situation described above.

$$1 = \left(\frac{\omega_{pa}}{\omega}\right)^2 \frac{1}{1 - j\frac{\nu_{ca}}{\omega}} \left\{ 1 + \frac{\Gamma^2}{R\ 1 - j\frac{\nu_{ca}}{\omega}} + \frac{5}{3}\frac{\Gamma^4}{R^2\left(1 - j\frac{\nu_{ca}}{\omega}\right)} + \ldots \right\} + \frac{\left(\frac{\omega_{pb}}{\omega}\right)^2}{(\Gamma-1)^2} \tag{1}$$

where

$$R = \frac{\frac{1}{2} m v_{ob}^2}{\frac{3}{2} KT} \quad \text{and} \quad \Gamma = \frac{\beta}{\beta_{eb}} \tag{2}$$

Equation 1 has been solved by using numerical methods (2) for the real and imaginary parts of Γ at $\omega = \omega_{pa}$ as a function of

$$\xi = \frac{\omega_{pb}}{\omega_{pa}}\left(\frac{V}{V_T}\right)^{1/2} \tag{3}$$

for parametric values of

$$\eta = \frac{\omega_{pb}}{\omega_{pa}}\left(\frac{\omega_{pa}}{\nu_{ca}}\right)^{1/2} \tag{4}$$

b. Power Transfer

(i) Plasma electrons at fixed temperature. The power per unit area dissipated in the plasma behind a plane of interest may be computed from the negative kinetic power carried across this plane by the beam:

$$P_{dis} = -\,\mathrm{Re}\left\{\frac{1}{2} U_b J_b^*\right\} = -\,\mathrm{Re}\left\{\frac{1}{2} Z_{ob} |J_b|^2\right\} \tag{5}$$

where

$$Z_{ob} = \frac{U_b}{J_b} = \frac{1 - \frac{\gamma}{j\beta_{eb}}}{\omega_{pb}\epsilon_o\beta_{pb}} = \frac{1 - u - j\nu}{\omega_{pb}\epsilon_o\beta_{pb}} \tag{6}$$

and we have introduced the normalized growth constant

$$\frac{\gamma}{j\beta_{eb}} = u + j\nu \tag{7}$$

Thus

$$P_{dis} = \frac{1}{2} \frac{u - 1}{\omega_{pb}\epsilon_o\beta_{pb}} |J_b|^2 \tag{8}$$

We are interested in knowing the power dissipated in the plasma behind the plane at which the magnitude of the ac beam current is some specified fraction of the dc beam current,

$$|J_b| = aJ_{ob} \tag{9}$$

Thus we write

$$\frac{P_{dis}}{P_o} = \frac{1}{2} a^2 \frac{J_{ob}}{V_{ob}} \frac{u - 1}{\omega_{pb}\epsilon_o\beta_{pb}} \tag{10}$$

Introducing the beam perveance and area, K and A, for ease of comparison with physical systems, we obtain

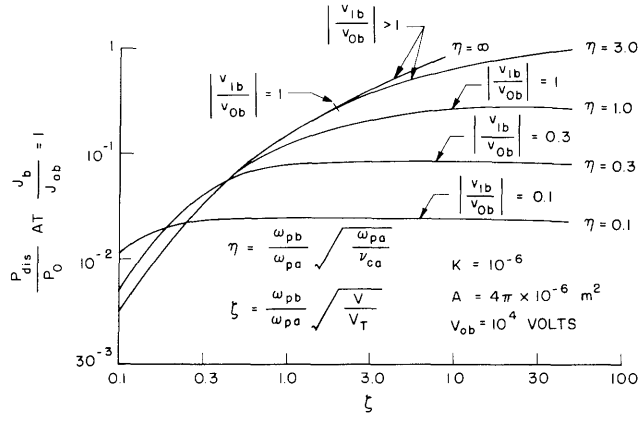

Fig. II-24. Ratio of power dissipated in plasma to dc beam power versus initial beam temperature, with collision frequency a parameter.

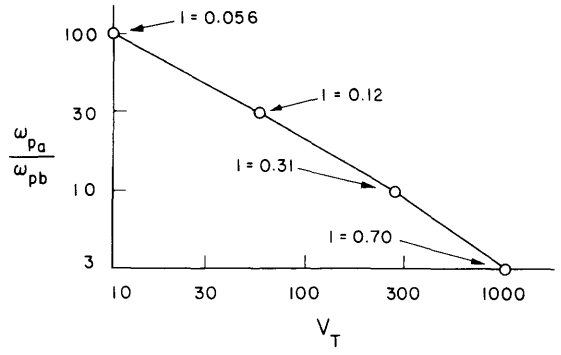

Fig. II-25. Equilibrium plasma temperature versus (ω_{pa}/ω_{pb}). (Plasma overtaking Index I noted along curve.)

$$\frac{P_{dis}}{P_o} = \frac{1}{2} a^2 \frac{KV_{ob}^{1/2}}{A} \frac{u - 1}{\omega_{pb}\epsilon_o\beta_{pb}} \tag{11}$$

Curves of P_{dis}/P_o as a function of plasma temperature for parametric values of collision frequency are shown in Fig. II-24. The beam and plasma parameters used in both Figs. II-24 and II-25 are those measured in the hollow-cathode discharge described by Getty and Smullin (3).

(ii) Beam electron velocity modulation. It is necessary to know the magnitude of the beam velocity modulation, as well as the current modulation, in order to keep a check on the validity of the small-signal assumptions used in our analysis. We start from Eq. 6 and proceed as follows:

$$U_b = J_b \frac{1 - u - j\nu}{\omega_{pb}\epsilon_o\beta_{pb}} \tag{12}$$

$$\frac{v_{1b}}{v_{ob}} = \frac{J_b}{J_{ob}} (1-u-j\nu) \tag{13}$$

Thus from the knowledge of the growth constant and the current modulation, the beam velocity modulation can be determined. The quantity $|v_{1b}/v_{ob}|$ is shown on the power dissipation curves as a reminder of the limits of the small-signal theory; this quantity must certainly be less than unity, and probably less than 1/2 if the small-signal assumptions are to be valid.

(iii) Amplitude of the plasma electron oscillations. Next, we consider the amplitude of the plasma electron oscillations. Since there is no dc drift velocity in the plasma,

$$J_a = \rho_{oa} v_a \tag{14}$$

if all components except the fundamental component of the plasma electron current are neglected.

The plasma and beam currents are related only by a complex constant, so we can write

$$v_a = \frac{J_{oa}}{\rho_{oa}} e^{\alpha z_o} \cos(\omega_{\rho a} t - \beta z_o + \theta) \tag{15}$$

and

$$z_a = z_o + \frac{J_{oa}}{\rho_{oa}\omega_{pa}} e^{\alpha z_o} \sin(\omega_{pa} t - \beta z_o + \theta) \tag{16}$$

where z_a is the position of a sheet of charge transverse to the z-axis which moves about its equilibrium position z_o. The condition for overtaking is

$$\frac{\partial z_a}{\partial z_o} = 0 \tag{17}$$

This defines the conditions under which two sheets with different equilibrium positions arrive at the same position simultaneously. Applying Eq. 17 to Eq. 16, we have

$$1 = a\left|m\right|\left(\frac{\omega_{pb}}{\omega_{pa}}\right)^2\left(\frac{\beta}{\beta_{eb}} + \frac{\alpha}{\beta}\,\frac{\alpha}{\beta_{eb}}\right)\cos\left(\omega_{pa}t-\beta z_o+\theta\right) \tag{18}$$

$$\tan\left(\omega_{pa}t-\beta z_o+\theta\right) = -\frac{\alpha}{\beta} \tag{19}$$

where

$$m = \frac{J_a}{J_b} = 1 + j\left(\frac{\omega_{pa}}{\omega_{pb}}\right)^2\left(\frac{\gamma}{j\beta_{eb}} - 1\right)^2 \tag{20}$$

The right-hand side of Eq. 18, with Eq. 19 satisfied, is a plasma overtaking index. When it is less than one, no overtaking occurs in the plasma under the assumption of Eq. 14.

(iv) Equilibrium temperature. The previous discussion has considered the power dissipated in the plasma with the plasma at a fixed temperature. If the plasma is allowed to warm up as a result of this interaction, the dissipation decreases and an equilibrium temperature is approached. An estimate of this equilibrium temperature may be made by finding the initial plasma temperature that will allow the plasma electron oscillations to reach an energy equivalent to this temperature as the beam leaves the small-signal region. A plot of the equilibrium temperature versus $(\omega_{pa}/\omega_{pb})$ is shown in Fig. II-25. Values of the plasma overtaking index are shown along the curve, indicating the size of the plasma electron oscillations.

D. L. Morse

References

1. G. D. Boyd, Experiments on the Interaction of a Modulated Electron Beam with a Plasma, Technical Report No. 11, California Institute of Technology, Pasadena, California, May 1959.

2. P. Chorney (private communication, 1961).

3. W. Getty and L. D. Smullin, Experimental results of the study of the hollow-cathode discharge, Quarterly Progress Report No. 58, Research Laboratory of Electronics, M.I.T., July 15, 1960, pp. 35-41.

6. INTERACTION OF IONS AND ELECTRONS

We have been studying the interaction between ions and electrons in a plasma. Our model is one-dimensional and it is constructed from cold ions, without thermal spread,

and of hot electrons with a velocity distribution given by a Maxwellian curve or a resonant type of curve (1). The latter has the form

$$f_e(v) = \frac{v_{e\theta}/\pi}{(v-v_e)^2 + v_{e\theta}^2} \tag{1}$$

where v_e is the mean velocity and $v_{e\theta}$ is the thermal spread. This distribution has been introduced in order to avoid error functions, which introduce heavy computational work into the problem.

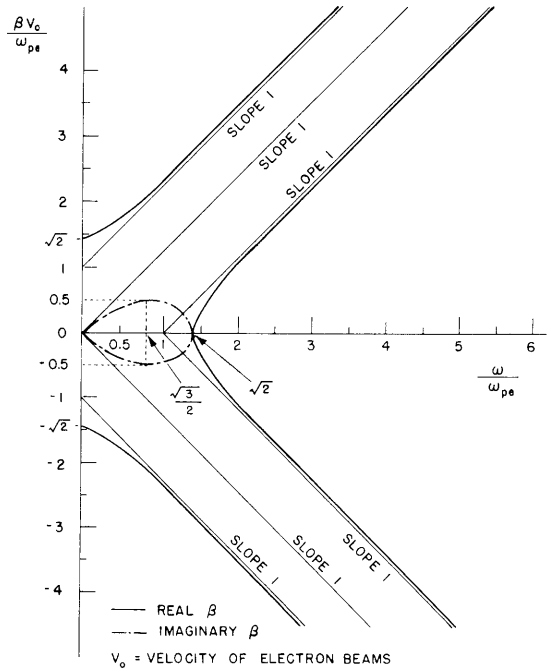

Fig. II-26. Wave number versus frequency for two electron beams with opposite velocities.

We may consider the electron distribution as an infinite number of beams with velocities symmetrically located with respect to $v_o = 0$. We consider, first, the interaction of two electron beams with opposite velocities, and then the same problem in the presence of cold ions. Our calculations yield the following results:

(a) For two electron beams with opposite velocities:

$$\beta = \pm \beta_e \left[1 + \frac{\omega_{pe}^2}{\omega^2} \left(1 \pm \left(1 + 4 \frac{\omega^2}{\omega_{pe}^2} \right)^{1/2} \right) \right]^{1/2} \tag{2}$$

For a plot of β versus ω, see Fig. II-26.

(b) For two electron beams with opposite velocities and cold ions:

$$\beta = \pm \beta_e \left\{ 1 + \frac{1}{b^2} \left[1 \pm (1+4b^2)^{1/2} \right] \right\}^{1/2} \tag{3}$$

where

$$b^2 = \frac{\omega^2 - \omega_{pi}^2}{\omega_{pe}^2} \tag{3a}$$

The plot of β versus ω is given in Fig. II-27.

(c) For electrons with distributed veolcities (resonant type of curve with $v_e = 0$) and cold ions:

$$0 < \omega < \omega_{pi}, \quad \beta = \pm \frac{\omega}{v_{e\theta}} \left[-1 - \frac{1}{2b^2} \pm \left\{ \frac{1}{b^2} \left(2 + \frac{1}{4b^2} \right) \right\}^{1/2} \right]^{1/2} \tag{4}$$

$$\omega_{pi} < \omega < \left(\omega_{pe}^2 + \omega_{pi}^2 \right)^{1/2} \begin{cases} \beta = \pm \dfrac{j\omega}{v_{e\theta}} \left(1 - \dfrac{\omega_{pe}}{\left(\omega^2 - \omega_{pi}^2 \right)^{1/2}} \right) & \text{(5a)} \\ \beta = \pm \dfrac{\omega}{v_{e\theta}} \left[-1 - \dfrac{1}{2b^2} + \left(\dfrac{1}{b^2} \left(2 + \dfrac{1}{4b^2} \right) \right)^{1/2} \right]^{1/2} & \text{(5b)} \end{cases}$$

Here, ω_{pe}^2 is defined as $n_e e^2/m\epsilon_o$, where n_e is the total electron density. For the plot of β versus ω see Fig. II-28.

(d) We are in the process of solving the problem of electrons with distributed velocities, cold ions and an electron beam.

In a study of the effects of pressure, we have generalized the dispersion equation so that it can include the effects of pressure, which are very strong even for small pressure, when the initial velocity is very small. If we treat the fully ionized gas as a perfect gas (2), we find the following relations between the kinetic voltage U_z and the current density J_z for the one-dimensional case:

$$\left(\frac{1}{v_o} \frac{\partial}{\partial t} + \frac{\partial}{\partial z} \right) J_z = \epsilon_o \frac{\omega_p^2}{v_o^2} \frac{\partial}{\partial t} U_z \tag{6a}$$

$$\left[\frac{1}{v_o} \frac{\partial}{\partial t} + \left(1 - \frac{a^2}{v_o^2} \right) \frac{\partial}{\partial z} \right] U_z = -\frac{1}{\epsilon_o} \left(\frac{1}{\partial} + \frac{a^2}{\omega_p^2} \frac{1}{v_o} \frac{\partial}{\partial z} \right) J_z \tag{6b}$$

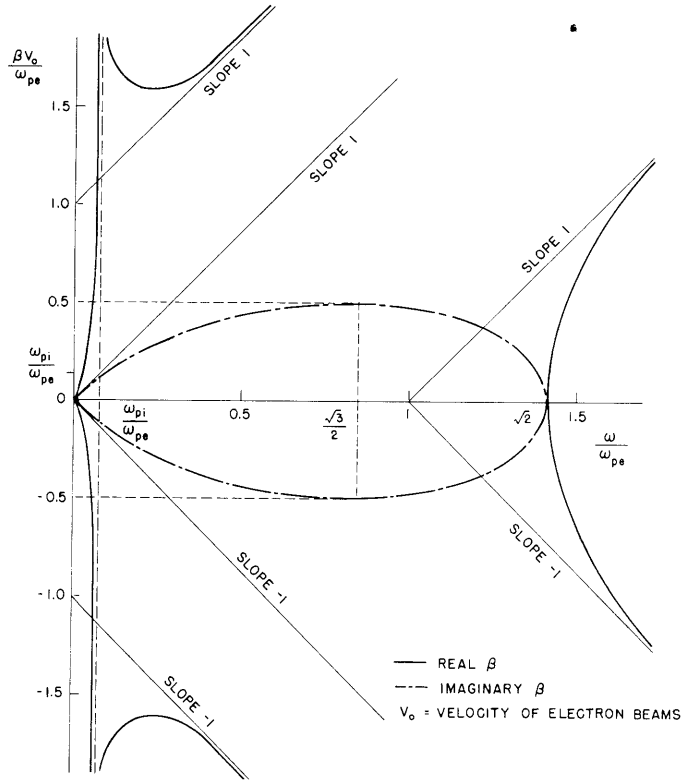

Fig. II-27. Wave number versus frequency for two electron beams with opposite velocities in the presence of cold ions.

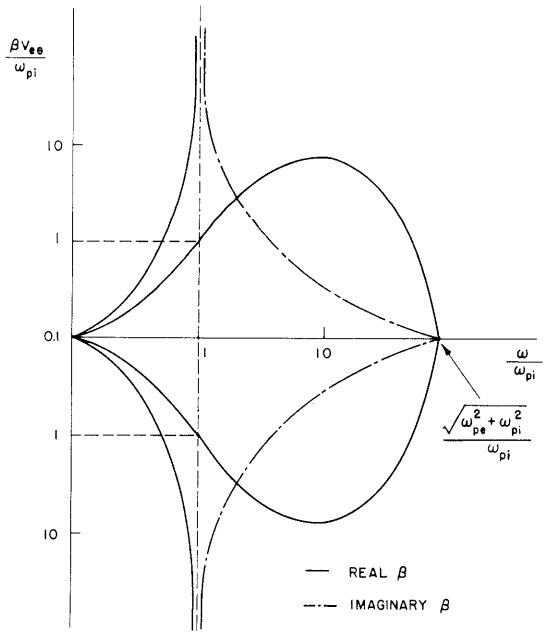

Fig. II-28. Wave number versus frequency for cold ions and electrons with thermal spread.

where a = sound velocity = $(\gamma P/mn)^{1/2}$. These equations form a generalization of the well-known equations in the absence of pressure (3). For more than one beam, we have

$$\frac{1}{v_{oi}}\frac{\partial}{\partial t}+\frac{\partial}{\partial z}\;J_i=\epsilon_o\frac{\omega_{pi}^2}{v_{oi}^2}\frac{\partial}{\partial t}U_i \tag{7a}$$

$$\left[\frac{1}{v_{oi}}\frac{\partial}{\partial t}+\left(1-\frac{a_i^2}{v_{oi}^2}\right)\frac{\partial}{\partial z}\right]U_i=-\frac{1}{\epsilon_o}\left(\frac{J_{total}}{\partial t}+\frac{a_i^2}{\omega_{pi}^2}\frac{1}{v_{oi}}\frac{\partial}{\partial z}J_i\right) \tag{7b}$$

Eliminating U_i and using the variation $\exp[j(\omega t-\beta z)]$, we find that (since $J_{total}=\sum_i J_i$) the dispersion relation is

$$\sum_i\frac{\beta_{pi}^2}{(\beta_{ei}-\beta)^2-\frac{\beta^2}{M_i^2}}=1 \tag{8a}$$

or

$$\sum_i\frac{\omega_{pi}^2}{(\omega-v_{oi}\beta)^2-a_i^2\beta^2}=1 \tag{8b}$$

where $M_i=(v_{oi}/a_i)$ is the Mach number. The known dispersion equation is a special case with $M=\infty$ ($a=0$, that is, $p=0$). For $M=0$ (that is, $v_o=0$) we find the results obtained by Pai (4), which cannot be obtained from the old dispersion equation. Then we made a study of the way in which the new formula modifies the known results in some special cases (5).

For the interaction of electron and cold ions, we find

$$\frac{\omega_{pi}^2}{\omega^2}+\frac{\omega_{pe}^2}{}\int_{-\infty}^{\infty}\frac{f_e(v)\,dv}{(\omega-v\beta)^2-a_e^2\beta^2}=1 \tag{9a}$$

or

$$\frac{\omega_{pi}^2}{\omega^2}+\frac{\omega_{pe}^2}{2a_e\beta^2}\int_{-\infty}^{\infty}f_e'(v)\ln\frac{v-\frac{\omega}{\beta}+a_e}{v-\frac{\omega}{\beta}-a_e}\,dv=1 \tag{9b}$$

If the Landau damping term is neglected, the dispersion equation reduces to

$$\frac{\omega_{pi}^2}{\omega^2} + \frac{\omega_{pe}^2}{\omega^2 - 3\beta^2 v_p^2} + \frac{\omega_{pe}^2 \beta^2 a_e^2}{(\omega^2 - 10\beta^2 v_p^2)\,\omega^2} = 1$$

with the solution

$$\beta^2 = \frac{\omega^2}{6v_p^2}\left\{\frac{(13b^2-10) + L^2 \pm [(7b^2-10)^2 + L^2(L^2+14b^2-8)]^{1/2}}{10b^2 + L^2}\right\} \tag{10}$$

where

$$L^2 = \frac{a_e^2}{v_p^2},\quad b^2 = \frac{\omega^2 - \omega_{pi}^2}{\omega_{pe}^2},\quad v_p^2 = \frac{kT}{m}$$

The Landau damping term is

$$\frac{\pi j}{2\beta^2}\left[f_e'\left(\frac{\omega}{\beta}+a_e\right) + f_e'\left(\frac{\omega}{\beta}-a_e\right)\right]$$

Solutions have been obtained in the general case which includes the Landau damping term (5).

The pressure also modifies the dielectric tensor. We can prove that

$$\nabla_{pi} = \frac{p_{oi}}{n_{oi}}\frac{\epsilon_o}{e}(\bar{\beta};\bar{\beta})\bar{E}_i$$

where $(\bar{\beta};\bar{\beta})$ denotes a dyadic.

Then, including ∇_{pi} in the motion equation, we finally find for the dielectric tensor $\overleftrightarrow{\epsilon} = \overleftrightarrow{\epsilon} + \overleftrightarrow{\epsilon}_p$, where $\overleftrightarrow{\epsilon}$ is the usual dielectric tensor (3), and $\overleftrightarrow{\epsilon}_p$ is given by

$$\overleftrightarrow{\epsilon}_p = \epsilon_o \frac{a^2}{\omega^2}\begin{bmatrix} \dfrac{-\beta_r^2 + j\beta_r\beta_\theta(\omega_c/\omega)}{1-(\omega_c^2/\omega^2)} & \dfrac{-\beta_r\beta_\theta + j\beta_\theta^2(\omega_c/\omega)}{1-(\omega_c^2/\omega^2)} & \dfrac{-\beta_r\beta_z + j\beta_\theta\beta_z(\omega_c/\omega)}{1-(\omega_c^2/\omega^2)} \\ \dfrac{-\beta_\theta\beta_r - j\beta_r^2(\omega_c/\omega)}{1-(\omega_c^2/\omega^2)} & \dfrac{-\beta_\theta^2 - j\beta_r\beta_\theta(\omega_c/\omega)}{1-(\omega_c^2/\omega^2)} & \dfrac{-\beta_\theta\beta_z - j\beta_r\beta_z(\omega_c/\omega)}{1-(\omega_c^2/\omega^2)} \\ -\beta_r\beta_z & -\beta_z\beta_\theta & -\beta_z^2 \end{bmatrix}$$

We have ignored collisions throughout this report.

P. E. Serafim

References

1. Quarterly Status Report No. 15, Stanford Electronics Laboratories, Stanford University, California, September 1960, p. 2.

2. L. Spitzer, Physics of Fully Ionized Gases (Interscience Publishers, Inc., New York, 1956).

3. L. D. Smullin, Electron Stimulated Ion Oscillations, Plasma Dynamics Summer Course, M. I. T., 1959 (unpublished).

4. S. I. Pai, Wave motions of small amplitude in a fully ionized plasma without external magnetic field, Revs. Modern Phys. 32, 882 (1960).

5. P. E. Serafim, Wave motion of small amplitude including pressure, Term Paper Course 6.526, M. I. T., 1961 (unpublished).

7. SCATTERING OF WAVES BY A TENUOUS PLASMA OF FINITE GEOMETRY

The study of the scattering of an incident uniform plane wave by a tenuous plasma rod in the absence of magnetic field (1) has continued. In particular, the near and far fields of the transmitted wave, which is the sum of the incident and scattered wave, are examined for different density profiles. The results are summarized below. The following notation is used:

E_{tI}, is the transmitted E-field in the far-field region I.

E_{tII}, is the transmitted E-field in the near-field region II.

This notation is explained in the following diagram.

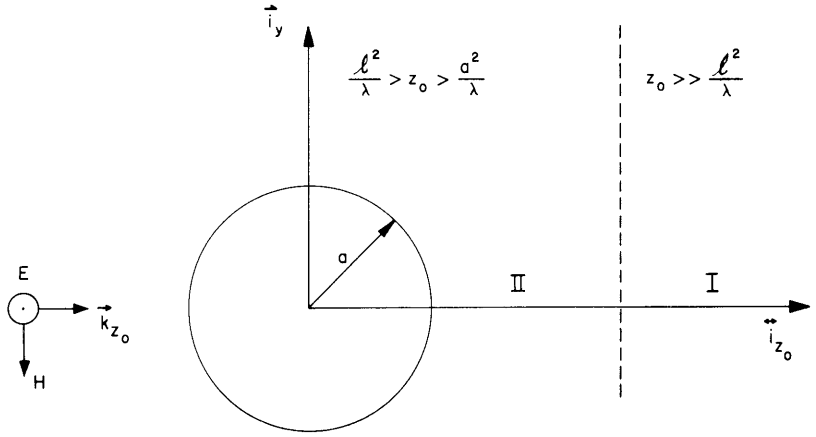

The incident field has the electric vector polarized parallel to the rod; z_o is the point of observation; 2ℓ is the length of the plasma rod; a is the radius of the plasma rod; and k is $2\pi/\lambda$, with λ the free-space wavelength.

For uniform density inside the rod and zero density outside the rod:

$$N = \begin{cases} N_o, & 0 \leq r \leq a \\ 0, & a < r \end{cases}$$

$$E_{tI_a} = E_o \exp(j\omega t - jka - jkz_o) \left\{ 1 - \left(\frac{\omega_p}{\omega}\right)^2 \frac{2\ell}{z_o} \left(\frac{ka}{2}\right)^2 + j \left(\frac{\omega_p}{\omega}\right)^2 \frac{k\ell}{z_o^2} \left(\frac{ka}{2}\right)^2 \left(\frac{\ell^2}{3} + \frac{a^2}{4}\right) \right\} \tag{1}$$

$$E_{tII_a} \doteq E_o \exp(j\omega t - jka - jkz_o) \left\{ 1 - \left(\frac{\omega_p}{\omega}\right)^2 \left(\frac{ka}{2}\right)^2 \left(\frac{\pi}{kz_o}\right)^{1/2} \left(1 - \frac{ka^2}{8z_o}\right) \right.$$

$$\left. + j \left(\frac{\omega_p}{\omega}\right)^2 \left(\frac{ka}{2}\right)^2 \left(\frac{\pi}{kz_o}\right)^{1/2} \left(1 + \frac{ka^2}{8z_o}\right) \right\} \tag{2}$$

For

$$N = \begin{cases} N_o(1-0.9(r/a)^2) & 0 \leq r \leq a \\ 0 & a < r \end{cases}$$

$$E_{tI_b} \approx E_o \exp(j\omega t - jka - jkz_o) \left[1 - \left(\frac{\omega_p}{\omega}\right)^2 \left(\frac{ka}{2}\right)^2 \frac{2\ell}{z_o} (.55) + j \left(\frac{\omega_p}{\omega}\right)^2 \left(\frac{ka}{2}\right)^2 \frac{k\ell}{z_0^2} (.55) \left(\frac{\ell^2}{6} + \frac{a^2}{11}\right) \right] \tag{3}$$

$$E_{tII_b} \approx E_o \exp(j\omega t - jka - jkz_o) \left[1 - \left(\frac{\omega_p}{\omega}\right)^2 \left(\frac{ka}{2}\right)^2 (.55) \left(\frac{\pi}{kz_o}\right)^{1/2} \left(1 - \frac{ka^2}{11z_o}\right) \right.$$

$$\left. + j \left(\frac{\omega_p}{\omega}\right)^2 \left(\frac{ka}{2}\right)^2 (.55) \left(\frac{\pi}{kz_o}\right)^{1/2} \left(1 + \frac{ka^2}{11z_o}\right) \right] \tag{4}$$

For

$$N = \begin{cases} N_o\left(1-2(r/a)^2 \exp\left[-0.8(r/a)^2\right]\right) & 0 \leq r \leq a \\ 0 & a < r \end{cases}$$

$$E_{tI_c} \approx E_o \exp(j\omega t - jka - jkz_o) \left[1 - \left(\frac{\omega_p}{\omega}\right)^2 \left(\frac{ka}{2}\right)^2 \frac{2\ell}{z_o} (.4) + j \left(\frac{\omega_p}{\omega}\right)^2 \left(\frac{ka}{2}\right)^2 \frac{k\ell}{z_o^2} (.4) \left(\frac{\ell^2}{3} + .08a^2\right) \right] \tag{5}$$

$$E_{tII_c} \approx E_o \exp(j\omega t - jka - jkz_o)\left[1 - \left(\frac{\omega_p}{\omega}\right)^2\left(\frac{ka}{2}\right)^2\left(\frac{\pi}{kz_o}\right)^{1/2}(.4)\left(1 - \cdot\frac{08ka^2}{z_o}\right)\right.$$

$$\left. + j\left(\frac{\omega_p}{\omega}\right)^2\left(\frac{ka}{2}\right)^2\left(\frac{\pi}{kz_o}\right)^{1/2}(.4)\left(1 + \cdot\frac{08ka^2}{z_o}\right)\right] \qquad (6)$$

See Fig. II-29 for density profiles as a function of r.

Equations 1-6 are valid for $(\omega_p/\omega)^2 \ll 1$, and for either $z_{oI} \gg \ell^2/\lambda > a^2/\lambda$ or $\ell^2/\lambda > z_{oII} \gg a^2/\lambda$. These equations tell us that the plasma rod makes only minute changes in the field at z_o, as compared with the case $\omega_p = 0$, and the effect of density profiles is to add finer details to that perturbation.

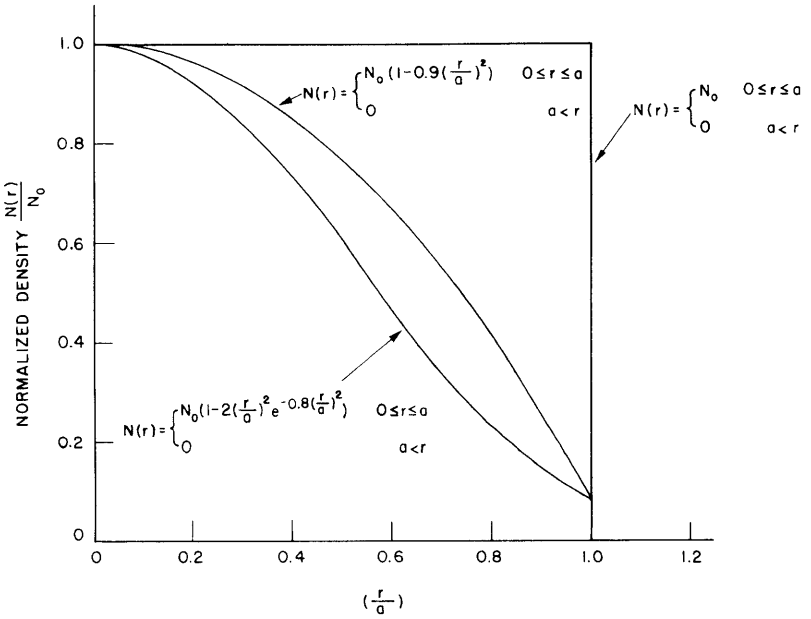

Fig. II-29. Density profiles as a function of r/a.

Some of the results of these calculations have been compared with the results of the boundary-value problem (1). The computer program for the boundary-value problem was prepared by Christa-Maria de Ridder and her colleagues at Lincoln Laboratory, M. I. T. These comparisons are shown in Fig. II-30.

An alternative problem that can help us to understand microwave measurements of the plasma column enclosed by vacuum system walls is to consider the problem of a dielectric rod in a waveguide. In particular, consider the system shown in Fig. II-31.

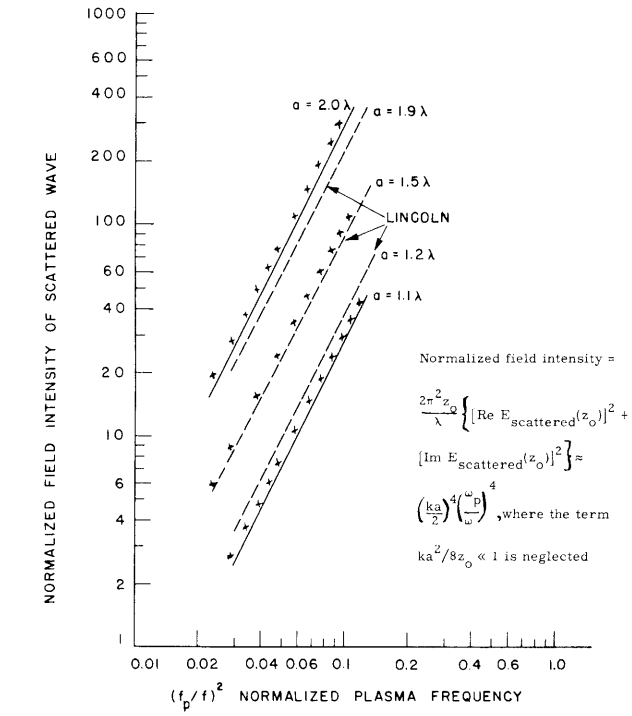

Fig. II-30. (a) Plot of normalized field intensity of scattered wave versus normalized plasma frequency. (x's on lines a = 2.0 λ, a = 1.5 λ, and a = 1.1 λ represent computed values from the expression for normalized field intensity.)
(b) Plot of phase of the scattered field of z_o, $\tan^{-1}$ (Im E_{sc}/Re E_{sc}) versus $(f_p/f)^2$.

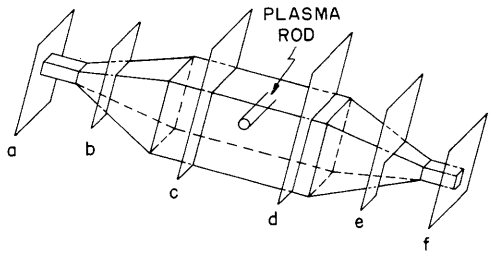

Fig. II-31. Waveguide configuration.

Here, the plasma appears as a dielectric post in the large rectangular waveguide which is joined at both ends by sectoral waveguides leading to smaller rectangular waveguides of such a cross section that at the probing frequency, ω, only the TE_{10} mode is propagating at planes a and f.

The problem of energy propagation from planes a to c, and hence from d to f, is well understood (2). The propagation from planes c to d can be treated by the method of images (3). Work has begun on the theoretical analysis of propagation from plane a to plane f, to provide the design data for the sectoral and large rectangular waveguides for microwave transmission measurements.

H. Y. Hsieh

References

1. H. Y. Hsieh, Scattering of waves by a tenuous plasma of finite geometry, Quarterly Progress Report No. 61, Research Laboratory of Electronics, M.I.T., April 15, 1961, pp. 43-47.

2. W. L. Barrow and L. J. Chu, Proc. IRE 27, 51-64 (1939).

3. J. C. Slater, Microwave Transmission (McGraw-Hill Book Company, Inc., New York, 1942), Chapter VII.

8. PENNING IONIZATION GAUGE (PIG) DISCHARGE

In the past quarter the study of Penning Ionization Gauge (PIG) discharges has been directed toward a study of hot-cathode devices. The terminal characteristics of a hot-cathode PIG discharge in mercury vapor at room temperature were measured.

The discharge tube (1) that was used is shown schematically in Fig. II-32a. Each cathode consists of a disk of a nickel cermet material held in a molybdenum cup. The anodes are rings of larger diameter than the cathodes. A mirror magnetic field with a mirror ratio of approximately 1.8 was used. The electrical network is shown schematically in Fig. II-32b.

Figure II-33 shows the V-I characteristics for the device. Figure II-33a shows the dc characteristics recorded on an automatic x-y plotter for various magnetic fields.

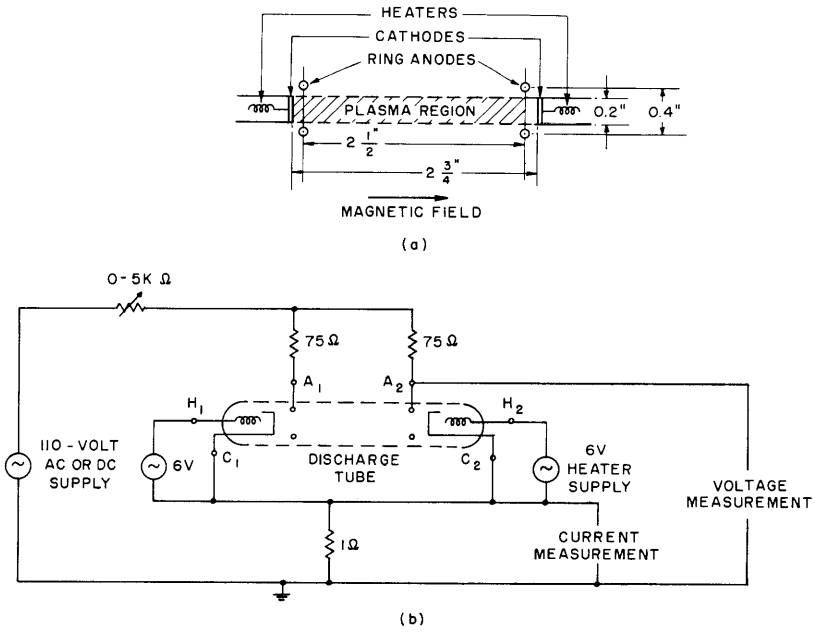

Fig. II-32. (a) Drawing of the PIG discharge device. (b) Schematic diagram of electrical network for operating the device.

Figure II-33b displays the dynamic characteristics of the discharge when a 60-cycle voltage source is used. It will be observed that the noise associated with the voltage is much greater for larger magnetic fields.

In Fig. II-33a we observe two distinct regions. For currents less than 520 ma the

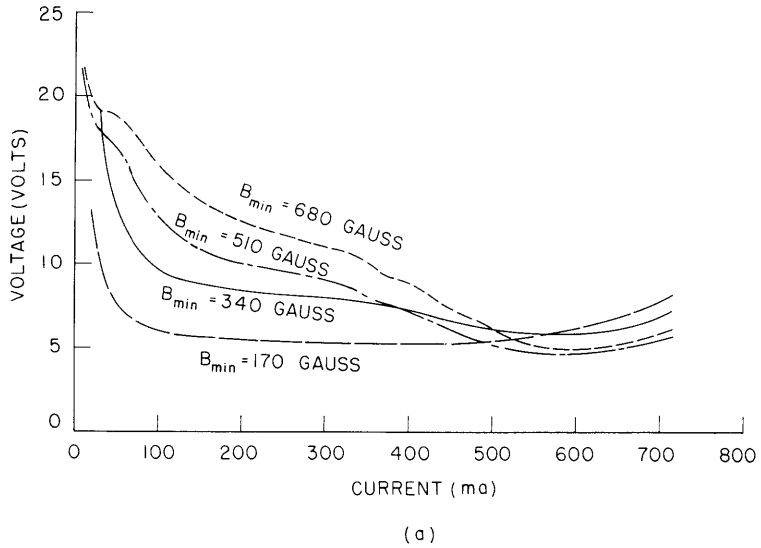

(See next page for figure legend.)

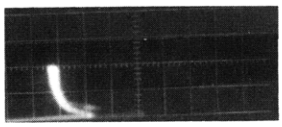

$B_{min.}$ = 170 gauss

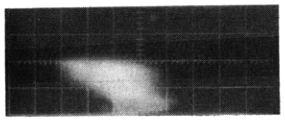

$B_{min.}$ = 680 gauss

(b)

Fig. II-33. (a) DC volt-ampere characteristics for various magnetic fields. (b) Oscillograms of ac volt-ampere characteristics at 60-cycle frequency. Abscissa and ordinate represent voltage and current, with scales of 5 volts/square and 100 ma/square, respectively.

voltage increases as the magnetic field increases, and for currents greater than 520 ma the voltage decreases as the magnetic field is increased. We have observed that the magnitude of the current at the crossover point is a function of cathode temperature, with higher cathode temperatures corresponding to larger crossover currents. This has been interpreted as the crossover from space-charge-limited to temperature-limited operation of the cathodes. In the temperature-limited region, all curves are for positive resistance. If we examine the power required to sustain the discharge at a given current, rent, we see that this power decreases as the magnetic field is increased. This appears quite logical because the larger magnetic field presumably inhibits the diffusion of charged particles to the anodes and thereby reduces the loss rate. An interpretation of the behavior in the space-charge-limited region has not yet been completed.

W. Larrabee IV

References

1. The discharge tube was furnished by Microwave Associates; it was developed there under U.S. Navy Bureau of Ships Contract NObsr-81206.

9. ANALYSIS OF A FULLY IONIZED PLASMA COLUMN

a. Basic Equations

A simple analysis exists for the one-dimensional problem of a fully ionized plasma flowing along parallel lines of induction, provided that:

(i) Space charge can be neglected in treating the parallel motions; and

(ii) The velocity distribution of each species of particle can be well-characterized

by a drift speed plus a Maxwellian distribution in the drifting system. The first assumption is valid in any reasonable plasma column; it fails in the sheaths at the ends of the column, but we shall not be concerned with the sheaths. The second assumption is often reasonable, in view of the fact that electron-electron and ion-ion velocity relaxations proceed much more rapidly than inter-species relaxations. This second assumption brings with it the further one that heat transfer can be neglected in calculating the local density and temperature. The reason is that heat flux requires an asymmetric velocity distribution in the drifting system.

Under these circumstances, a momentum equation and an energy equation can be written for each species (1). For the electrons, the momentum equation is

$$\frac{d}{dx}\left(nm_e\overleftarrow{v_{xe}^2} + nkT_e\right) - nq_eE = \int \underset{\sim}{dv} m_e v_{xe}\left(\frac{\partial f_e}{\partial t}\right)_{\text{coll ei}} = -nq_e\eta j \tag{1}$$

$$\frac{d}{dx}\left(nm_i\overline{v_{xi}^2} + nkT_i\right) - nq_iE = \int \underset{\sim}{dv} m_i v_{xi}\left(\frac{\partial f_i}{\partial t}\right)_{\text{coll ie}} = nq_e\eta j \tag{2}$$

Here, n(x) is the density of either species, $\bar{v}_x(x)$ is the mean axial drift velocity, kT(x) is thermal energy in the drifting system, q is charge, and E(x) is the axial electric field. The integrals represent momentum transferred to each species by the other by means of collisions; their sum is zero. The notation $\int \underset{\sim}{dv}$ represents integration over velocity space. If all drift speeds are small compared with the random electron speed, η is the conventionally calculated resistivity. In other cases, in which $T_e \to 0$, $v_x \to 0$ (we shall not discuss these cases in detail), the term η could be written as a function of n, and the drift speeds as a function of T_e.

The energy equation for each follows from the general time-independent relation

$$\underset{\sim}{\nabla} \cdot \left(n_i m_i \overline{v_i v_i^2}\right) = \underset{\sim}{j}_i \cdot \underset{\sim}{E} + \int \underset{\sim}{dv} \frac{m_i v_i^2}{2}\left(\frac{\partial f_i}{\partial t}\right)_{\text{coll ie}} = \underset{\sim}{j}_i \cdot \underset{\sim}{E} + \mathcal{S} \tag{3}$$

and similarly for the electrons. Here, $\underset{\sim}{v}$ is vector velocity, $\underset{\sim}{j}$ the current (amps) of the species. The symbol $\mathcal{S}$ is short notation for the energy interchange integral. By use of the standard reductions given by Rose and Clark (1), Eq. 3 reduces to

$$\frac{d}{dx}\left(\frac{n}{2} m_i \overline{v_{xi}^3} + \frac{5}{2} n\bar{v}_{xi} kT_i\right) = q_i n\bar{v}_{xi} E + \mathcal{S} \tag{4}$$

and similarly for electrons, by changing subscripts, and for the sign of $\mathcal{S}$ (the integrals must be equal and opposite). The quantity $\mathcal{S}$ is positive if ions gain energy from electrons. It is a function only of n, T_e, and T_i if the drift velocities are small, but it is also a function of the $\bar{v}_x$, generally.

The particle currents

$$\Gamma_e = n\bar{v}_{xe} \tag{5}$$

$$\Gamma_i = n\bar{v}_{xi} \tag{6}$$

are independent of distance x, and are used to eliminate the $\bar{v}_x$. We have, then, four first-order nonlinear equations (Eqs. 1, 2, and 4 for each species) in the four variables n, T_e, T_i and E.

b. Solution

The equations to be solved contain E algebraically; therefore the set can be reduced immediately to three equations. Next, the sum of Eqs. 1 and 2 yields

$$\frac{m_e\Gamma_e^2}{n} + nkT_e + \frac{m_i\Gamma_i^2}{n} + nkT_i = P = \text{constant} \tag{7}$$

where P is an integration constant. Thus there are, in fact, only two differential equations to be solved. These equations do not contain the distance x explicitly. Since $(dT/dx)/(dn/dx) \equiv dT/dn$ and $dn/dx \equiv 1/(dx/dn)$, we can write, after some algebraic manipulations,

$$\frac{d(kT_e)}{dn} = \frac{2kT_e}{3n} - \frac{5P\Gamma_i}{3(\Gamma_i-\Gamma_e)\,n^2}\left[1 - \frac{8\left(m_e\Gamma_e^2+m_i\Gamma_i^2\right)}{5Pn}\right]\left[1 + \frac{\Gamma_e(\Gamma_i-\Gamma_e)\,e^2\eta}{\mathcal{S}}\right] \tag{8}$$

$$\frac{dx}{dn} = \frac{5P\Gamma_e\Gamma_i}{2(\Gamma_i-\Gamma_e)\,n^2\mathcal{S}}\left[1 - \frac{8\left(m_e\Gamma_e^2+m_i\Gamma_i^2\right)}{5Pn}\right] \tag{9}$$

where $e = +1.6 \times 10^{-19}$ coulomb.

Although, generally, η and $\mathcal{S}$ may be functions of n, T_e, T_i and the fixed Γ, the T_i dependence can be removed by Eq. 7. Equation 8 is a first-order nonlinear equation between T_e and n. Given its solution, Eq. 9 is an integration, whereupon all is solved. An equation similar to Eq. 9 could be written for T_i, but no reason appears for displaying it. If the density is very high, so that the gas is essentially in thermal equilibrium, Eq. 8 reduces to $dT/dn = 2T/3n$, or $n/T^{3/2} = \text{constant}$. This is the adiabatic law for a perfect gas.

The ratio $|\Gamma_e(\Gamma_i-\Gamma_e)n^2\eta/\mathcal{S}|$ is critical for the analysis. The approximations (2)

$$\eta = 0.86\left(\frac{m_e}{2\pi}\right)^{1/2}\frac{e^2\ln\Lambda}{32\epsilon_o^2(kT_e)^{3/2}} \tag{10}$$

$$\mathcal{S} = \frac{e^4 n^2 m_e \left(1 - \frac{T_i}{T_e}\right) \ln \Lambda}{2\pi\epsilon_o^2 (2\pi m_e k T_e)^{1/2} m_i} \tag{11}$$

apply if the random electron velocity greatly exceeds all other velocities. The ratio in question is, then,

$$\frac{\Gamma_e(\Gamma_i - \Gamma_e)\, e^2}{\mathcal{S}} = \frac{0.169 m_i \Gamma_e (\Gamma_i - \Gamma_e)}{(nkT_e)n}$$

The parameter P is of the same order of magnitude as nkT_e. If Γ_e and Γ_i are not incommensurate, we see that the two correction terms in the brackets of Eq. 8 are comparable. These terms are in order of magnitude (ion drift energy)/(electron thermal energy). If Eq. 12 is large compared with unity, Eq. 8 is linear in T_e^2. In many cases of interest, however, Eq. 12 represents a small term, so that

$$kT_e = \frac{\Gamma_i P}{(\Gamma_i - \Gamma_e)n}\left[1 - \frac{m_e\Gamma_e^2 + m_i\Gamma_i^2}{Pn}\right] + Cn^{2/3} \tag{13}$$

where C is a constant of integration. Equations 7 and 13 give the simple form

$$\Gamma_e kT_e + \Gamma_i kT_i + (\Gamma_i - \Gamma_e)\, Cn^{2/3} = 0 \tag{14}$$

The correction term in brackets in Eq. 13 is small.

We must now solve Eq. 9 for x. Substitution of Eqs. 13 and 7 (or 14) for T_e and T_i in $\mathcal{S}$ leads to a difficult integral. It is easy to show for (drift energy/random energy) $\ll 1$ that $|dn/dx| \gg |dT_e/dx|$. One useful approximation then consists in setting

$$1 - \frac{T_i}{T_e} = 2 - \frac{P}{nkT_e}\left[1 - \frac{m_e\Gamma_e^2 + m_i\Gamma_i^2}{nP}\right] \approx 2 - \frac{P}{nkT_e} \tag{15}$$

and setting $T_e = T_{eo}$, a mean temperature, wherever it appears in $\mathcal{S}$, Eq. 9. Such approximations slightly distort the x-scale of the result, but not the relative changes of n, T_e, or T_i. Thus we find

$$x = D\left\{\frac{P^2}{2(nkT_{eo})^2} + \frac{2P}{nkT_{eo}} + 4\ln\left[2 - \frac{P}{nkT_{eo}}\right] + G\right\} \tag{16}$$

where

$$D = \frac{5\pi\epsilon_o^2 (2\pi m_e kT_{eo})^{1/2} m_i \Gamma_e \Gamma_i (kT_{eo})^3}{P^2(\Gamma_i - \Gamma_e)e^4 m_e \ln \Lambda} < 0 \tag{17}$$

because Γ_e is an inherently negative quantity (electrons flow in the -x direction). The constant G determines where x = 0.

Other simple approximations can be found, but the one stated appears most useful.

c. Numerical Example

We cite one example, corresponding roughly to the magnetically collimated anode-fed gas arc of Makin and co-workers at Oak Ridge National Laboratory (3). Conditions chosen near the anode end are: n_e (= n_i) = $10^{20}/m^3$; kT_e/e = 70 ev; kT_i/e = 2 ev; $\Gamma_i = 0.5 \times 10^{24}/m^2$-sec; $\Gamma_e = -3.0 \times 10^{24}/m^2$-sec (corresponding to 56 amp/cm^2, input H_2 rate of 2 cc (STP)/sec at the anode, fully ionized, arc cross-section area, 2.1 cm^2). The ion drift energy is approximately 1 ev, and the electron drift energy is much less.

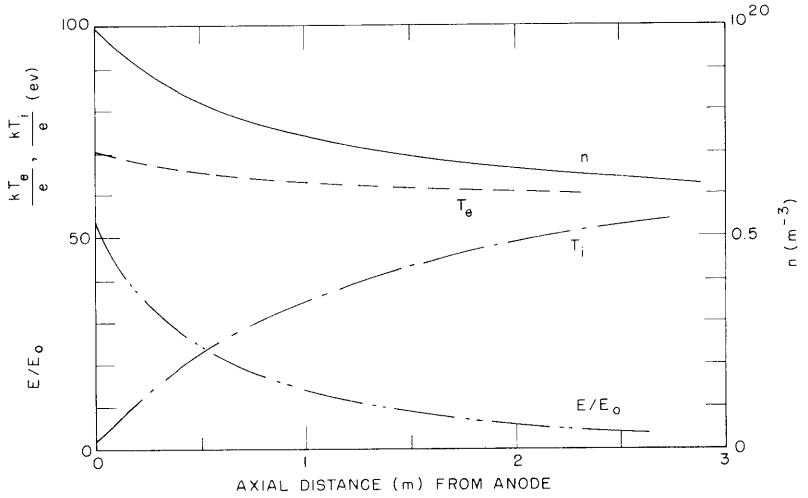

Fig. II-34. Density n, electron temperature kT_e/e, and ion temperature kT_i/e as functions of axial distance calculated for an arc column. Also shown is the ratio E/E_o, where E_o is the field calculated from the current density and conventional fully ionized plasma resistivity.

Figure II-34 shows the density, and electron and ion energies as functions of position. In addition, the electric field has been calculated. More instructive than the field itself is the ratio E/E_o, where E_o is the conventionally calculated value from the current density and resistivity η of a fully ionized gas. The quantity E/E_o is plotted in Fig. II-34. Note that the apparently small gradients of density and temperature have a drastic effect on the field, with $E/E_o \approx 50$ near the anode. The actual field E predicted near the anode is approximately 30 volts/m. We conclude that conventional

momentum-transfer resistivity is quite inadequate to describe the field in the arc, and that the various gas-kinetic derivatives described in Eqs. 1-5 dominate.

D. J. Rose

References

1. D. J. Rose and M. Clark, Jr., Plasmas and Controlled Fusion (The M. I. T. Press, Cambridge, Mass., and John Wiley and Sons, New York, 1961), pp. 119-122, 124.

2. Ibid., pp. 169, 173.

3. Report ORNL-3011, ORNL Thermonuclear Division Semi-Annual Report for period ending 31 July 1960, pp. 50-52; Report ORNL-3104, ORNL Thermonuclear Division Semi-Annual Report for period ending 31 January 1961, pp. 58-70.

10. ANOMALOUS DIFFUSION ACROSS THE MAGNETIC FIELD

In Quarterly Progress Report No. 61 (pages 64-66) the results of the radial voltage versus radial current experiments in the hollow-cathode discharge were reported. In the small current, the current I_r and the voltage V_r are sufficiently linear. Therefore, the effective diffusion coefficient can be determined from the slope. According to the classical theory (1), the slope dI_r/dV_r should be proportional to n^2/B^2. According to the Bohm diffusion theory (2), the slope should be proportional to n/B.

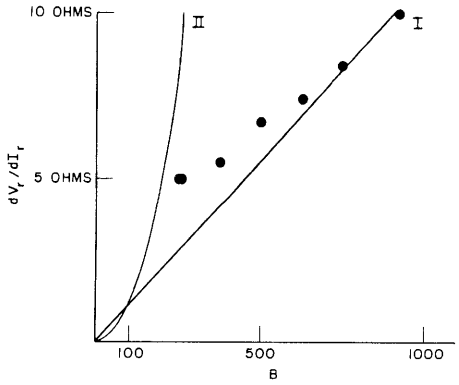

Fig. II-35. Plot of dV_r/dI_r as a function of B. Curve I: Bohm diffusion. Curve II: Classical diffusion.

In order to see this, the slope dV_r/dI_r, which is proportional either to B^2/n^2 or B/n, was measured as a function of density n and the magnetic field B. The density can be varied by changing the main axial current. In the earlier experiment, the magnetic field was changed, while the axial current was kept constant; this roughly keeps the density n constant. The result is shown in Fig. II-35, and it strongly suggests Bohm diffusion.

In that experiment, the noise was measured. It was found that the noise is independent of the magnetic field, and on one occasion it was independent of the density. The

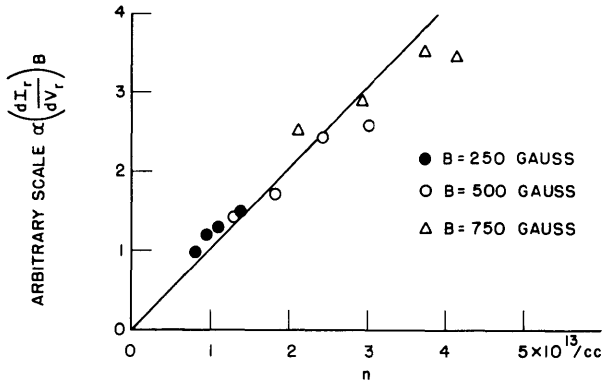

Fig. II-36. Plot of $(dI_r/dV_r)B$ as a function of B.

noise voltage is only the function of the applied radial voltage minus the floating potential of the auxiliary ring anode. The theory to account for this fact was developed, and will be published elsewhere.

In the second and third experiments, performed later, the density dependence was investigated. In the third experiment, the measurement of the density was made by means of a Langmuir probe, in a configuration somewhat different from that in the previous experiments. The plot dI_r/dV_r multiplied by the magnetic field B versus the density is presented in Fig. II-36. It shows that the points are almost linear. The mean-square deviation from this linear curve is 15 per cent.

All of the results seem to support the Bohm diffusion theory.

S. Yoshikawa

References

1. L. Spitzer, Jr., Physics of Fully Ionized Gases (Interscience Publishers, Inc., New York, 1955); see Eq. (3-16).

2. Ibid., see Eq. (3-19).

11. THE FUSION REACTOR BLANKET PROBLEM

a. Introduction

The conceptual design of a tritium regenerating blanket to surround a power-producing deuterium-tritium cycle thermonuclear reactor is being studied. Several blanket designs have been suggested in published works. However, as far as we know, previous considerations of the problem have been primarily feasibility studies and have been to some extent unrealistic. It is the intent of the present study to explore the problem in more detail from both the neutronic and the chemical and mechanical standpoints.

b. Basic Considerations

The blanket system that is under consideration must have the capability of effecting:

(a) Conversion of the kinetic energy of 14 MeV neutrons barn in D-T fusion to thermal energy at thermodynamically useful temperatures.

(b) Reproduction of tritium in sufficient quantities to fuel the thermonuclear reaction.

(c) Protection of the magnetic coils from damaging radiation.

Accordingly, provision must be made for neutron multiplication, slowing-down, and tritium-breeding capture; for high temperature heat transfer and removal within practical material limitations; for tritium extraction; and for effective neutron and gamma shielding.

In view of these requirements, several remarks may be made at the outset concerning possible materials for use in the blanket. The choice of coolant is severely limited. Water is impractical, since its use at high temperatures necessarily involves large amounts of high-pressure piping. Organic fluids are rapidly degraded by fast neutron irradiation. Liquid metals present severe circulation problems in strong magnetic fields. Gases such as CO_2 or steam are unequal to the high thermal-energy densities expected.

Fused salts appear to be the only practical alternatives, and of these only those formed with strong ionic bands may be expected to be stable under intense irradiation. Since dissociated ions in a fused-salt mix lead to serious corrosion problems at useful temperatures in almost all known containment materials, it seems that the best coolant media available are the fluoride-based fused salts.

Neutron-moderating media are equally restricted. Water and the organics are not feasible. Beryllium presents serious physical problems except in the solid metallic state, and, in addition, is excessively expensive compared with the alternatives. Zirconium hydride suffers from rapid evolution and loss of free hydrogen by diffusion at useful temperatures. Graphite presents several advantages, with no serious disadvantages. It has reasonable moderating properties; it can withstand quite high temperatures, and it is an effective containment material for most fused salts. Hence its use appears to be unequivocally recommended.

c. Blanket Characteristics

The blanket may be thought of as being composed of three successive annular regions surrounding the plasma. The first region includes the first wall, its cooling channels, and the neutron multiplication and primary slowing-down media. It is anticipated that low-energy gamma radiation arising from interactions in the plasma will be deposited in large quantities on the first solid surface enclosing the plasma. Sputtering considerations dictate that at least the first few millimeters of the first wall be of a refractory material; also, the wall must be capable of passing a high thermal flux from the first surface to a fluid coolant and must provide some structural support. The use of a solid metallic wall, possibly molybdenum, seems unavoidable.

Calculations based on a nominal first surface gamma flux of one megawatt per square

meter on one surface of a metallic wall and a fused fluoride coolant in channels that are 2-7 cm deep and at 500°C to 600°C on the other surface show that film temperature drops of approximately 20°C-60°C may be expected if the corresponding pumping power losses are to be held between 1/2 per cent and 1 per cent of the thermal energy transferred. These sizable film temperature drops, coupled with a corrosion temperature limitation of 600°C-700°C, indicate that first wall cooling in very high-density devices (first wall gamma fluxes of several megawatts per square meter) will be difficult.

Simultaneously, provision must be made in the first region for both neutron multiplication and primary slowing-down of 14 MeV neutrons. If we assume a first wall composed of a few centimeters of molybdenum on tungsten and a back-up second wall of heavy metal for neutron energy degradation by inelastic scattering, several coolant systems appear practical. These include:

(a) A pulsed mixture of LiF and BeF_2 in which multiplication is accomplished by the reaction $Be^9(n, 2n)\ 2He^4$.

(b) A fused salt based on sodium and a halogen of such constitution that most of the fast neutrons emerging from the first wall reach the second wall with sufficient energy to cause (n, 2n) reactions in the heavy metal.

(c) A lead or bismuth salt which would permit (n, 2n) multiplication in the coolant. A lead-cesium salt, for example, is attractive from both the nuclear and thermodynamic points of view.

Fissionable material could be incorporated alternately into either the fused-salt coolant or into the second wall. In this case, multiplication proceeds by both (n, 2n) and fission processes. The use of U^{238} is quite attractive in view of its relatively large fission and (n, 2n) cross sections at higher neutron energies. However, fission is inevitably accompanied by the multitudinous problems associated with fission products.

Preliminary calculations indicate that the nonfissioning systems may be expected to yield multiplication of the order of 30 per cent. A system containing the equivalent of approximately 5 cm of U^{238} will yield multiplication of the order of 150 per cent.

The second major region is that devoted to neutron moderation by elastic scattering, and to tritium regeneration. In this region the possible systems are far fewer in number. The only known isotope that has a tritium-yielding cross section large enough to be useful, and which is also avialable in large quantities, is Li^6. Chemical and thermodynamic considerations indicate that the lithium-bearing component should also be the coolant for the second region; hence the use of a lithium-based fused salt is dictated. Solubility data for HF in the fused fluorides indicate that regeneration of tritium as TF may be easily achieved. Certain binary salt mixtures, notably the eutectic $LiF\text{-}BeF_2$, have especially desirable physical and nuclear properties and can be readily contained in graphite. For these reasons, it appears evident that the second region will be composed of a matrix of high-density graphite pierced by channels containing a molten circulating

mixture of LiF and BeF_2.

A set of calculations of the (n, T) reaction rate in a homogenized graphite-LiF-BeF_2 medium, based on Fermi Age Theory, with incident neutron energies of 1 MeV, has been

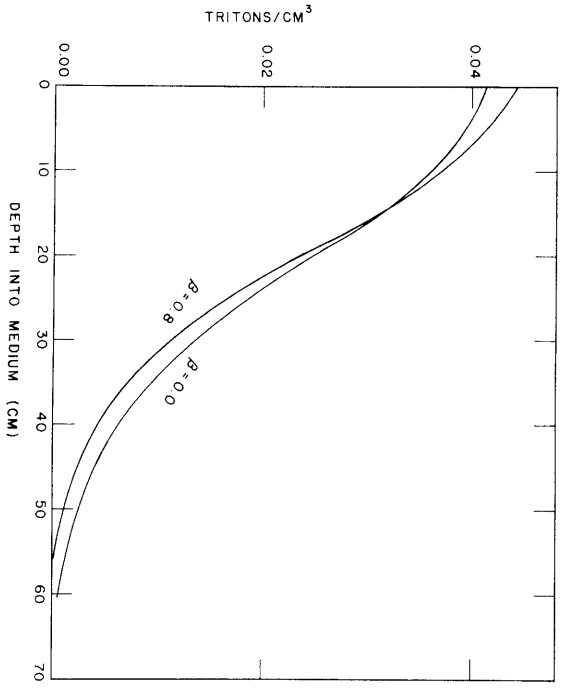

Fig. II-37. Tritium-breeding reaction rate in plane geometry. Source: 1 neutron at 1 MeV per square centimeter of surface. Medium: $(2LiF \cdot BeF_2)(1-\beta) + C(\beta)$. ($\beta$ = volume fraction of graphite.)

completed. A fortudinous characteristic of this system is that the fused-salt mix closely resembles graphite in its average neutron-scattering properties, while the rather high (n, T) cross section of Li^6 yields a strongly absorbing medium for even moderate amounts of natural lithium. The net result is that the (n, T) reaction rate is nearly independent of the Li^6 concentration. A typical plot of the tritium-breeding reaction rate versus depth into the medium is shown in Fig. II-37.

While no specific calculations have been made for the external shielding region, it appears that shielding will not be a problem, even for thermal protection of exterior superconducting magnetic-field coils.

d. Preliminary Conclusions

On the basis of the studies completed, thus far, it seems apparent that a feasible blanket system for a power-producing fusion reactor whose general characteristics are consistent with current estimates is entirely within the scope of availabe materials and

techniques. The overriding limitations appear to be those imposed by practical heat transfer, especially in the case of high specific energy density machines.

W. G. Homeyer, A. J. Impink, Jr., D. J. Rose, I. Kaplan

(Professor Kaplan is from the Department of Nuclear Engineering, M. I. T.)

References

1. L. G. Barrett, A Fusion-Fission Reactor, Report KAPL-M-LGB-14, Knolls Atomic Power Laboratory, Schenectady, New York, June 27, 1957.

2. N. C. Christofilos et al., Engineering Study of an Astron Power Reactor, Report TID 7558 Suppl. 1, U. S. Atomic Energy Commission, May 1960, pp. 18-30.

3. E. P. Johnson, Appraisal of Possible Stellerator Blanket Systems, Report NYO-7900, U. S. Atomic Energy Commission, Sept. 20, 1957.

4. P. R. Bell, J. S. Luce, R. H. Makin, Jr., E. D. Shipley, and A. Simon (eds.), The ORNL Thermonuclear Program, Report ORNL-2457, Oak Ridge National Laboratory, Jan. 15, 1958, pp. 70-78.

5. P. Powell, Proposal for a Driven Thermonuclear Reaction, Report LWS-24920, U. S. Atomic Energy Commission, Oct. 6, 1953.

12. DEVELOPMENT OF A LARGE-VOLUME SUPERCONDUCTING SOLENOID

A solenoid is being developed which uses super-conductivity to produce the magnetic field and has a magnetic volume large enough for useful experiments on plasmas. More specifically, our magnet has a working space, at room temperature, 8 inches in diameter and 4 feet long. A general view of this magnet is shown in Fig. II-38.

The development of such apparatus involves the loose coupling of two different systems – the magnetic system proper and a satisfactory dewar vessel.

a. System Generating the Magnetic Field

(i) Superconducting materials. Although many materials exhibit superconductivity, few are suitable for the production of high magnetic fields (for example, fields greater than 5 kgauss).

A notable part of our time has been devoted to studies of possible materials.

Niobium as unannealed wire was the first to be applied to the purpose (1), and is still the only one with reliably determined characteristics. The useful field range lies between 5 and 8 kgauss, with current density between 0.3 and 1×10^5 amp/cm^2 at 4.2°K. A gain of 3 kgauss accrues from operation at 1.5°K (helium vapor pressure 3.6 mm Hg). Molybdenum-rhenium (2) (49 per cent weight per cent Re) can be made to produce fields in excess of 10 kgauss with current density near 10^5 amp/cm^2, at 4.2°K; at higher fields, the critical current density falls sharply; this makes for prohibitive material

cost. Niobium-tin (3) (probably Nb_3Sn) used as a core in niobium wire has produced fields of approximately 100 kgauss, with current densities $\approx 10^5$ amp/cm^2 in the core, at 4.2°K; although preparation techniques are well developed, the brittleness and low strength of the core introduces problems of fabrication which may not be easy to solve.

Niobium-zirconium (≈ 33-50 per cent Zr) appears, at present, most promising for our purpose. Fields up to 70 kgauss at current density $> 10^4$ amp/cm^2 seem possible with thin rolled strip; even better performance may be obtained with wire. A small test solenoid of Nb-Zr immersed in liquid helium will soon be tested; final calculations for the large solenoid will be made on the basis of these tests.

(ii) Magnetic circuit. The principle of the magnetic circuit is shown in Fig. II-39. Nb-Zr wire is insulated with nylon and wound on aluminum spools, 2 inches long; 24 such spools make the 4-ft system. It is planned to operate the spools as 12 series pairs. Each pair will be individually controlled. Wire diameter will be 0.010-0.020 inch, to give a wire current of approximately 50 amp. Maximum design field strength will be approximately 30 kgauss.

The current control in Fig. II-38 allows operation on persistent current, once the field has been established. The magnetic switch is a power cryotron, using annealed niobium as the gate material. The fringing field at the switch position may reach 2 kgauss, so that no lower critical field material can be used for the gate wire. The controlling magnet will also be superconducting (Nb), for convenience. Copper current leads enter from outside the dewar and are joined to the Nb-Zr system in the liquid helium. These leads can be small because their full load is established only while starting the magnet.

The turn-on procedure is: (a) energize the magnetic switches, making all gates resistive; (b) increase all of the 12 main currents with a time constant long compared with the time $\tau = L/R$, where L is the self-inductance per spool pair (≈ 10 henries) and R is the gate resistance (≈ 1 ohm); (c) open the magnetic switches; (d) remove the power supplies.

(iii) Magnetic stresses. The magnetic stresses for a single solenoid of the sort envisaged do not give rise to any reaction outside the liquid-helium space. The equivalent magnetic pressure.

$$p = B^2/2\mu_o \qquad (1)$$

corresponds to 1 atm at 5 kgauss, and 36 atm at 30 kgauss. The solenoidal windings experience a bursting force and an axial compressive force. The radial bursting force produces a hoop tension of approximately 7 tons; the windings themselves, with layers separated by 0.002-inch mylar and clamped on the outside by a stainless-steel band, will easily take this stress. The axial stress is approximately 30 tons, and will be taken easily by the spools in compression. Finally, all 24 spools will be supported in

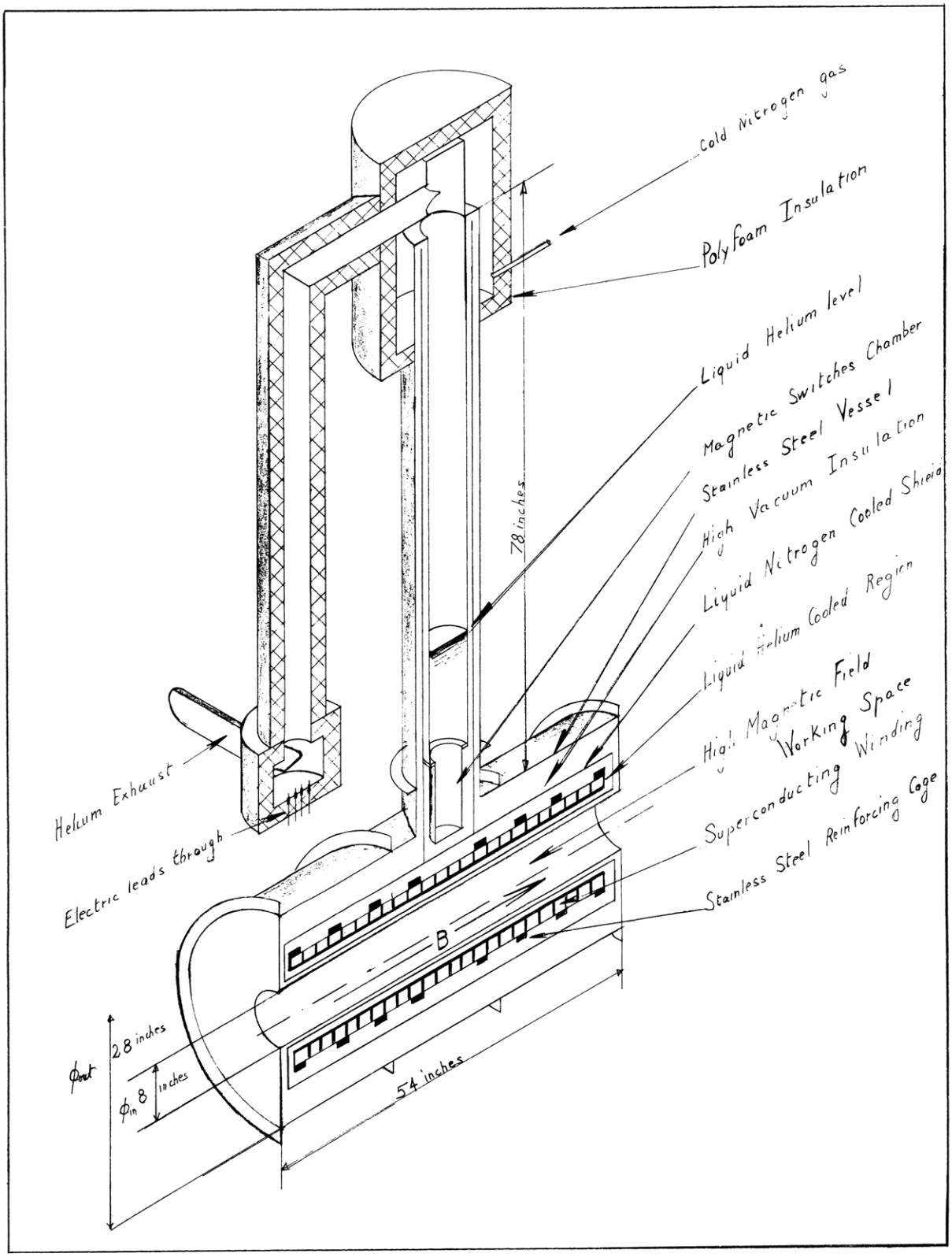

Fig. II-38. Cross section of the superconducting solenoid.

a strong stainless-steel cage.

The magnetic field possesses an energy density given by Eq. 1, which is approximately 100 joules/liter at 5 kgauss. For our effective volume of 80 liters at 30 kgauss, the energy is nearly 300 kilojoules. This energy will appear as heat if the magnetic circuit is disrupted. The specific heat of all materials (except helium) is small at liquid-helium temperatures, and the heat of vaporization of liquid helium is only 82 joules/mole at 4.2°K. It is prudent, therefore, to reduce the liquid-helium inventory to a minimum and to confine it in strong pipes. A liquid-helium bath will not be used, but rather a system of cooling coils.

The exact fate of the magnetic energy, in the event of loss of superconductivity, is a difficult problem. A change dI/dt in the superconducting windings induces azimuthal electric fields, which cause the current to reappear in the various electrically closed shells of the supporting dewar, clamps, and so forth. Thus a number of additional bursting and axial compressive stresses appear in the dewar structure. These stresses can be tolerated by the various shells; when all magnetic energy is eventually degraded to heat, the temperature rise will be negligible ($\approx 50°K$) if it is evenly distributed.

The stress considerations discussed above apply only to an isolated solenoid. Two solenoids nearby will react upon each other through their dipole fields, and the stresses must be transmitted between the sets of windings. The only method that is feasible for doing this, at the present time, is the direct connection of the two systems at helium temperature; otherwise thermal losses become excessive.

b. Cryogenic System

(i) Cooling systems. A schematic view of the cooling systems is shown in Fig. II-39. The helium system will normally operate at 4.2°K, but can be pumped to 3.6 mm Hg (1.5°K). The liquid-nitrogen system (77°K) is a shield between the room-temperature walls and the helium system, and reduces radiation losses.

The helium system consists of a 10-liter reserve tank at the bottom of the vertical stack; this tank is fed by a transfer line and control valve (also used as a throttling valve for continuous operation below 4.2°K). From the tank, helium flows to racks of cooling lines soldered to a copper sheath surrounding the coils both on the inside and the outside. Circulation depends on the thermosiphon principle — helium first flows to manifolds at the lowest axial line, then is partially boiled off on its return to the top of the racks.

For operation at 1.5°K, a pumping rate of approximately 70 cfm on the helium is required.

The nitrogen system consists of copper tubing soldered onto the copper radiation cylinders. All tubes are in series with inlet and outlet at the top of the vertical stack. Circulation is effected by a small rotary pump submerged in the nitrogen process tank. Cold gas from this tank is used to precool the top of the stack and the electric leads.

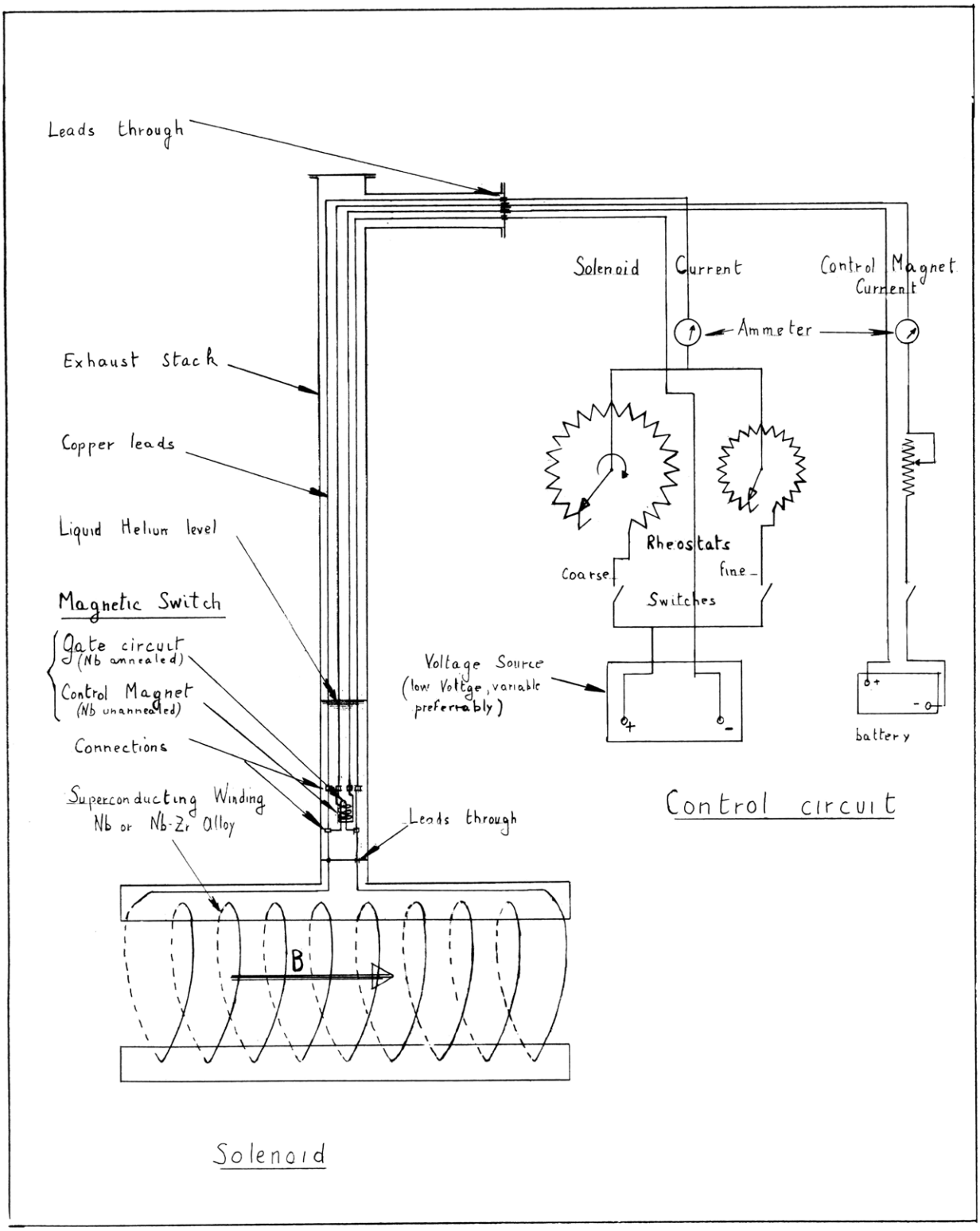

Fig. II-39. Schematic drawing of the electric circuit for a superconducting solenoid.

(ii) Heat losses and liquid gas consumption. Because the cryostat is evacuated, heat losses are limited to radiation between the walls, and conduction up the support stack and up the electrical leads.

The radiation loss is

$$W = E_{hc}\,\sigma\left(T_h^4 - T_c^4\right) A_h \qquad \text{watt} \tag{2}$$

between a hot wall of area A_h and temperature T_h, and a cold wall at temperature T_c. Here, E_{hc} is the effective coefficient of the two walls, and $\sigma = 5.67 \times 10^{-8}$ watt/m^2(°K)^4 is the Stefan-Boltzmann constant.

For a black body (ϵ=1), the radiation loss from 4.2°K to 77° K is 2 watts/m^2, and from 77°K to 300°K is 460 watts/m^2.

The emission coefficient depends on the material and configuration; for "gray-body" material, a reasonable approximation for pure annealed copper aluminum and parallel walls is

$$E_{hc} = \left[\frac{1}{\epsilon_h} + \frac{A_h}{A_c}\left(\frac{1}{\epsilon_c} - 1\right)\right]^{-1} \tag{3}$$

For an insulated radiation shield with parameters A_m and ϵ_m between the walls, we have

$$E_{hc} = \left[\frac{1}{\epsilon_h} + \frac{A_h}{A_c}\left(\frac{1}{\epsilon_c} - 1\right) + \frac{A_h}{A_m}\left(\frac{2}{\epsilon_m} - 1\right)\right]^{-1} \tag{4}$$

which shows the efficacy of additional radiation shields. We shall have radiation shields between the 300°K and 77°K walls, and between the 77°K and 4.7°K walls. Physical support for these shields reduces the improvement from that in Eq. 4; on the other hand, ϵ_m for the smooth shields will be less than ϵ_h and ϵ_c for the other walls that bear soldered pipes, etc.

Calculation of radiation losses are shown in Table II-1.

Rigid support for the solenoidal coils (≈ 500 lb at 4.2°K) without excessive heat loss requires a long re-entrant stack, as shown in Figs. II-38 and II-40. The top of the 6-ft stack us at 77°K. Its interior is finned to make a counterflow heat exchange for using the sensible heat of the outflowing gaseous helium. For the stainless-steel design shown, we expect a direct conduction loss of 0.27 watt, a heat exchange from the helium of 0.19 watt, leaving a net loss of 0.09 watt.

For losses from the electric leads, we must account both for thermal conduction and heat transfer to the ambient gas. This latter effect is not included in McFee's calculations (6).

The following copper dimensions have been chosen after tests:

(a) Solenoid current 50 Amp for turn-on: No. 24 wire, with No. 20 near the top.

Table II-1. Radiation heat losses for the LVSS-1 system.*

Location	Area[a] (m^2)	Cold Side Material	e_h	Radiation Shield Material	e_M	Hot Side Material	l_h	E_{hc}	W_{hc} (Watt)
				Liquid Helium					
Inner side	1.12	Copper[b]	0.04	Al[c]	0.02	Copper	0.03	0.0066	0.0148
Outer side	1.39	Copper	0.04	Al - 2	0.02	Copper	0.03	0.0034	0.0095
Lateral side	0.20	S. S.	0.06	Al	0.02	Copper	0.03	0.0068	0.0027
Stack	0.47	S. S.	0.06	Al	0.02	Copper	0.03	0.0068	0.0064
								Total	0.0334
				Liquid Nitrogen					
Inner side	0.95	Copper	0.03			S. S.	0.08	0.0239	10.4
Outer side	3.08	Copper	0.03	Al	0.02	S. S.	0.08	0.0065	9.2
Lateral side	0.70	Copper	0.03	Al	0.02	S. S.	0.08	0.0060	1.9
Stack	1.72	Copper	0.03			S. S.	0.08	0.0223	17.7
Process Vessel	1.70	S. S.	0.07	Al	0.02	S. S.	0.08	0.0080	6.3
								Total	45.5

*Emissivities from R. B. Scott (5).

[a]Hot side, by definition of E_{hc}.

[b]Copper soft, high purity, electrolytically polished.

[c]Al No. 1100, highly polished.

[d]Stainless steel No. 347, highly polished.

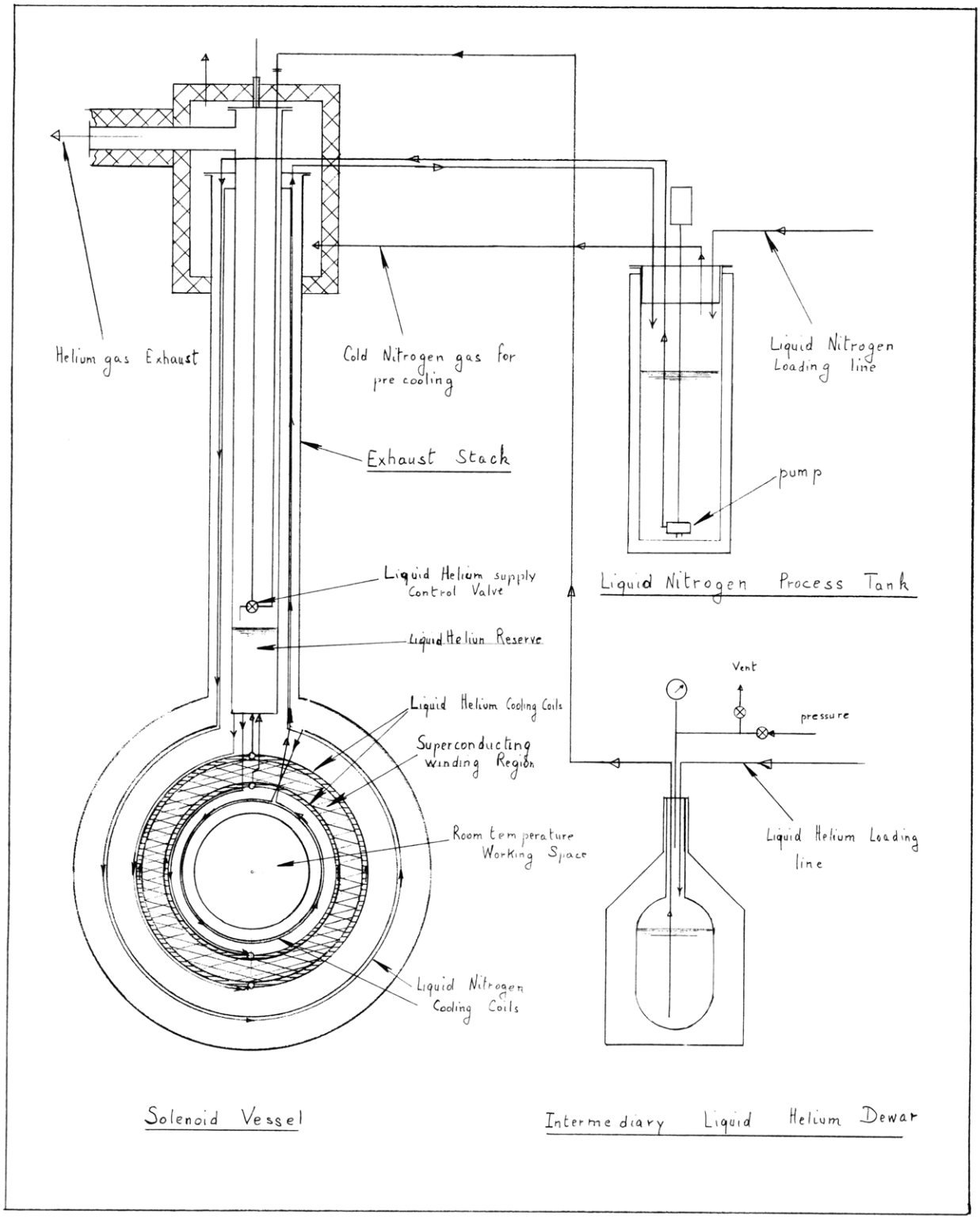

Fig. II-40. Schematic drawing of the cooling system for the superconducting magnet.

(b) Magnetic switch: No. 28 wire, with No. 24 near the top.

For 96 wires, 10 feet long, the losses are calculated as: (a) straight conduction 0.25 watt; (b) heat exchange from helium 0.03 watt, giving a net loss of 0.22 watt.

Liquid-helium consumption, for an expected heat leakage of 0.34 watt from the 4.2°K region, is approximately 0.46 liters/hour. At 1.5°K, consumption would be approximately doubled.

Approximately 25 watts are lost by conduction between 77°K and 300°K; the total heat loss from the 77°K-region is, therefore, approximately 70 watts, giving a liquid-nitrogen consumption of approximately 1.5 liters/hr.

This system will be able to withstand a moderate torque arising from stray ferromagnetic material, and so forth. A torque of 1400 ft-lb can be applied safely to the 4.2°K-system in any direction.

Vertical contraction of the cooled stack is approximately 0.2 inch.

D. J. Rose, L. J. Donadieu

References

1. L. J. Donadieu, S. H. Autler, Quarterly Progress Report No. 59, Oct. 15, 1960, p. 27.

2. L. J. Donadieu, unpublished results, May 1961.

3. J. E. Kunzler, E. Buehler, F. S. L. Hsu, and J. H. Wernick, Phys. Rev. Letters 6, 89 (1961).

4. J. E. Kunzler, Paper V3, Bull. Am. Phys. Soc. II, 6, 298 (1961).

5. R. B. Scott, Cryogenic Engineering (D. Van Nostrand Company, New York, 1959).

6. R. McFee, Rev. Sci. Instr. 30, 102 (1959).

II-C. PLASMA MAGNETOHYDRODYNAMICS AND ENERGY CONVERSION*

Prof. E. N. Carabateas
Prof. J. A. Fay
Prof. G. N. Hatsopoulos
Prof. W. D. Jackson
Prof. H. P. Meissner
Prof. D. C. Pridmore-Brown
Prof. A. H. Shapiro
Prof. H. H. Woodson
L. Y. Cooper
R. S. Cooper
D. M. Dix
D. A. East
W. H. Heiser
E. D. Hoag
S. A. Khayatt
G. B. Kliman
P. Klimowski
A. Kniazzeh
M. F. Koskinen
A. T. Lewis
J. R. Melcher
W. T. Norris†
J. P. Penhune
E. S. Pierson
J. W. Poduska
J. H. Wasserlein
G. L. Wilson

1. MAGNETOHYDRODYNAMIC AC GENERATOR WITH GAS LOSSES

H. A. Haus has reported (1) a one-dimensional analysis of a magnetohydrodynamic (MHD) ac generator in which longitudinal hydromagnetic waves in an infinitely conducting gas, flowing at supersonic speed, couple with an electric circuit to obtain amplification of signals in the circuit. With properly phased feedback around the circuit, the system will oscillate, and generate ac electric power. The primary power source consists of kinetic and potential energy in the gas flowing into the interaction region. His analysis indicated a theoretical possibility, but gave no indication of the conditions under which power generation could be accomplished with a real system having losses.

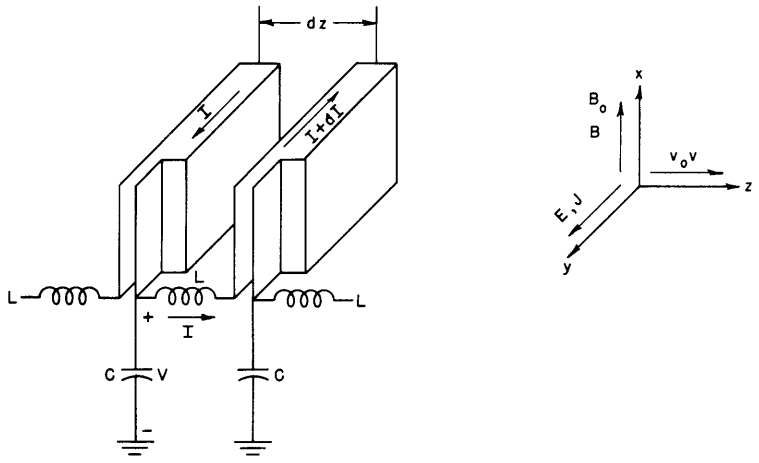

Fig. II-41. System circuit with variables and their directions defined.

The purpose of the present report is to extend Haus' analysis to the slightly lossy

*This work was supported in part by National Science Foundation under Grant G-9330, and in part by WADD Contract AF33(616)-7624 with Flight Accessories Laboratory, Wright-Patterson Air Force Base, Ohio.

†Commonwealth Fellow from England, 1960-61.

case to provide a theoretical basis for determining the possibility of power generation with real gases.

The system that is to be analyzed is essentially that shown previously by Haus (2) and reproduced here with minor changes as Fig. II-41. The variables and their directions are defined in our figure. Time-average quantities are denoted by subscript o; small-signal ac quantities are represented by variables with no subscripts. Variables needed in addition to those shown in Fig. II-41 are the gas variables: pressure (p_o, p), density (ρ_o, ρ), and temperature (T_o, T). The gas is assumed to have a constant, scalar conductivity, σ, and no viscosity or heat conduction. The problem is assumed to be one-dimensional, so that variables will be functions of only coordinate z and time t.

Haus showed that in such a system, with a perfectly conducting gas flowing with an average velocity v_o, waves of frequency ω will propagate with propagation constants

$$\beta_o = \frac{\omega}{v_o \pm c} \tag{1}$$

with the velocity c given by

$$c = \left(\frac{\beta_o^2}{\mu_o \rho_o} + \gamma \frac{p_o}{\rho_o} \right)^{1/2} \tag{2}$$

where μ_o is the permeability of free space, and γ is the ratio of specific heats for gas. The two waves relating to the propagation constants of Eq. 1 have phase velocities of $v_o + c$ and $v_o - c$. When $v_o > c$, defined here as supersonic velocity, the wave with phase velocity $v_o - c$ is a slow wave that carries negative power in the forward direction and can couple with a circuit to achieve amplification (1).

In the analyses that follow the losses will be assumed to perturb the idealized solutions obtained by Haus; consequently, his answers will be used to define perturbations.

a. Waves in Gas without Circuit

The equations describing the small signal behavior of the system with small losses are those given by Haus (3), with a modified Ohm's law. These equations are:

Force Equation:
$$\rho_o \left(\frac{\partial}{\partial t} + v_o \frac{\partial}{\partial z} \right) v = - \frac{\partial p}{\partial z} - J B_o \tag{3}$$

Maxwell's Equations:
$$\frac{1}{\mu_o} \frac{\partial B}{\partial z} = J \tag{4}$$

$$\frac{\partial E}{\partial z} = \frac{\partial B}{\partial t} \tag{5}$$

Continuity Equation: $$\left(\frac{\partial}{\partial t} + v_o \frac{\partial}{\partial z}\right)\frac{\rho}{\rho_o} = -\frac{\partial v}{\partial z} \tag{6}$$

Ohm's Law: $$J = \sigma(E+vB_o+v_oB) \tag{7}$$

Adiabatic Equation of State: $$\frac{p}{p_o} = \gamma\frac{\rho}{\rho_o} \tag{8}$$

When the space-time dependence $\exp[j(\omega t-\beta z)]$ is assumed for each small-signal variable, Eqs. 3-8 can be combined to obtain the dispersion relation

$$(\omega-\beta v_o)^2 = c_s^2\beta^2 + \frac{c_b^2\beta^2}{1+\dfrac{\beta^2}{j\mu_o\sigma(\omega-\beta v_o)}} \tag{9}$$

where $c_s = \left(\dfrac{\gamma p_o}{\rho_o}\right)^{1/2}$ is the velocity of sound, and $c_b = \dfrac{B_o}{(\mu_o\rho_o)^{1/2}}$ is the Alfvèn velocity.

When losses are assumed to be small enough so that

$$\frac{\beta^2}{\sigma\mu_o(\omega-\beta v_o)} \ll 1 \tag{10}$$

Eq. 9 can be put into the form

$$(\omega-\beta v_o)^2 = c^2\beta^2 - \frac{c_b^2\beta^4}{j\sigma\mu_o(\omega-\beta v_o)} \tag{11}$$

where $c^2 = c_s^2 + c_b^2$. Note that if $\sigma \to \infty$, this reduces to the dispersion relation that yields the propagation constants of Eq. 1.

Because of the assumption of small losses in Eq. 10, the propagation constant β is assumed to be a small perturbation from the lossless case. Using Eq. 1, we obtain

$$\beta = \frac{\omega}{v_o \pm c} + \delta_\ell = \beta_o + \delta_\ell \tag{12}$$

where δ_ℓ is a small perturbation caused by losses, and satisfies the condition $\delta_\ell \ll \beta_o$. Substitution of Eq. 12 in Eq. 11, retention of only first-order terms in δ_ℓ, and simplification yield

$$\delta_\ell = -j\frac{c_b^2\omega^2}{2\sigma\mu_o c^2(v_o\pm c)^3} \tag{13}$$

where the plus sign is for the fast wave, and the minus sign is for the slow wave.

b. Waves with Lossy Gas and Lossless Circuit

The purpose here is to combine Haus' analysis for the gain of a coupled circuit with the analysis just given to obtain an expression for gain in the presence of small losses only in the gas.

In the system shown in Fig. II-41, the L and C of the circuit are per unit length in the z-direction. The distributed coupling coils shown as single turns are assumed to have n turns per unit length in the z-direction. The small-signal equations needed are Eqs. 3-8, with modification of Eq. 4 to include the circuit current,

$$\frac{1}{\mu_o}\frac{\partial B}{\partial z} = J - \frac{\partial I}{\partial z} \tag{14}$$

modification of Ohm's law (Eq. 7) to include finite conductivity,

$$J = \sigma(E+vB_o+v_oB) \tag{15}$$

and addition of the circuit equations

$$\frac{\partial V}{\partial z} = -L\frac{\partial I}{\partial t} + n\frac{\partial B}{\partial t} \tag{16}$$

$$\frac{\partial I}{\partial z} = -C\frac{\partial V}{\partial t} \tag{17}$$

For the case with no coupling to the gas (n=0), the propagation constant of the circuit is $\beta_o = \omega(LC)^{1/2}$, which leads to a circuit phase velocity of $v_c = (LC)^{-1}$. As Haus pointed out (1), strong interaction between circuit and wave occurs only when the circuit wave is approximately synchronous with the fast or the slow gas wave; and, furthermore, circuit gain can be achieved only when the circuit wave and the slow gas wave are approximately synchronous.

When a space-time dependence $\exp[-j(\omega t-\beta z)]$ is assumed for each of the variables, simultaneous solution of the relevant equations yields

$$(\omega-\beta v_o)^2 = c_s^2\beta^2 + \frac{c_b^2\beta^2\left(1-\dfrac{\beta_c^2\dfrac{n\mu_o}{L}}{\beta^2-\beta_c^2}\right)}{1+\dfrac{\beta^2}{j\mu_o\sigma(\omega-\beta v_o)}\left(1-\dfrac{\beta_c^2\dfrac{n\mu_o}{L}}{\beta^2-\beta_c^2}\right)} \tag{18}$$

For strongest coupling, it is assumed that the circuit wave is synchronous with a gas wave:

$$\beta_c = \beta_o = \frac{\omega}{v_o \pm c} \tag{19}$$

and, furthermore, that loss and gain both cause only a small change in propagation constant:

$$\beta = \beta_o + \delta \tag{20}$$

where $\delta \ll \beta_o$. Substitution of Eqs. 19 and 20, in Eq. 18, making the assumption of weak enough coupling so that

$$\frac{n\mu_o}{L} \sim \left(\frac{\delta}{\beta_o}\right)^2$$

and keeping only first-order terms in δ, after some manipulation, yields

$$\delta^2 + j\,\frac{c_b^2\omega^2\delta}{2\mu_o\sigma c^2(v_o \pm c)^3} \mp \frac{c_b^2\omega^2\,\frac{n\mu_o}{L}}{4c(v_o \pm c)^3} = 0 \tag{21}$$

Here, the upper sign denotes coupling to the fast wave, and the lower sign denotes coupling to the slow wave.

The interest now is in gain; consequently, only coupling to the slow wave will be considered. Thus,

$$\beta_c = \beta_o = \frac{\omega}{v_o - c}$$

and if we use the definition of δ_ℓ in Eq. 13, and a gain constant δ_g given by Haus (1), we obtain

$$\delta_g = j\,\frac{c_b}{c}\,\beta_o\left(\frac{c}{(v_o - c)}\,\frac{n\mu_o}{4L}\right)^{1/2} \tag{22}$$

Equation 21 can be put into the form for coupling with the slow wave

$$\delta^2 - \delta_\ell\delta - \delta_g^2 = 0 \tag{23}$$

for which the solutions are

$$\delta = \frac{\delta_\ell}{2} \pm \left(\frac{\delta_\ell^2}{4} + \delta_g^2\right)^{1/2} \tag{24}$$

The solution that has the plus sign represents an attenuated wave and is of no interest. The solution that yields gain is

Table II-2.

Gas	Temperature T_o(°K)	Pressure p_o(atm)	Condition σ(mhos/m)	Sound Velocity C_s(m/sec)	Power Gain G_p	Slow-Wave Length λ(m)	Maximum Frequency f(cps)	Minimum Length ℓ(m)
CO_2 plus K seed	3000	1	80	860	100	125	10	830
					10	125	10	500
					2	125	10	270
Argon	20,000	1	10^4	3500	100	0.24	20,000	1.60
					10	0.24	20,000	0.97
					2	0.24	20,000	0.53
Hydrogen	20,000	23	10^4	20,000	100	0.044	6.5×10^5	0.29
					10	0.044	6.5×10^5	0.18
					2	0.044	6.5×10^5	0.10

$$\delta = \frac{\delta_\ell}{2}\left[1 - \left(1 + \frac{4\delta_g^2}{\delta_\ell^2}\right)^{1/2}\right] \tag{25}$$

It is interesting to note that Eq. 25 indicates wave growth for any finite value of the constants. Furthermore, when $\delta_g \to 0$ ($n \to 0$, see Eq. 22) there is no attenuation or growth. This is the wave on the lossless circuit alone.

c. Some Approximate Results

When the transmission line is loaded at its input and output terminals so that no reflections occur, and the assumption of only a forward-traveling circuit wave is satisfied, over a line of length ℓ, the power gain is given by

$$G_p = \frac{1}{4} e^{|\delta|\ell} \tag{26}$$

To obtain some order-of-magnitude estimates of device sizes and operating frequencies, the following relations are assumed:

$$C_b = C_s$$

$$C = \sqrt{2}\, C_b$$

$$v_o - C = C$$

$$\frac{n\mu_o}{L} = 0.1$$

$$\sigma\lambda C = 1.25 \times 10^7$$

From available data on combustion gases (4), argon (5), and hydrogen (6), with the conditions assumed above and Eq. 26 used, the quantities listed in Table II-2 were calculated. The essential results of these calculations are the frequency, f, and length, ℓ. These represent the maximum frequency and minimum length for which the desired power gain is possible with the assumed conditions. Operation is possible at a lower frequency and greater length with the desired power gain.

The frequencies and lengths listed in Table II-2 indicate that for combustion gases at temperatures that can be contained by material walls, the size is too large to be practical, even for central-station power generation. The results for argon and hydrogen indicate that experiments of laboratory size are possible. Hence experiments can be

performed that will give us more knowledge about the interactions, especially about the departure of the operation of a three-dimensional device from that predicted by a one-dimensional model, and about the large-signal operation.

H. H. Woodson

References

1. H. A. Haus, Magnetohydrodynamic ac generator, Quarterly Progress Report No. 60, Research Laboratory of Electronics, M. I. T., Jan. 15, 1961, pp. 46-50.

2. Ibid., see Fig. II-18, p. 49.

3. Ibid., see Eqs. 1-6, p. 47.

4. R. J. Rosa and A. R. Kantrowitz, Magnetohydrodynamic Energy Conversion Techniques, Research Report 86, Avco-Everett Research Laboratory, Everett, Massachusetts, April 1959.

5. S. C. Lin, A. R. Kantrowitz, and E. L. Resler, Electrical conductivity of highly ionized argon produced by shock waves, J. Appl. Phys. 26, 95 (1955).

6. E. B. Turner, Equilibrium Hydrodynamic Variables behind a Normal Shock Wave in Hydrogen, Report GM-TR-0165-00460, Space Technology Laboratories, Physical Research Laboratory, Los Angeles, California, Aug. 26, 1958.

2. MAGNETIC REFLECTION OF A SHOCK-PRODUCED PLASMA

This report consists of part of a thesis with the same title, submitted to the Department of Electrical Engineering, M. I. T., June 1961, in partial fulfillment of the requirements for the degree of Bachelor of Science.

a. Introduction

In a previous report (1) an experimental apparatus was described in which the interaction of a shock-produced plasma with a weak magnetic field was studied. That apparatus has been modified to allow application of magnetic fields strong enough to significantly affect the gas flow through the field. The purpose here is to report some further results obtained with this equipment with the objective of learning more about how a pulsed plasma, parametric energy converter (2, 3) will operate.

b. Experiment

The geometry used is shown in Fig. II-42; in this figure a coaxial driver replaces the T-tube driver described in Quarterly Progress Report No. 51 (page 28). This new driver produces more uniform shocks at higher magnetic Reynolds numbers than those generated by the T-tube driver. The shock passes into a solenoidal coil that is driven with a high-current, crowbarred, pulse system, for which a schematic diagram is shown in Fig. II-43, to produce a maximum field of 30,000 gauss. The pulse is long enough to

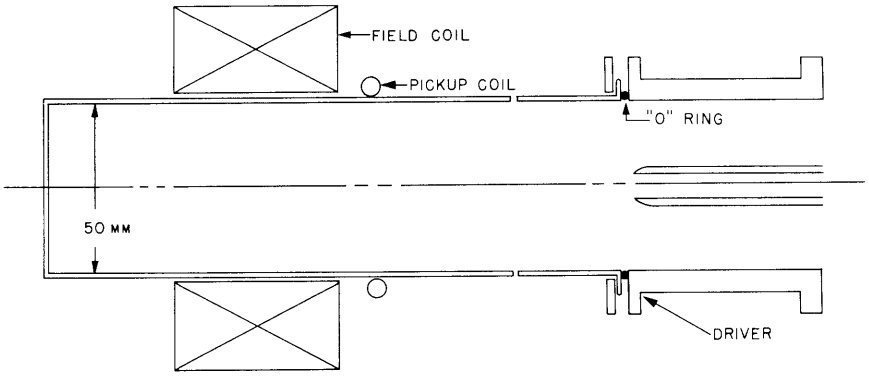

Fig. II-42. Shock-tube geometry.

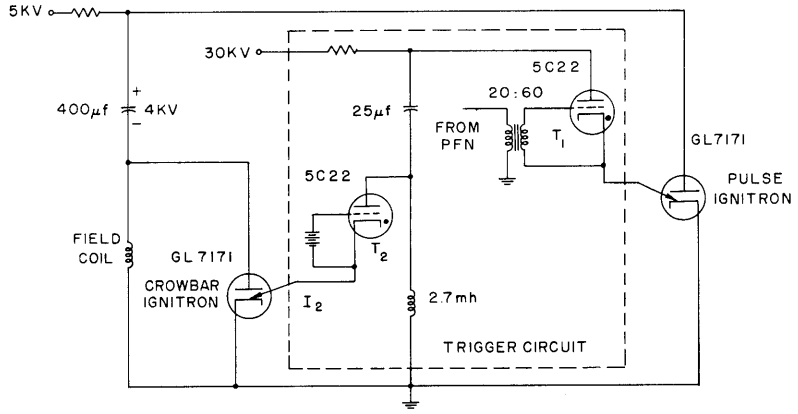

Fig. II-43. Ignitron pulse circuit.

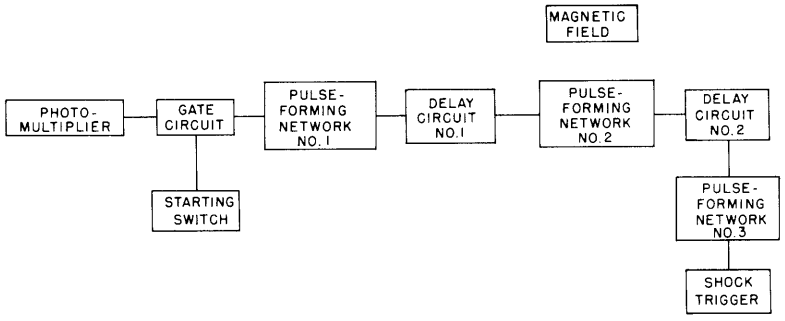

Fig. II-44. Timing system.

create a magnetic field that looks essentially constant to the plasma.

The driver discharge system consists of a 2.5-μfd, 30-kv capacitor discharging through a parallel-plate transmission line. The system has a ringing frequency of 300 kc. All measurements are made in hydrogen gas over an initial pressure range 0.1-1.0 mm Hg. The initial discharge voltage is 24 kv and generates 7-10 cm/μs shock velocities.

Measurements were made with a rotating-mirror camera that is capable of producing 0.3 μs/mm writing speeds. The shock tube was covered with an opaque material, except for a thin slit along the tube, which was divided by vertical stripes with 1-cm spacing. The smear camera was synchronized with the rest of the system through delay and pulse

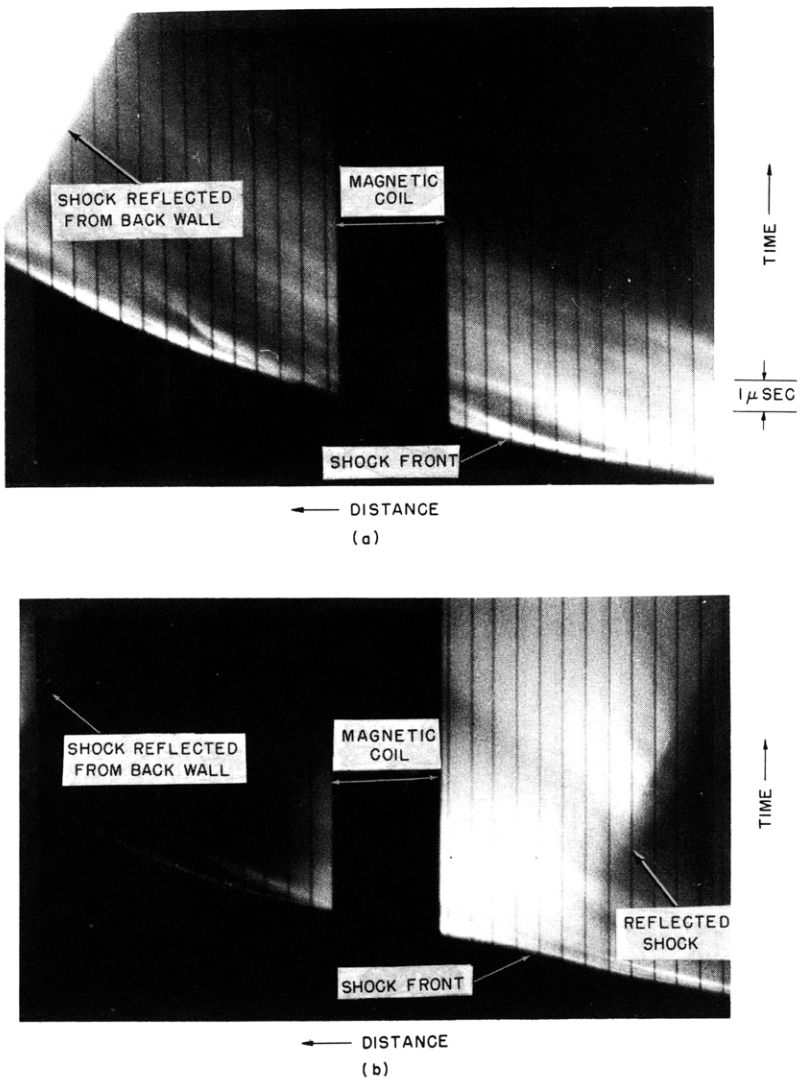

Fig. II-45. Smear camera pictures along the tube.

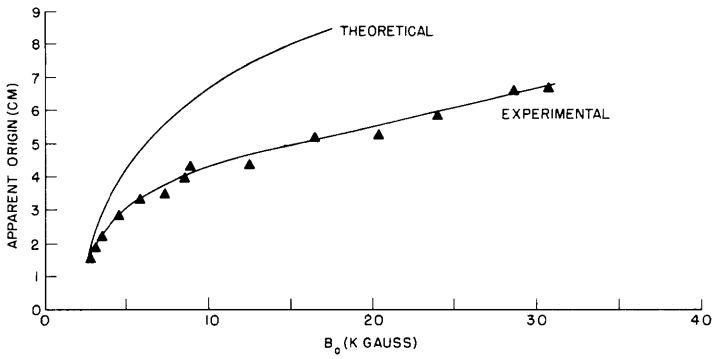

Fig. II-46. Reflected shock origin versus axial field strength, B.

circuitry which is illustrated in the block diagram of Fig. II-44. Figure II-45a is a typical smear camera photograph taken along the tube with no applied magnetic field. The shock wave is moving toward the left, with a reflected shock coming off the end wall of the tube. Figure II-45b is taken with an applied magnetic field of 24,000 gauss. A shock is seen reflecting off the field of the coil. At this high field, a large fraction of the gas does not pass through; this is verified by the difference in light intensities of the shocks reflected by the end wall.

By using pictures similar to those of Fig. II-45, a curve is plotted of the apparent shock origin as a function of the applied magnetic flux density at the center of the coil. The apparent origin is obtained by extrapolating the reflected shock front to the front of the incoming shock wave and measuring the distance between this intersection and the coil center. The experimental curve measured at an initial pressure of 0.3 mm Hg is presented in Fig. II-46.

c. Theory

As the gas enters the field coil, the forces produced by the induced currents and the magnetic fields have two effects. If cylindrical symmetry is assumed, it follows that only azimuthal currents flow.

$$\vec{J} \times \vec{B} = -\sigma V B_r^2 \vec{i}_z - \sigma V B_r B_z \vec{i}_r \qquad (1)$$

This interaction is illustrated in Fig. II-47. The first term in Eq. 1 is a force density in the axial direction which opposes the motion of the oncoming gas. The second term is a force density that tends to channel the gas into a smaller cross section as the gas approaches the center of the coil. These two force densities are strongly coupled through changes in parameters in the gas.

The gas is reflected by the force in the axial direction in Eq. 1. This force must

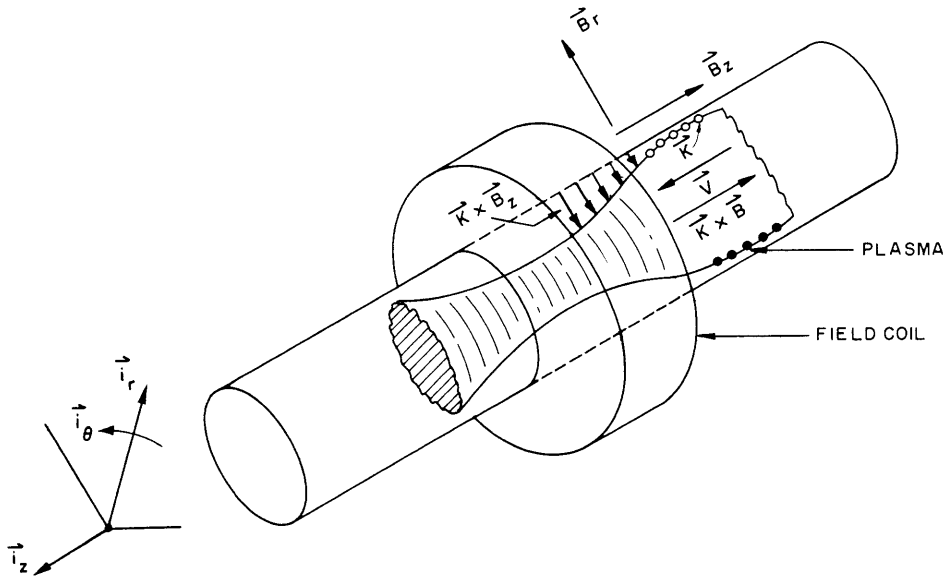

Fig. II-47. Plasma moving into the magnetic coil.

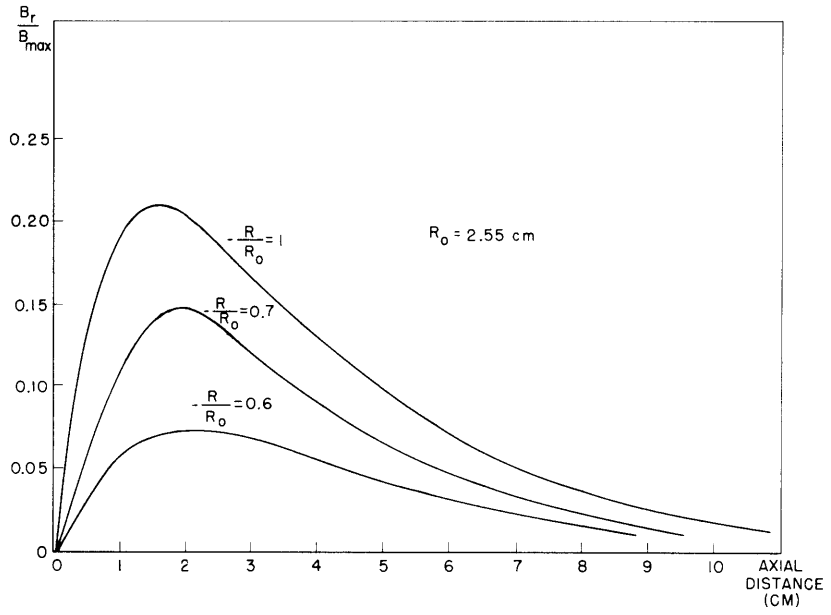

Fig. II-48. Ratio of radial to axial field versus axial distance.

have a certain finite value before the reflected gas is steepened into a shock.

The curves of Fig. II-48 show the ratio of the radial field to the maximum field at the coil center, plotted for different radial positions as a function of the axial distance from the center of the coil. It is apparent that an incoming slug of gas can never be reflected from a distance closer to the center of the coil than the axial position at which the radial field is a maximum. Secondly, if channeling is neglected, and gas conductivity is constant, the gas reflects from a distance farther away from the center of the coil as the applied field is raised. This is done in such a manner as to keep the axial force term in Eq. 1 constant, and therefore the radial magnetic-field component constant. Utilizing this condition along one of the curves of Fig. II-48, we can obtain a theoretical curve that neglects the channeling effects on the gas. This curve is plotted in Fig. II-46 as the theoretical curve that is normalized to the threshold point of the experimental data. The discrepancy between the curves of Fig. II-46 can be explained through the effects of channeling. Along a line of constant B_o the experimental curve indicates that the force exerted on the gas is less than predicted, as evidenced by the shorter distance between the coil center and the apparent origin on the experimental curve as compared with that of the theoretical curve. Figure II-48 indicates that for a lower radius of the gas slug, the radial field, and thus the axial force, is decreased. This decrease in plasma radius is due to channeling. Figure II-46 also verifies the fact that the shock is reflected from a minimum apparent origin coinciding, within experimental error, to the axial position of peak radial field. Also, the similarity in the shapes of the two curves verify the dependence of the reflecting force on B_r alone.

By placing a slit across the tube one centimeter upstream from the field coil, a smear camera photograph of the shock can be taken as it enters the magnetic field. Pictures are taken at 650 cps (0.32 μs/mm writing speed), for various applied magnetic fields. Figure II-49 shows three pictures taken with the shocks moving toward the left. Figure II-49a is with no applied field. The shock front is planar, but the gas behind is turbulent and not uniform. Figure II-49b and 49c are with applied fields of 8000 gauss and 20,000 gauss, respectively. The plasma is strongly channeled, as these photographs demonstrate. The incoming velocities of all of these pictures are about the same. However, the gas diffuses back into the magnetic field in much less time in Fig. II-49b than in Fig. II-49c. This increase in diffusion time indicates that the magnetic Reynolds number, and therefore the conductivity of the gas have increased considerably, as indicated by the following equation:

$$R_m = \mu\sigma V \ell_c \approx \frac{B_{induced}}{B_{imposed}} \approx \frac{\tau_d}{\tau_t} \qquad (2)$$

where μ is the magnetic permeability, σ is the gas conductivity, V is the gas velocity, ℓ_c is a characteristic length of the interaction (in this case, the plasma radius), τ_d is

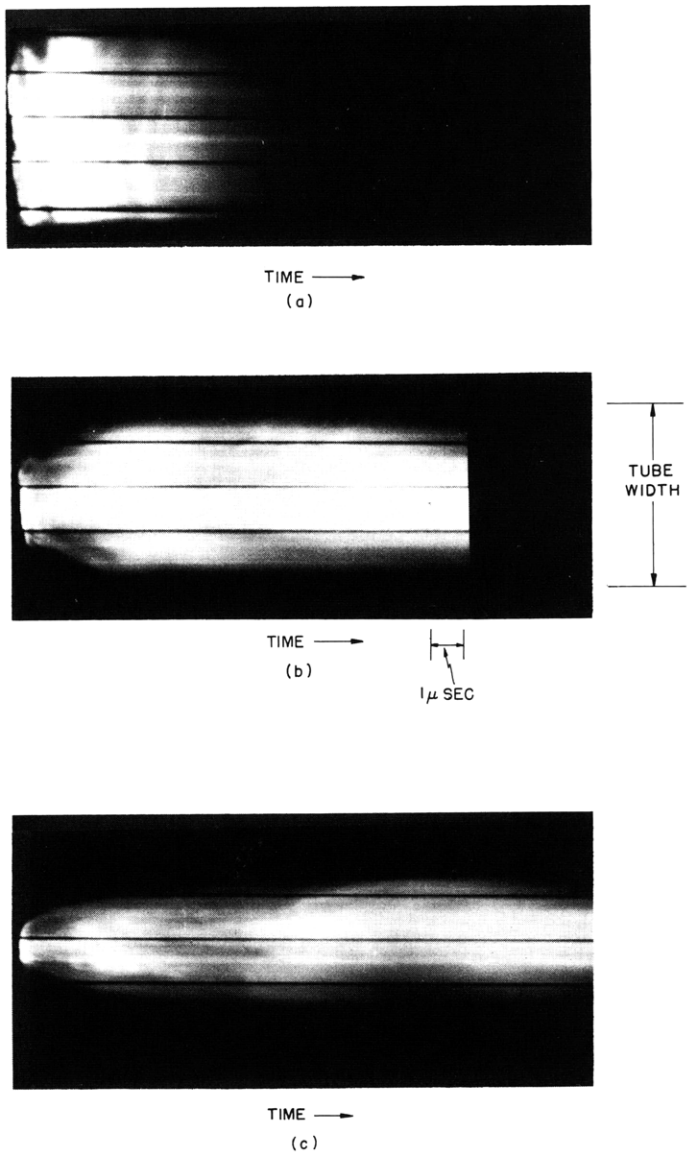

Fig. II-49. Smear camera pictures across the tube.

the time needed for the gas to diffuse into the field, and τ_t is the time needed for the gas to travel a characteristic length through the field.

Finally, measurements made on the transmitted shock indicate that its velocity does not change appreciably from that of the incident shocks, although applied magnetic fields ranged from 1000-30,000 gauss.

d. Conclusions

The experimental data taken indicate two important results concerning the interaction of a plasma with the magnetic field of a solenoidal coil.

First, a reflected shock wave is formed and a major part of the gas is stopped. This reflected shock is produced purely through the interaction of the radial-field component with the plasma. The presence of this interaction has been verified for gas pressures ranging from 0.3 mm Hg to 6 mm Hg at applied magnetic fields ranging from 1000-30,000 gauss, with incident shock velocities of approximately 10 cm/μs. Also, as the gas enters the coil it is channeled as the magnetic field is intensified.

Second, the conductivity increases considerably as the gas is compressed. This indicates that a design for an energy converter of this type need not require initial magnetic Reynolds numbers as high as calculated (3) because the conductivity and magnetic Reynolds number increase as the plasma enters the field coil.

G. L. Wilson

References

1. H. H. Woodson and A. T. Lewis, Plasma magnetohydrodynamic experiments, Quarterly Progress Report No. 59, Research Laboratory of Electronics, M.I.T., Oct. 15, 1960, pp. 40-45.

2. H. H. Woodson and W. D. Jackson (eds.), Summary Report: Study of Electrical Energy Conversion Systems for Future Aircraft, WADD Technical Report No. 60-148, Electronic Systems Laboratory, M.I.T., February 1960, pp. 67-89.

3. H. H. Woodson and A. T. Lewis, Some requirements for the operation of magnetohydrodynamic induction generators, Proc. Second Symposium on the Engineering Aspects of Magnetohydrodynamics, Power Conversion Session (Columbia University Press, New York, 1961).

3. SUMMARY OF SOME RESULTS IN THE STUDY OF DECAYING MAGNETOFLUID-DYNAMIC FLOWS

In his recent monograph (1), Wiener has presented the Calculus of Random Functionals. This calculus has been used to analyze decaying turbulent flows (2). In this report the results of that analysis are extended to hydromagnetic flows.

Consider a uniform, incompressible, homogeneous, Newtonian fluid with a scalar conductivity, σ. Suppose that some time ago an isotropic field of turbulence was established, and by time $t = 0$ has settled to the final stages of decay. At time $t = 0$, let a uniform magnetic field of strength B_0 be applied in the y direction, as shown in Fig. II-50.

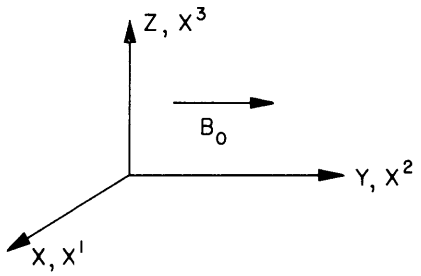

Fig. II-50.

The turbulent velocity field may be expanded in homogeneous polynomial functionals (3) as follows:

$$u^i = \sum_0^\infty \nu \int_{-\infty}^{\infty} \nu \int K_\nu^i(x+x_1, y+y_1, z+z_1; \ldots; x+x_\nu, y+y_\nu, z+z_\nu; t) \ldots \prod_{j=1}^{\nu} dr(s_j, \alpha)$$

where $r(s, \alpha)$ is the stochastic process of time-space and phase.

Now, for isotropic turbulence,

$$K_o^i \equiv 0$$

and in the final stages of decay, the dominant term is K_1^i. Hence, we write

$$u^i \approx \int_{-\infty}^{\infty} K_1^i(x+x_1, y+y_1, z+z_1; t)\, dr(s_1, \alpha)$$

and similarly for the pressure, we write

$$P = \int_{-\infty}^{\infty} w_1(x+x_1, y+y_1, z+z_1; t)\, dr(s_1, \alpha)$$

Let

$$R^{ij}(\epsilon^k) = \overline{u^i(x^k, t)\, u^j(x^k+\epsilon^k, t)}$$

$$\triangleq \left(\frac{1}{2\pi}\right)^3 \int_{-\infty}^{\infty} 3 \int \Phi^{ij}(\lambda_k, t) \exp\left(j\lambda_k \epsilon^k\right) d\tau_k$$

For isotropic turbulence, it has been shown (2) that

$$\Phi^{ij} = \left[\mu^2 \delta^{ij} - \lambda_i \lambda_j + j\mu e^{ijk} \lambda_k\right] F(\mu) \exp\left(-2 \frac{\mu^2}{R} t\right.$$

where $\mu^2 = \lambda_k \lambda_k$, and $F(\mu)$ depends on the initial condition. The physical situations of interest require that

$$\lim_{\mu \to 0} F(\mu) = \text{constant} \triangleq a,$$

$$F(\mu) \geq 0 \text{ for every real } \mu,$$

and

$$\int_0^\infty \mu^4 F(\mu)\, d\mu \text{ is bounded.}$$

Hence, in the final stages of decay,

$$\Phi^{ij} \rightarrow a\left[\mu^2\delta^{ij} - \lambda_i\lambda_j + j\mu\, e^{ijk}\lambda_k\right] \exp\left[-2\frac{\mu^2}{R}(t+t_o)\right]$$

where $(-t_o)$ is the time when the flow field was established.

When the B-field is applied, the normalized, dynamic equations of motion (with kinematic effects neglected) become

$$\frac{\partial K_1^i}{\partial t} - \frac{1}{R}\nabla^2 K_1^i + \frac{\partial w_1}{\partial x^i} = -\frac{M^2}{R}\left(K_1^i - \delta_2^i K_1^2\right)$$

where M is the Hartmann number.

The continuity equation gives

$$\frac{\partial K_1^i}{\partial x^i} = 0$$

Now let

$$\begin{Bmatrix} K_1^i \\ w_1 \end{Bmatrix} = \left(\frac{1}{2\pi}\right)^3 \int_{-\infty}^{\infty} \int^3 \begin{Bmatrix} A_1^i(\lambda_k, t) \\ W_1(\lambda_k, t) \end{Bmatrix} \exp\left(j\lambda_k x^k\right) d\tau_k$$

Then the solution of the dynamic equation is

$$A_1^1 = \lambda_3 N_1 \exp\left(-\frac{\mu^2 + M^2}{R}t\right) - \frac{\lambda_1\lambda_2}{\lambda_1^2 + \lambda_2^2} C_1 \exp\left[-\frac{1}{R}\left(\mu^2 + M^2\frac{\lambda_2^2}{\mu^2}\right)t\right]$$

$$A_1^2 = C_1 \exp\left[-\frac{1}{R}\left(\mu^2 + M^2\frac{\lambda_2^2}{\mu^2}\right)t\right]$$

$$A_1^3 = -\lambda_1 N_1 \exp\left(-\frac{\mu^2 + M^2}{R}t\right) - \frac{\lambda_3\lambda_2}{\lambda_1^2 + \lambda_2^2} C_1 \exp\left[-\frac{1}{R}\left(\mu^2 + M^2\frac{\lambda_2^2}{\mu^2}\right)t\right]$$

where N_1 and C_1 are functions of λ_k only.

Furthermore, for axisymmetric, homogeneous turbulence

$$\begin{aligned}\Phi^{ij} = {} & \Phi_1\lambda_i\lambda_j + \Phi_2\delta^{ij} \\ & + \Phi_3\left\{\lambda_2\left(\lambda_i\delta_2^j + \lambda_j\delta_2^i\right) - \mu^2\delta_2^i\delta_2^j\right\} \\ & + \Phi_4\left\{\left(\lambda_2\lambda_i - \delta_2^i\mu^2\right)e^{j\ell m} + \left(\lambda_2\lambda_j - \delta_2^j\mu^2\right)e^{i\ell m}\right\}\lambda_\ell\delta_2^m \\ & + \Phi_5\, e^{ijk}\lambda_k\end{aligned}$$

where the Φ_n are functions of μ, λ_2, and t only.

For the A_1^i above, with isotropic initial conditions, the Φ_n become

$$\Phi_1 = a\mu^2 \exp\left(-2\frac{M^2}{R}t\right) \exp\left[-2\frac{\mu^2}{R}(t+t_o)\right] \cdot \left[\lambda_2^2\left(\exp\left(2\frac{M^2}{R}\frac{\beta^2}{\mu^2}t\right) - 1\right) - \beta^2\right]$$

$$\Phi_2 = a\mu^2 \exp\left(-2\frac{M^2}{R}t\right) \exp\left[-2\frac{\mu^2}{R}(t+t_o)\right]$$

$$\Phi_3 = a\frac{\mu^2}{\beta^2} \exp\left(-2\frac{M^2}{R}t\right) \exp\left[-2\frac{\mu^2}{R}(t+t_o)\right] \cdot \left[1 - \exp\left(2\frac{M^2}{R}\frac{\beta^2}{\mu^2}t\right)\right]$$

$$\Phi_4 \equiv 0$$

$$\Phi_5 = aj\mu \exp\left(-2\frac{M^2}{R}t\right) \exp\left[-2\frac{\mu^2}{R}(t+t_o)\right] \exp\left(-\frac{M^2}{R}\frac{\lambda_2^2}{\mu^2}t\right)$$

where $\beta^2 = \mu^2 - \lambda_2^2$.

From this analysis it appears that with the application of a B-field, an isotropic field of turbulence will decay to an axisymmetric field with a time constant of (R/M^2). Furthermore, in the final decay of the axisymmetric field,

$$\overline{u^i u^i} \sim t^{-5/2} \exp\left(-2\frac{M^2}{R}t\right)$$

This represents an exponential decay that may be compared with the power law,

$$\overline{u^i u^i} \sim t^{-5/2}$$

for isotropic turbulence.

J. W. Poduska

References

1. N. Wiener, Nonlinear Problems in Random Theory (The Technology Press of the Massachusetts Institute of Technology, Cambridge, Mass., and John Wiley and Sons, New York, 1958).

2. J. W. Poduska, Random Theory of Turbulence, S. M. Thesis, Department of Electrical Engineering, M. I. T., 1960.

3. N. Wiener, op. cit., see Chapters III and IV, and Appendix A1.

4. FUEL CELLS

a. Introduction

There is still considerable disagreement among authors as to the exact location of the electrode reactions occurring in a fuel cell, especially when gaseous reactants are used. That is, some statements indicate that the three-phase boundary line between the gas, the electrolyte, and the electrode in the usual type of porous diffusion electrode represents the reaction locale. The fact that these diffusion electrodes do not function satisfactorily when "drowned" has been cited as evidence for the hypothesis that reaction occurs primarily at this "three-phase boundary". Sama's (1) work, on the other hand, suggests that reaction occurs at the two-phase boundary plane between the liquid and the gas phases. In this case, the reactant gas must first diffuse through the pores of a diffusion type of electrode to the liquid-solid interface, dissolve in the electrolyte, and then diffuse to the nearby submerged electrode surface. If solubilities are low, then the reactant can effectively diffuse only over small distances, hence reaction is largely restricted to the submerged area lying close to the three-phase boundary line. Hence, under the usual operating conditions, only a fraction of the total internal area of the electrode is effectively available for reaction.

The method proposed here for resolving the question of which of these two explanations is correct involves operation of a totally flooded electrode. The fuel cell reagent in question will first be dissolved in appropriate amounts in the electrolyte. This solution will then be caused to flow continuously through the electrode that is under study. In this way, a larger fraction of the internal electrode will be fed with an electrolyte solution of the reactant in question, but no three-phase boundary will exist anywhere within the system. Thus, if the two-phase theory is correct, higher current densities should be obtainable when operating "flooded" with an electrolyte solution of the reactant, than when operating with a gas-liquid interface maintained within the system. By suitable variation of flow velocities, reactant concentration, temperature, and so forth, insight into the rate-limiting steps should be obtained. It is proposed to use this technique to explore both the oxygen electrode and the fuel electrode.

b. Apparatus

The apparatus needed for this study has been built and the first "shake-down" runs have been successfully completed. A schematic diagram is presented in Fig. II-51, which is largely self-explanatory. In this apparatus, the following things can be varied independently: composition of the electrolyte, including concentration of reagent, such as oxidant or fuel; flow rate of this electrolyte through the electrode; temperature; and current density. The electrode itself can, of course, be replaced at will, so that study can be made of porosity, the catalyst to be used, dimensions, and so forth.

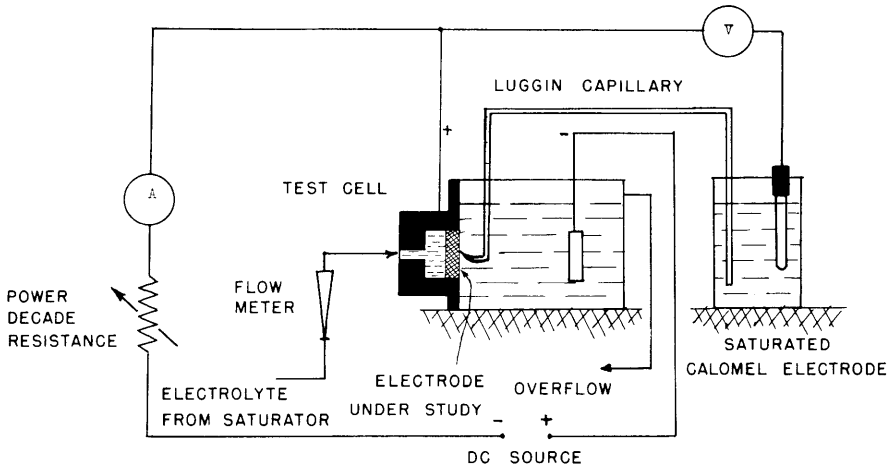

Fig. II-51. Schematic diagram of the apparatus.

Our procedure involves measuring the potential of the electrode under study as a function of current against a saturated potassium chloride-calomel electrode. This potential is measured right at the electrode surface by means of a Luggin capillary. Constant current is obtained by the use of a dc source connected in series with a 1-megohm decade power resistor.

The current density can be measured within 1.0 per cent accuracy in the range 0.01-2,000.0 ma/cm^2, and the electrode potential is measured with a Sargent Model M. R. recorder, capable of accuracies of 0.1 per cent throughout the voltage range to be studied. As can be seen from Fig. II-51, the electrode under study is isolated by the use of a "dummy" on the other electrode. Care is taken in all cases to prevent the reaction products from the "dummy" electrode from reaching the electrode that is being studied. The electrolyte is premixed, or saturated with the reactant in a pressure vessel, from which it can be driven with a constant pressure head through a flowmeter and the electrode body itself. The whole assembly – saturator, lines, valves, and so forth – is either made of plastic materials, glass, or is plastic-coated, to prevent galvanic currents and electrolyte contamination. The unit can be run at pressures up to 5 atm.

H. P. Meissner, A. R. Reti

References

1. D. A. Sama, Metal Oxide-Oxygen Electrodes and Fuel Cells, Sc. D. Thesis, Department of Electrical Engineering, M. I. T., June 1960.